

DIGITAL ACCESS TO SCHOLARSHIP AT HARVARD
DASH.HARVARD.EDU

HARVARD LIBRARY


Biomaterial Directed Immune Modulation and Tissue Regeneration in the Context of Skeletal Muscle Injury

Citation

Raimondo, Theresa Marie. 2019. Biomaterial Directed Immune Modulation and Tissue Regeneration in the Context of Skeletal Muscle Injury. Doctoral dissertation, Harvard University, Graduate School of Arts & Sciences.

Link

http://nrs.harvard.edu/urn-3:HUL.InstRepos:41121315

Terms of use

This article was downloaded from Harvard University's DASH repository, and is made available under the terms and conditions applicable to Other Posted Material (LAA), as set forth at
https://harvardwiki.atlassian.net/wiki/external/NGY5NDE4ZjgzNTc5NDQzMGIzZWZhMGFlOWI2M2EwYTg

Accessibility

https://accessibility.huit.harvard.edu/digital-accessibility-policy

Share Your Story

The Harvard community has made this article openly available.
Please share how this access benefits you. Submit a story

Biomaterial Directed Immune Modulation and Tissue Regeneration in the Context of Skeletal Muscle Injury

A dissertation presented

by

Theresa Marie Raimondo

to

The Harvard John A. Paulson School of Engineering and Applied Sciences

In partial fulfillment of the requirements

for the degree of

Doctor of Philosophy

in the subject of

Engineering Sciences

Harvard University

Cambridge, Massachusetts

August, 2018

© 2018 Theresa Marie Raimondo

All rights reserved.

Dissertation Advisor: Professor David J. Mooney Theresa Marie Raimondo

Biomaterial Directed Immune Modulation and Tissue Regeneration

in the Context of Skeletal Muscle Injury

ABSTRACT

Chronic wounds and inflammatory diseases pose a significant health challenge worldwide. In fact, chronic inflammation contributes to the pathogenesis of 7 of the 10 leading causes of death in the United States (CDC, 2016) and the prevalence of diseases associated with chronic inflammation is anticipated to rise. Dysregulation of the inflammatory response can inhibit healing and cause progressive tissue damage. The successful regeneration of functional tissues requires both appropriate modulation of the inflammatory response, and activation of tissue resident cells. Biomaterials offer unique opportunities to spatiotemporally control cytokine delivery, and may provided significant advantages in the modulation of immune cells and tissue resident stem cells alike to promote regeneration. The aim of this thesis is to develop and explore biomaterial systems capable of both modulating the inflammatory response and directly promoting tissue regeneration, independently, in the context of skeletal muscle.

In order to modulate the inflammatory response, gold nanoparticles (AuNPs) were designed to deliver immunomodulatory cytokines that could direct macrophage polarization. Partial PEGylation of the AuNP surface, followed by cytokine conjugation resulted in the generation of stable nanoparticles that retained the bioactivity of the conjugated cytokines. Conjugated IL-4, IL-13, and IL-10, all potent promoters of anti-inflammatory and pro-regenerative macrophage phenotypes (M2), were able to direct the polarization of human macrophages in vitro towards M2 phenotypes. Further, PEGylated, IL-4 conjugated AuNPs were able to shift the balance of macrophages in vivo, in ischemic muscle tissue, away from the inflammatory and towards the pro-regenerative M2a phenotype. Importantly, this shift in macrophage polarization resulted in improved muscle histology, and ultimately improved muscle function as evidenced by significant increases in muscle contraction force and velocity.

This thesis also explored the use of an established biomaterial system, an injectable alginate hydrogel, to deliver growth factors that could promote angiogenesis, innervation, and muscle regeneration in the contexts of muscle nerve injury and microvascular muscle transplantation. First, in a model of sciatic nerve injury in aged mice, the combined delivery of vascular endothelial growth factor (VEGF) and insulin-like growth factor-1 (IGF-1) promoted the regeneration on functional muscle innervation, ultimately leading to improved toe spreading, significant increases in muscle fiber area, and increased muscle contraction force and velocity. Subsequently, this strategy was tested in a more clinically relevant model of autologous muscle transplantation in rabbits. Here, clinical electromyography demonstrated a significant increase in compound muscle action potential, indicative of improved engraftment and muscle function, in response to alginate delivery of VEGF + IGF-1.

In summary, this thesis demonstrates the ability of biomaterials to both modulate the innate inflammatory response and directly promote tissue regeneration, independently, in skeletal muscle tissue. The ability to promote resolution of inflammatory processes in vivo, shift macrophage polarization towards regenerative phenotypes, and directly stimulate tissue regeneration opens new opportunities for biomaterial based regenerative therapies.

TABLE OF CONTENTS

CHAPTER 1: Introduction……1
1.1 Motivation……..1
1.2 Background……..2
1.3 Hypothesis…….....13
1.4 Specific Aims…….....13
1.5 Significance……..…….…...13
1.6 References……..……..15

CHAPTER 2: M2 Macrophage Polarizing Cytokines can be Conjugated to Gold Nanoparticles and Direct Macrophage Polarization……..……22
2.1 Introduction……...…….22
2.2 Materials and Methods……..……....24
2.3 Results……..…….28
2.4 Discussion……..……...50
2.5 References…….……....53

CHAPTER 3: Functional Muscle Recovery with Nanoparticle-Directed M2 Macrophage Polarization in Mice……...57
3.1 Introduction…….....57
3.2 Materials and methods…….....58
3.3 Results…….....63
3.4 Discussion……82
3.5 References…….....85

CHAPTER 4: Combined delivery of VEGF and IGF-1 promotes functional innervation and improves muscle transplantation in mice and rabbits……....89
4.1 Introduction……...89
4.2 Materials and Methods…….....92
4.3 Results……...96
4.4 Discussion……...114
4.5 References……...119

CHAPTER 5: Conclusions, Implications, and Future Directions……...124
5.1 Summary and Conclusions…….....124
5.2 Implications…….....126
5.3 Future Directions……....128
5.4 References……...131

APPENDICIES……134
APPENDIX A: Supplemental Figure and Table for Chapter 2……....134
APPENDIX B: Supplemental Methods and Figures for Chapter 3……..136
APPENDIX C: Supplemental Figures for Chapter 4……....141

ACKNOWLEDGEMENTS

I would like to start by thanking Dr. David Mooney for his support and guidance over the past several years. It was under his mentorship that I learned the importance of independent thinking, asking critical questions, and formulating novel research. I greatly appreciate the opportunity to have worked in his lab and collaborate with the other graduate students and postdoctorial fellows under his supervision.

It is out of deep gratitude and respect that I would like to thank the members of my dissertation committee, Dr. Herman Vandenburgh, and Dr. Samir Mitragotri, for their time and thought provoking discussions. Each provided very valuable insights and raised questions that further advanced my thinking and research. I greatly appreciated the experience of discussing my research with them and have learned to appreciate the value of alternative perspectives.

I would be remiss if I did not express my gratitude to Dr. Simon Talbot and Dr. Hehuan Li. Their surgical expertise was crucial to the completion of these experiments. Dr. Talbot was a close collaborator who contributed his expertise to the design, implementation, and interpretation of many experiments including microsurgical studies of murine muscle innervation and rabbit muscle transplantation.

Over the past several years it has been my great fortune to collaborate with so many investigators in the Mooney Lab. In particular I would like to acknowledge, Dr. Cathal Kearney, Dr. Hadas Skaat, Dr. Brian Kwee, Dr. Erin Anderson, Dr. Sahar Rahmani, Dr. Christine Cezar, Dr. Angelo Mao, and Dr. Nisarg Shah. Many others at Harvard, the Wyss Institute, and Brigham and Women's have contributed invaluably to my research over the years. In particular, I would like to thank Edward Doherty from the Wyss Institute for his alginate hydrogel expertise, and for providing materials; Benjamin Ferland from Brigham and Women's for his histology expertise; Dr. Roderick Bronson from the Harvard Medical School for his histology and pathology expertise; Thomas Ferrante from the Wyss Institute for his microscopy expertise; Patricia Rogers from the Bauer Core for her assistance with flow cytometry; and

Matthew Pezone from the BRI animal facility for his help with animal work. I would also like to thank the undergraduate students, Erica Budina, Kaitlyn Felsheim, and Theresa Rizk, who gave me the opportunity to grow as a mentor and for contributing to data collection.

I am grateful to Kurt Schellenberg, Katie Parodi, and Joan Cassidy whose exceptional management of the laboratory made these experiments possible.

I greatly appreciate the funding provided by the NIH, the Wyss Institute, and the NSF Graduate Research Fellowship.

Finally, I would like to thank my family for their patience and unending support, and for impressing upon me the importance of higher education.

Theresa Marie Raimondo

August, 2018

CHAPTER 1:

Introduction

1.1 Motivation

The human body has an innate, yet limited, ability to regenerate diverse tissues following injury including bone, cartilage, nerves, skin, and muscle. Incomplete regeneration, however, often leads to progressive degeneration, functional disability, and limb amputation [1]. Successful regeneration of functional tissue requires both the activation and maturation of stem cells into organ specific parenchymal cells and guidance of the immune response. The innate immune response plays a central role in coordinating tissue repair processes, and further, the regenerative capacity of stem cells is influenced by regulatory networks orchestrated by the immune response [2]. This complex interplay between tissue regeneration and innate immunity has been observed in many tissues including skin [3], cardiac and skeletal muscle [4, 5], bone [6], and the nervous system [7]. Uncontrolled activation of immune cells, and incomplete resolution of the acute inflammatory response, can inhibit regeneration and cause progressive tissue damage [8]. In fact, chronic inflammation contributes to the pathogenesis of many diseases, including 7 of the 10 leading causes of death in the United States (CDC, 2016).

Stem cell therapy has generated much interest in the contexts of traumatic injury, following some cancer treatments such as irradiation [9], cardiovascular diseases [10, 11], cerebrovascular disease (stroke) [12], and central nervous system diseases (myelin diseases, retinal disease, Parkinson's disease, and neurodegenerative diseases) [13]. Given the limited tissue regeneration typically manifested in these conditions, the hope is that transplanted stem cells will 'seed' the injured region ultimately leading to the regeneration of functional tissue. While such therapies hold great promise, to date, clinical trials have shown minimal therapeutic improvements [2]. Poor donor cell engraftment and viability, sub-optimal cell migration, and immune rejection have limited the use of such therapies [14]. The recruitment and transplantation of cells relies on an inductive microenvironment composed of the appropriate paracrine

cues to support cell viability and regeneration, supportive stromal cells, and hospitable/pro-regenerative immune cells.

Biomaterials can be designed to modulate the local microenvironment in injured tissue both to provide cues to stimulate cell regeneration, and modulate the inflammatory response. By controlling the degradation rate of the biomaterial, it can be used to control the release of multiple cytokines in a spatiotemporally regulated manner [15]. The release of growth factors that mimic endogenous regenerative cascades can promote functional tissue regeneration while the presentation of immunomodulatory cytokines can control the immune response. This thesis explores the use of various biomaterials both to control the innate immune response and to deliver pro-regenerative growth factors to ultimately improve the regeneration of tissue function. These concepts are explored independently, within the context of skeletal muscle regeneration.

1.2 Background: Inflammation plays a central role in tissue regeneration and disease progression

Inflammation is a protective response that kills invading pathogens and initiates tissue regeneration. The quality of tissue regeneration is dependent on the nature and successful resolution of the inflammatory response. Uncontrolled inflammation can lead to progressive tissue damage and cause disease. Statistics from the Center for Disease Control (CDC) reveal that chronic inflammation contributes to the pathogenesis of 7 of the 10 leading causes of death in the United States: heart disease, cancer, chronic lower respiratory disease, stroke, Alzheimer's disease, diabetes, and nephritis (2016), and the prevalence of diseases associated with chronic inflammation is anticipated to increase. Worldwide, 3 of 5 people die due to chronic inflammatory diseases [16]. In addition, chronic inflammation leads to significant morbidity from other diseases such as osteoarthritis, rheumatoid arthritis, psoriatic arthritis, inflammatory bowel disease, and chronic obstructive pulmonary disease. Therefore, the development of therapeutics to modulate the inflammatory response is of considerable interest.

1.2.1 The innate inflammatory response

Innate inflammation is the natural, protective, biological response of vascular tissues to pathogen invasion and/or tissue injury. Following infection or injury, tissue resident innate immune cells, including macrophages, dendritic cells and mast cells, recognize infection and tissue damage. Pattern-recognition receptors expressed by these cells allow them to identify pathogen and damage associated molecular patterns thereby allowing discrimination between self and non-self (microbial) components, and the identification of tissue damage, respectively [17]. In response to infection and/or injury, these tissue resident cells secrete inflammatory cytokines and chemotactic signals that increase vascular permeability to allow the delivery of serum antibodies, complement proteins, and the recruitment of inflammatory immune cells, including neutrophils, natural killer cells, and monocytes along with cells of adaptive immunity, to the compromised tissue.

Neutrophils are among the first innate immune cells recruited. Following extravasation, neutrophils release reactive oxygen species and proteins that contribute to microbe killing and matrix degradation. They also promote endothelial cell activation for the subsequent recruitment of monocytes. Following neutrophil recruitment, monocytes localize in the compromised tissue where they differentiate into macrophages. Inflammatory cytokines, along with pathogen and damage associated molecular patterns, activate macrophages. These inflammatory macrophages secrete inflammatory cytokines (such as tumor necrosis factor-α (TNFα), interleukin (IL)-1 and IL-6, among others), and reactive oxygen and nitrogen radicals to both ramp up the inflammatory immune response and kill invading pathogens. Macrophages, along with dendritic cells, neurophils, mast cells and monocytes, also play a central role in the phagocytosis of tissue debris, making way for subsequent tissue regeneration, and antigen presentation to T cells to inform adaptive immunity. Adaptive immunity, however, is outside the scope of this thesis. The phagocytosis of apoptotic neutrophils stimulates macrophages to release mediators (such as transforming growth factor-β (TGF-β) and IL-10) that suppress the inflammatory response [18]. Suppression of the initial inflammatory response is critical for subsequent tissue healing as many of the

inflammatory, microbe killing, and matrix degrading processes associated with acute inflammation can also cause collateral tissue damage. Unresolved inflammation has been shown to inhibit the healing of chronic skin ulcers in diabetic patients [19], limit cardiac regeneration following myocardial infarction [20], and significantly contribute to muscle wasting in muscular dystrophies [21]. Neutrophil apoptosis and subsequent down regulation of the inflammatory macrophage phenotype prevent further infiltration of neutrophils and monocytes, bring about resolution of the acute inflammatory response, and initiate tissue regenerative processes. Resolution of the acute inflammatory response and macrophage adaption of pro-regenerative pheontypes are critical for the activation of tissue resident stem and progenitor cells, initiation of tissue regeneration, and restoration of homeostasis.

1.2.2 Macrophage Polarization

Macrophages play a central role in regulating inflammation because they adopt both pro-inflammatory (M1) and pro-regenerative (M2) phenotypes. In response to various environmental cues macrophages display great plasticity, able to sequentially change their physiology. This plasticity gives rise to many macrophage phenotypes, typically referred to as polarization states, that serve various functions ranging from host defense, wound healing, and immune regulation [22].

Classically activated or M1 macrophages are inflammatory cells initially stimulated in response to acute inflammation. In their original characterization, M1 macrophages were stimulated in response to interferon-γ (IFN-γ) and tumor-necrosis factor (TNF), secreted high levels of pro-inflammatory cytokines, and showed enhanced microbicidal and tumoricidal abilities [22]. The secretion of inflammatory mediators such as TNF, nitric oxide, reactive oxygen and nitrogen species, and cytokines (such as IL-1, IL-6, IL-12, and IL-23) contribute to the killing of pathogens, activation of oxidative processes, and polarization of the adaptive immune response which further drives the inflammatory response [23]. The importance of an initially M1 dominated inflammatory response in host defense is well established. Both mice lacking IFNγ expression and humans with genetic mutations in these signaling pathways are more

susceptible to bacterial, protozoal and viral infections [24]. These antimicrobial processes, however, are somewhat indiscriminate and can be highly damaging to neighboring tissues [23]. Indeed, the over expression or prolonged activation of M1 macrophages is believed to be a critical component of the pathogenesis of many chronic inflammatory and autoimmune diseases including atherosclerosis [25], inflammatory bowel disease [26], asthma [26], rheumatoid arthritis [27], osteoarthritis [28], multiple sclerosis [29], and chronic venous leg ulcers [30].

In direct contrast to the M1 phenotype, macrophages can also adapt anti-inflammatory and pro-regenerative phenotypes, broadly called the M2 polarization states. M2 macrophages are generally characterized by low production of inflammatory cytokines, and express high levels of IL-10 and low levels of IL-12 [31]. An important subcategory of M2 macrophages are those stimulated in response to IL-4 and IL-13, typically referred to as wound-healing macrophages, or M2a macrophages [22]. Immune cells in the tissue are important sources of IL-4 that stimulate resolution of the acute inflammatory response. In macrophages, IL-4 stimulates arginase metabolism ultimately leading to the production of polyamines and collagen, and contributing to the production of extracellular matrix, an important component of tissue regeneration [32]. M2a macrophages generated in vitro in response to IL-4 and/or IL-13 are less efficient than M1 macrophages at producing oxygen and nitrogen radicals, killing intracellular pathogens, presenting antigen, and secreting inflammatory cytokines [33]. These macrophages also produce growth factors (such as platelet-derived growth factor) and cytokines (such as TGF-β1) which stimulate fibroblasts to differentiate into myofibroblasts, and contribute to the activation and/or maturation of tissue resident stem cells (such as satellite cells in skeletal muscle tissue) leading to tissue regeneration [23]. Further, M2a macrophages express the decoy IL-1RII and IL-1 receptor antagonist, thereby directly suppressing inflammatory mechanisms promoted by the M1 phenotype [31]. Taken together, these studies have lead many to believe that the primary functions of M2a macrophages are suppression of inflammation and promotion of wound healing [22]. Related to their production of extracellular matrix, however, M2a macrophages also play a role in scar formation. Matrix deposition,

used to form granulomas and 'wall-off' macroparasites, is an important component of immunity against helminthes and nematodes orchestrated my M2a macrophages [34]. Over expression of M2a macrophages, like over expression of M1 macrophages, can also be detrimental to the host. However rather than leading to tissue destruction, dysregulation of the M2a response leads to excessive fibrosis that can limit tissue function.

Another important phenotype of macrophages is stimulated in response to glucocorticoids and IL-10; these are considered regulatory or anti-inflammatory macrophages, and called M2c macrophages. These macrophages produce high levels of IL-10, a potent inhibitor of inflammation, and TGF-β [31, 22]. In contrast to M2a macrophages, M2c macrophages do not substantially contribute to extracellular matrix production, and they can present antigen to adaptive immune cells [33]. As such they can patrol tissue, identify and present antigen in response to infection, dampen inflammation, and modulate the adaptive immune response. Dysregulation of M2c macrophages can lead to inappropriate alterations in immune suppression, predispose the host to allergy or infection, and contribute to the progression of neoplasia [22].

1.2.3 Interplay between macrophage polarization and skeletal muscle regeneration

The coordination between macrophage polarization and skeletal muscle regeneration has been well established. Satellite cells are muscle resident stem cells that are thought to be primarily responsible for skeletal muscle regeneration [35]. Following injury, satellite cells must become activated and proliferate, migrate to the site of injury, fuse to form muscle fibers, and mature, to yield functional regenerated myofibers [35]. Appropriate regulation of macrophage polarization is essential for muscle regeneration because macrophages directly control various stages of satellite cell activation and maturation [36, 37]. It has been observed in histology from regenerating healthy human muscle that regions associated with proliferating myogenic precursor cells were associated with M1 macrophages. Conversely, in the same muscle, regions containing differentiating myogenic precursor cells were

associated with anti-inflammatory macrophages [36]. This data, along with data from many preclinical studies, has clearly suggested coordination between progression of the acute inflammatory response with myogenesis [38]. Within hours after injury, and extending for a few days, resident immune cells and recruited macrophages are biased towards the M1 phenotype; concurrently, satellite cells are activated and begin to proliferate. Subsequently, M2 macrophages secrete anti-inflammatory cytokines as myogenic precursor cells begin to differentiate. Myogenesis and progression of the innate inflammatory response are spatially and temporally linked.

Both M1 and M2 macrophages play a critical role in muscle tissue regeneration. Disruptions to the regulation of macrophage polarization have been shown to delay muscle regeneration in murine models. Deletion of microRNA-155, an RNA that does not regulate satellite cells but rather regulates the balance between M1 and M2 macrophages, significantly inhibited the regeneration of muscle fibers [37]. Coordination between macrophages and satellite cells is essential for successful regeneration of muscle function. IFN-γ expression by immune cells stimulated as part of the inflammatory response following muscle injury, both promotes M1 macrophage polarization and is secreted by M1 macrophages, and is temporally coordinated with the proliferation and accumulation of myogenic precursor cells in the damaged muscle [39]. M1 macrophages promote myogenic precursor cell proliferation by the secretion of TNF-α, IL-6, and GM-CSF [40, 41]. In a model of cardiotoxin induced murine muscle injury, administration of an IFN-γ blocking antibody reduced myogenic cell proliferation, ultimately resulting in a decreased number and area of regenerating myofibers [39]. Further, IFN-γ null mice showed decreased accumulation of M1 macrophages following cardiotoxin induced muscle injury and increased fibrosis, as opposed to functional muscle regeneration [39]. This result is consistent with the known function of M1 macrophages in promoting the proliferation of myogenic precursor cells and M2 macrophages in fibrosis. IFN-γ provides one direct link between innate immunity and myogenesis. IFN-γ associated with the M1 inflammatory response directly binds myogenic precursor cells and activates pathways that inhibit differentiation [38]. In addition to IFN-γ, M1 macrophages secrete high levels of TNF-α, IL-6, and IL-1β

which inhibit myogenic precursor cell maturation [41]. Maintenance of the myogenic proliferative state is initially required to provide sufficient cells to support muscle tissue repair. Prolonged presence of M1 macrophages, however, inhibits the differentiation and fusion of myogenic precursor cells [40]. Skewing towards the M1 phenotype leads to defects in muscle regeneration and an inability to regenerate mature functional fibers.

M2 macrophages play a critical role in promoting the commitment of myogenic precursor cells to terminal differentiation, fusion and growth of myofiber diameter, and ultimately promoting the regeneration of functional myofibers. In contrast to M1 macrophages, M2 macrophages secrete TGF-β which stimulates the formation of myotubes [41]. In vitro co-cultures of M2 macrophages with myogenic cells promoted myogenic differentiation as assessed by myogenin expression and fusion into myotubes [5]. Intramuscular depletion of macrophages at later timepoints following notexin injury, corresponding to the M2 macrophage dominated phase of the immune response, lead to a decrease in the diameter of regenerating fibers [5] supporting the important role of M2 macrophages in late stages of myogenesis and muscle regeneration. Blocking the induction of M2 polarization, in vivo, but not M1 polarization, by genetic depletion of CREB-binding sites in macrophages resulted in sever defects in muscle fiber regeneration [42]. Other studies have shown that conditional deletion of the insulin-like growth factor 1 (IGF-1) gene, which also inhibited M2 polarization, resulted in fewer regenerating myofibers in the muscle cross section and diminished myofiber cross sectional area among the regenerating myofibers [43]. Importantly, in both of these studies conditional genetic mutation of macrophages resulted in incomplete muscle regeneration. Deletion of CREB-binding sites in muscle cells only (and not macrophages) had no affect on muscle regeneration [42], together suggesting a direct effect of M2 macrophages on myogenesis. The differentiation of myogenic precursor cells promoted by M2 macrophages is critical for the regeneration of functional muscle fibers.

The data discussed here suggest that macrophage polarization sequentially orchestrates myogenesis in skeletal muscle repair, and provides support for the concept that macrophage polarization plays a direct role in stem cell activation and tissue regeneration.

1.2.4 Biomaterial based approaches for macrophage polarization

Therapeutic strategies that encourage resolution of the initial inflammatory response and promote either M1 or pro-regenerative macrophage phenotypes are of considerable interest. To this end, the delivery of macrophage polarizing cytokines has been explored in both preclinical models and clinical trials. Directing M1 macrophage polarization to promote the killing of aberrant cells by the immune system, and to limit the development of tolerance by adaptive immunity, has been explored in the context of solid tumors [44, 45]. Conversely, directing M2 polarization is of interest in the context of chronic inflammatory and autoimmune conditions including autoimmune demyelinating disease, arthritis and psoriasis [46, 47, 48] among others. Although potent regulators of macrophage polarization, cytokines are unstable in vivo and are often associated with systemic side effects [49]. In vivo instability and short half-lives of such cytokines have led to the use of high doses with repeated or continuous administration [48, 47]. The use of IL-4 to direct a type 2 immune response has shown promise in clinical trials of psoriasis. In a trial of 20 patients with severe psoriasis, subcutaneous IL-4 injection resulted in improved clinical scores for all patients, with 15 patients showing >68% improvement [48]. In this study however, IL-4 was administered three times a day, five days a week, for six weeks. Although this study shows the potential of cytokine therapies for innate immune modulation, the treatment of organs for which direct injection is not possible, and the intravenous administration of such high doses of cytokine drugs, remain challenging. As a result, the success of other diverse cytokine therapies has been variable [49].

Biomaterials offer many advantages in the spatiotemporal control of cytokine release, and may prove particularly advantageous in the delivery of macrophage polarizing cytokines. The diffusion of cytokines from scaffolds in muscle tissue has been studied extensively both computationally and

experimentally [50, 51], and scaffolds have been developed to allow for controlled degradation rates and the release of multiple cytokines with independent kinetics [15, 52]. In the context of macrophage polarization for tissue regeneration, the use of scaffolds to initially promote an M1 macrophage dominated response followed by and M2 response may improve tissue resident stem cell activation and promote tissue maturation yielding more functional tissue than current therapies. With this goal in mind silk protein films have been developed to release either IFN-γ or IL-4, and were able to direct the repolarization of M2 macrophages towards the M1 phenotype or vice versa, respectively, in vitro [53]. Decellularized bone scaffolds have also been designed to rapidly release IFN-γ, to promote M1 polarization, and slowly release IL-4, to promote subsequent M2a polarization [54]. Despite only week physical adsorption of IFN-γ to the scaffold and IL-4 conjugation via biotin-streptavidin bonding, IFN-γ and IL-4 demonstrated overlapping release profiles that tempered sequential macrophage polarization. The delivery of macrophage polarizing cytokines to improve the integration of biomaterials, and prevent rejection or fibrosis (which often limits the effectiveness of the material) is also gaining attention [55]. An IL-4 releasing thin coating has been used to coat a non-degradable polypropylene mesh material, and direct M2a macrophage polarization in vivo at the implant surface in mice, ultimately improving tissue integration of the implant [56].

Nanoparticles also offer unique advantages in macrophage modulation. Nanoparticles, following injection, can distribute throughout the tissue (as opposed to scaffolds) to contact and polarize many macrophages, can be designed (by modulation of size and hydrophobicity) to slow lymphatic drainage [57], localize in inflamed tissues due to the increased vascular permeability in these tissues [58], and tissue responsive nanoparticles can be used to release cytokines only in the target tissue [45]. Mesoporous silica nanoparticles with extra-large pores have been designed to deliver IL-4 [59]. Following intravenous injection, these particles targeted phagocytic myeloid cells and upregulated M2 polarization in the spleen [59]. Further, hyaluronic acid-poly(ethyleneimine) nanoparticles delivering plasmid DNA expressing either IL-4 or IL-10 upregulated M2a and M2c macrophage polarization, respectively, in peritoneal

macrophages following intraperitoneal injection [60]. Nanoparticles have also been developed to promote M1 polarization, typically for use as cancer therapies. pH responsive polymeric nanoparticles containing IL-12 have been shown to release IL-12 in a tumor microenvironment in vivo, shift macrophage polarization, and slow the progression of tumor growth [45]. Further, phase I clinical trials have been completed for TNF-α coated, PEGylated, gold nanoparticles (CYT-6091) for the treatment of patients with advanced stage solid tumors [61]. The phase I trial concluded that CYT-6091 was well tolerated and allowed for doses of TNF-α three-times greater than the previously published maximum tolerated dose. A phase II clinical trial in patients with pancreatic adenocarcinoma is being planned.

While significant advances for biomaterial direction of M1 polarization have been made, to date, approaches to direct M2 polarization following tissue injury or in the context of chronic inflammation, while promising, have shown limited therapeutic success.

1.2.5 Biomaterial based approaches for skeletal muscle repair

While tissue resident satellite cells endow muscle the capacity to regenerate, large volume muscle loss resulting from traumatic injury or tumor removal, functional damage associated with myopathies, chronic paralysis, and some genetic disorders such as Mobius syndrome often require reconstruction with donor tissue or engineered constructs [62]. Despite advancements in microsurgical techniques, successful reinnervation, engraftment, and function of transplanted autologous muscles are unpredictable and many patients are left with poor function [63, 64]. Biomaterials have been used to promote skeletal muscle regeneration both by (a) using scaffolds to create a synthetic niche to deliver cytokines, promote host muscle regeneration and/or deliver cells, and by (b) using a material to promote the assembly of myoblasts and other cell types in vitro prior to transplantation. The combined delivery of angiogenic (vascular endothelial growth factor, VEGF) and myogenic (IGF-1) factors promoted angiogenesis, reinnervation, and satellite cell activation and proliferation following ischemic muscle injury. This ultimately led to increased myofiber diameter and a 2.3-fold increase in tibialis anterior (TA) muscle

titanic force generation, compared to negative controls, 2 weeks post injury [15]. Further, the release of VEGF and IGF-1 from scaffolds used to transplant myogenic cells, improved cell engraftment and accelerated muscle regeneration [65]. The ability to protect the viability and regenerative capacity of transplanted cells, and importantly, the capacity of scaffolds to release cytokines that stimulate host regeneration holds great potential for clinical translation. The complex microenvironment of the regenerating muscle, and coordination required between many systems (muscle tissue, immune response, and peripheral motor nerves) to achieve functional regeneration remain significant challenges to the development of artificial muscle. Failure of any one of these biological systems to correctly engage in muscle regeneration can result in non-functional tissue or muscle atrophy. The delivery of cytokines that can promote both myogenesis and reinnervation (such as VEGF) [66], and of immune polarizing cytokines (discussed in section 1.2.4) make biomaterials an attractive strategy for muscle regeneration.

The development of tissue engineered skeletal muscle has also received much attention. Such constructs may be of great clinical utility in the replacement of damaged muscle in conditions where host regeneration is not possible, donor tissue is not available, or donor site morbidity is prohibitive. Further, such constructs can be used as in vitro model systems. Culturing myoblasts between two posts acting as artificial tendons promotes the organization of bundles of aligned myofibers [67, 68]. These bioartificial muscle (BAM) tissues are able to contract and generate force following stimulation. Importantly, BAMs have demonstrated clustering and maturation of acetylcholine receptors, suggesting that they recapitulate conditions that support innervations [69], which is essential for muscle viability and function. In a recent report, the murine femoral nerve was diverted into an engineered muscle construct [70], mimicking techniques used in the microvascular transfer of autologous muscle. Although the engineered construct was able to generate an action potential following nerve stimulation, its amplitude was much lower than that of native muscle [70]. Genetic modification of BAMs has been successfully used for the sustained, local delivery of cytokines following transplantation [71]. VEGF delivery from BAMs increased capillary

density in adjacent ischemic host muscle tissue [72], suggesting that artificial muscle constructs have potential to serve both as muscle replacement tissue and as a cytokine delivery platform.

1.3 Hypothesis

Biomaterial delivery of cytokines can improve functional skeletal muscle regeneration either by driving the polarization of macrophages towards the M2 phenotype, or by promoting the regeneration of muscle fibers and innervations.

1.4 Specific Aims

Three specific aims tested the above hypothesis:

Aim 1: Design a biomaterial/nanoparticle for the delivery of anti-inflammatory cytokines that can direct M2 macrophage polarization.

Aim 2: Examine the ability of IL-4 carrying nanoparticles to shift the balance of macrophages towards the M2 phenotype, and improve functional skeletal muscle regeneration following murine ischemic muscle injury.

Aim 3: Examine the ability of a VEGF and IGF-1 delivering biomaterial hydrogel to promote functional skeletal muscle regeneration following microvascular transplantation.

1.5 Significance

Chronic inflammatory diseases represent the most significant cause of death in the world, and their prevalence is expected to increase steadily for the next 30 years in the United States [16]. In addition to chronic disease, chronic inflammation causes tissue damage and has been linked to the pathology of non-healing wounds. Macrophages play a central role in regulating inflammation because they adopt pro-inflammatory (M1) and pro-regenerative (M2) phenotypes. Although cytokines that stimulate M1 and M2 polarization have been identified, their clinical use has been limited by their in vivo instability, inability to

target the inflamed tissue, and often broad systemic side effects. While biomaterials used to deliver M1 polarizing cytokines in the context of cancer therapy are currently in clinical trial, promotion of M2 phenotypes have not, to date, seen as much therapeutic success. This thesis aims to develop a biomaterial that can be used to direct macrophage polarization in vivo, in the context of tissue inflammation, to ultimately promote the regeneration of functional tissue. Specifically, this thesis will explore the development of a biomaterial that can shift the balance of macrophage polarization away from the M1 and towards the M2a phenotype in ischemic muscle, and promote functional muscle regeneration. The eventual goal is that such a material system could be used not only in the context of acute muscle injury but also in the context of chronic muscular dystrophies, and more broadly to modulate the macrophage response in many progressive degenerative and chronic inflammatory diseases to limit disease progression and promote healing.

In addition to the delivery of cytokines to modulate macrophage phenotype, this thesis also explores the ability of biomaterials to deliver cytokines to create a microenvironment that more directly promotes tissue regeneration, specifically in the context of muscle regeneration. Despite the advancements that have been made in the engineering of artificial muscle, autologous muscle transfer remains the clinical gold standard for the treatment of chronic paralysis. However engraftment and innervation of the transplanted tissue is unpredictable, and surgical nerve repairs only result in 52% satisfactory motor recovery [73]. The biomaterial explored in this thesis builds directly from previous work to develop scaffolds for the dual release of cytokines to promote angiogenesis, myogenesis, and innervation. This thesis aims to expand the use of these established scaffolds to treat muscle transplant tissue, improve engraftment and ultimately muscle function. The use of such biomaterials to improve engraftment of autologous muscle may circumvent the current challenges associated with the vascularization, innervation and function of engineered muscle and thereby provide a more rapid route to clinical adaption.

More generally, this thesis aims to explore the development of biomaterials to both modulate the innate immune response and promote tissue regeneration. The biological and medical fields have recently come to the understanding that the inflammatory response is not limited to host defense but also plays a critical role in orchestrating tissue regeneration, and, if dysregulated, disease progression. Coordination between innate immune cells and tissue resident stem cells is required for the regeneration of functional tissue. While biomaterial design has traditionally focused on minimizing the immune response, to limit scarring-off of the implanted material and rejection by the host, it has been appreciated more recently that appropriate direction of the immune response by biomaterials towards regenerative phenotypes may lead to improved functional tissue regeneration. The concepts explored here within the context of skeletal muscle regeneration are expected to find broad applicability in the areas of chronic disease treatment and tissue regeneration.

1.6 References

[1] P. Giannoudis and I. Pountos, "Tissue regeneration: The past, the present and the future," *Injury,* vol. 36, no. 4, Suppliment, pp. S2-S5, 2005.

[2] S. Forbes and N. Rosenthal, "Preparing the ground for tissue regeneration: from mechanism to therapy," *Nature Medicine,* vol. 20, no. 8, pp. 857-869, 2014.

[3] S. Willenborg and S. Eming, "Macrophages – sensors and effectors coordinating skin damage and repair," *JDDG: J German Soc Derm,* vol. 12, no. 3, pp. 214-221, 2014.

[4] M. Wang et al., "Crosstalk of mesenchymal stem cells and macrophages promotes cardiac muscle repair," *The International Journal of Biochemistry & Cell Biology,* vol. 58, pp. 53-61, 2015.

[5] L. Arnold et al., "Infl ammatory monocytes recruited after skeletal muscle injury switch into antiinfl ammatory macrophages to support myogenesis," *JEM,* vol. 204, no. 5, pp. 1057-1069, 2007.

[6] C. Champagne, J. Takebe, S. Offenbacher and L. Cooper, "Macrophage cell lines produce osteoinductive signals that include bone morphogenetic protein-2," *Bone,* vol. 30, no. 1, pp. 26-31, 2002.

[7] D. Donnelly and P. Popovich, "Inflammation and its role in neuroprotection, axonal regeneration and functional recovery after spinal cord injury," *Experimental Neurology,* vol. 209, no. 2, pp. 378-388,

2008.

[8] N. Kamaly et al., "Development and in vivo efficacy of targeted polymeric inflammation-resolving nanoparticles," *Proc Natl Acad Sci USA,* vol. 110, no. 16, pp. 6506-6511, 2013.

[9] A. Chapel et al., "Mesenchymal stem cells home to injured tissues when co-infused with hematopoietic cells to treat a radiation-induced multi-organ failure syndrome," *J Gene Med,* vol. 5, pp. 1028-1038, 2003.

[10] N. Pavo et al., "Cell therapy for human ischemic heart diseases: Critical review and summary of the clinical experiences," *J Molec Cell Cardiology,* vol. 75, pp. 12-24, 2014.

[11] A. Behfar, R. Crespo-Diaz, A. Terzic and B. Gersh, "Cell therapy for cardiac repair—lessons from clinical trials," *Nature Reviews Cardiology,* vol. 11, pp. 232-246, 2014.

[12] P. Rosado-de-Castro et al., "The Rise of Cell Therapy Trials for Stroke: Review of Published and Registered Studies," *Stem Cells and Development,* vol. 22, no. 15, pp. 2095-2111, 2013.

[13] S. Goldman, "Stem and Progenitor Cell-Based Therapy of the Central Nervous System: Hopes, Hype, and Wishful Thinking," *Cell Stem Cell,* vol. 18, no. 2, pp. 174-188, 2016.

[14] C. Cezar and D. Mooney, "Biomaterial-based delivery for skeletal muscle repair," *Advanced Drug Delivery Reviews,* vol. 84, pp. 188-197, 2015.

[15] C. Borselli, H. Storrie, F. Benesch-Lee, D. Shvartsmana, C. Cezara, J. Lichtmane, H. Vandenburgh and D. Mooney, "Functional muscle regeneration with combined delivery of angiogenesis and myogenesis factors," *Proc Natl Acad Sci,* vol. 107, no. 8, pp. 3287–3292, 2010.

[16] R. Pahwa and I. Jialal, Chronic Inflammation, Treasure Island (FL): StatPearls Publishing, 2018 [Updated 2018 Apr 19].

[17] J. Liu and X. Cao, "Cellular and molecular regulation of innate inflammatory responses," *Cellular & Molecular Immunology,* vol. 13, pp. 711-721, 2016.

[18] O. Soehnlein and L. Lindbom, "Phagocyte partnership during the onset and resolution of inflammation," *Nature Reviews Immunology,* vol. 10, pp. 427-439, 2010.

[19] E. Leal et al., "Substance P Promotes Wound Healing in Diabetes by Modulating Inflammation and Macrophage Phenotype," *Am J Path,* vol. 185, no. 6, pp. 1638-1648, 2015.

[20] S. Prabhu and N. Frangogiannis, "The Biological Basis for Cardiac Repair After Myocardial Infarction: From Inflammation to Fibrosis," *Circulation Research,* vol. 119, no. 1, pp. 91-112, 2016.

[21] A. Rosenberg et al., "Immune-mediated pathology in Duchenne muscular dystrophy," *Sci Transl Med,* vol. 7, no. 299, p. 299rv4, 2015.

[22] D. M. Mosser and J. P. Edwards, "Exploring the full spectrum of macrophage activation," *Nature Reviews,* vol. 8, no. 12, pp. 958-969, 2008.

[23] P. Murray and T. Wynn, "Protective and pathogenic functions of macrophage subsets," *Nature Reviews,* vol. 11, no. 11, pp. 723-737, 2011.

[24] O. Filipe-Santos et al., "Inborn errors of IL-12/23- and IFN-gamma-mediated immunity: molecular, cellular, and clinical features," *Semin Immunol.,* vol. 18, no. 6, pp. 347-361, 2006.

[25] A. Mantovani, C. Garlanda, M. Locati, "Macrophage Diversity and Polarization in Atherosclerosis: A Question of Balance," *Arterioscler Thromb Vasc Biol,* vol. 29, no. 10, pp. 1419-1423, 2009.

[26] X. Zhang, D.M. Mosser, "Macrophage activation by endogenous danger signals," *J Pathol,* vol. 214, no. 2, pp. 161-178, 2008.

[27] R. W. Kinne, B. Stuhlmuller, G. Burmester, "Cells of the synovium in rheumatoid arthritis. Macrophages.," *Arthritis Res Ther,* vol. 9, no. 6, pp. 224-239, 2007.

[28] N. Fahy et al., "Human osteoarthritic synovium impacts chondrogenic differentiation of mesenchymal stem cells via macrophage polarisation state," *HumaOsteoarthritis and Cartilage,* vol. 22, no. 8, pp. 1167-1175, 2014.

[29] J. Mikita et al., "Altered M1/M2 activation patterns of monocytes in severe relapsing experimental rat model of multiple sclerosis. Amelioration of clinical status by M2 activated monocyte administration," *Multiple Sclerosis Journal,* vol. 17, no. 1, pp. 2-15, 2011.

[30] A. Sindrilaru et al., "An unrestrained proinflammatory M1 macrophage population induced by iron impairs wound healing in humans and mice," *The Journal of clinical investigation,* vol. 121, no. 3, pp. 985-997, 2011.

[31] A. Mantovani et al., "The chemokine system in diverse forms of macrophage activation and polarization," *TRENDS in Immunology,* vol. 25, no. 12, pp. 677-686, 2004.

[32] T. Kreider, R. Anthony, J. Urban and W. Gause, "Alternatively activated macrophages in helminth infections," *Curr. Opin. Immunol.,* vol. 19, pp. 448-453, 2007.

[33] J. Edwards, X. Zhang, K. Frauwirth and D. Mosser, "Biochemical and functional characterization of three activated macrophage populations," *J. Leukoc. Biol.,* vol. 80, p. 1298–1307, 2006.

[34] J. Allen and T. Wynn, "Evolution of Th2 Immunity: A Rapid Repair Response to Tissue Destructive Pathogens," *PLoS Pathogens,* vol. 7, no. 5, p. e1002003, 2011.

[35] A. Wagers and I. Conboy, "Cellular and molecular signatures of muscle regeneration: Current concepts and controversies in adult myogenesis," *Cell,* vol. 122, no. 5, pp. 659-667, 2005.

[36] M. Saclier et al., "Differentially Activated Macrophages Orchestrate Myogenic Precursor Cell Fate During Human Skeletal Muscle Regeneration," *Stem Cells,* vol. 31, no. 2, pp. 384–396, 2013.

[37] M. Nie et al., "MicroRNA-155 facilitates skeletal muscle regeneration by balancing pro- and anti-inflammatory macrophages," *Cell Death and Disease,* vol. 7, no. 6, p. e2261, 2016.

[38] J. Tidball, "Regulation of muscle growth and regeneration by the immune system," *Nature Reviews, Immunology,* vol. 17, no. 3, pp. 165-178, 2017.

[39] M. Cheng, M. Nguyen, G. Fantuzzi and T. Koh, "Endogenous interferon-gamma is required for efficient skeletal muscle regeneration," *Am J Physiol Cell Physiol,* vol. 294, pp. C1183–C1191, 2008.

[40] J. G. Tidball and S. A. Villalta, "Regulatory interactions between muscle and the immune system during muscle regeneration," *Am J Physiol Regul Integr Comp Physiol,* vol. 298, no. 5, pp. R1173-R1187, 2010.

[41] M. Saclier, S. Cuvellier, M. Magnan, R. Mounier and C. B, "Monocyte/macrophage interactions with myogenic precursor cells during skeletal muscle regeneration," *FEBS Journal,* vol. 280, no. 17, pp. 4118-4130, 2013.

[42] D. Ruffell et al., "A CREB-C/EBP-beta cascade induces M2 macrophage-specific gene expression and promotes muscle injury repair," *Proc Natl Acad Sci,* vol. 106, no. 41, pp. 17475–17480, 2009.

[43] J. Tonkin et al., "Monocyte/Macrophage-derived IGF-1 Orchestrates Murine Skeletal Muscle Regeneration and Modulates Autocrine Polarization," *Molecular Therapy,* vol. 23, no. 7, pp. 1189-1200, 2015.

[44] L. Yang and Y. Zhang, "Tumor-associated macrophages: from basic research to clinical application," *J Hematology & Oncology,* vol. 10, pp. 58-69, 2017.

[45] Y. Wang et al., "Polymeric nanoparticles promote macrophage reversal from M2 to M1 phenotypes in the tumor microenvironment," *Biomaterials,* vol. 112, pp. 153-163, 2017.

[46] M. Racke, A. Bonomo, D. Scott, B. Cannella, A. Levine, C. Raine, E. Shevach and M. Rocken, "Cytokine-induced immune deviation as a therapy for inflammatory autoimmune disease," *J Exp Med,* vol. 180, no. 5, pp. 1961-1966, 1994.

[47] A. Horsfall, D. Butler, L. Marinova, P. Warden, R. Williams, R. Maini and M. Feldmann, "Suppression of collagen-induced arthritis by continuous administration of IL-4," *J Immunol,* vol. 159, no. 11, pp. 5687-5696, 1997.

[48] K. Ghoreschi et al., "Interleukin-4 therapy of psoriasis induces Th2 responses and improves human autoimmune disease," *Nature Medicine,* vol. 9, no. 1, pp. 40-46, 2003.

[49] Z. Zidek, P. Anzenbacher and E. Kmonickova, "Current status and challenges of cytokine pharmacology," *Br J Pharmacol,* vol. 157, no. 3, pp. 342–361, 2009.

[50] E. Silva and D. Mooney, "Spatiotemporal control of vascular endothelial growth factor delivery from injectable hydrogels enhances angiogenesis," *J Thromb Haemost,* vol. 5, pp. 590-8, 2007.

[51] N. Loren, M. Nyden and A. Hermansson, "Determination of local diffusion properties in heterogeneous biomaterials," *Advances in Colloid and Interface Science,* vol. 150, no. 1, pp. 5-15, 2009.

[52] T. Richardson, M. Peters, A. Ennett and D. Mooney, "Polymeric system for dual growth factor delivery," *Nature Biotechnology,* vol. 19, pp. 1029-1034, 2001.

[53] A. Reeves, K. Spiller, D. Freytes, G. Vunjak-Novakovic and D. Kaplan, "Controlled release of cytokines using silk-biomaterials for macrophage polarization," *Biomaterials,* vol. 73, pp. 272-283, 2015.

[54] K. Spiller et al., "Sequential delivery of immunomodulatory cytokines to facilitates the M1-to-M2 transition of macrophages and enhance vascularization of bone scaffolds," *Biomaterials,* vol. 37, pp. 194-207, 2015.

[55] R. Sridharan, A. Cameron, D. Kelly, C. Kearney and F. O'Brien, "Biomaterial based modulation of macrophage polarization: a review and suggested design principles," *Materials Today,* vol. 18, no. 6, pp. 313-325, 2015.

[56] D. Hachim, S. LoPresti, C. Yates and B. Brown, "Shifts in macrophage phenotype at the biomaterial interface via IL-4 eluting coatings are associated with improved implant integration," *Biomaterials,* vol. 112, pp. 95-107, 2017.

[57] D. Rao, M. Forrest, A. Alani, G. Kwon and J. Robinson, "Biodegradable PLGA based nanoparticles for sustained regional lymphatic drug delivery," *J Pharm Sci,* vol. 99, no. 4, pp. 2018-2031, 2010.

[58] J. Kim, L. Cao, D. Shvartsman, E. Silva and D. Mooney, "Targeted Delivery of Nanoparticles to Ischemic Muscle for Imaging and Therapeutic Angiogenesis," *Nano Letters,* vol. 11, no. 2, pp. 694-700, 2011.

[59] D. Kwon et al., "Extra-Large Pore Mesoporous Silica Nanoparticles for Directing in Vivo M2 Macrophage Polarization by Delivering IL-4," *Nano Letters,* vol. 17, no. 5, pp. 2747−2756, 2017.

[60] T.H. Tran, R. Rastogi, J. Shelke and M. Amiji, "Modulation of Macrophage Functional Polarity towards Anti-Inflammatory Phenotype with Plasmid DNA Delivery in CD44 Targeting Hyaluronic Acid Nanoparticles," *Scientic Reports,* vol. 5, pp. 16632-46, 2015.

[61] S. Libutti et al., "Results of a completed phase I clinical trial of CYT-6091: A pegylated colloidal

gold-TNF nanomedicine," *J Clinical Oncology,* vol. 27, no. 15S, pp. 3586-3586, 2009.

[62] A. Bach, J. Beier, J. Stern-Staeter and R. Horch, "Skeletal muscle tissue engineering," *J. Cell. Mol. Med.,* vol. 8, no. 4, pp. 413-422, 2004.

[63] F. Biglioli et al., "Recovery of Emotional Smiling Function in Free-Flap Facial Reanimation," *J Oral Maxillofac Surg,* vol. 70, pp. 2413-8, 2012.

[64] K. Barrie, S. Steinmann, A. Shin, R. Spinner and A. Bishop, "Gracilis free muscle transfer for restoration of function after complete brachial plexus avulsion," *Neurosurg Focus,* vol. 16, no. 5, pp. 1-9, 2004.

[65] C. Borselli, C. Cezar, D. Shvartsmana, V. H and D. Mooney, "The role of multifunctional delivery scaffold in the ability of cultured myoblasts to promote muscle regeneration," *Biomaterials,* vol. 32, no. 34, pp. 8905-8914, 2011.

[66] D. Shvartsman et al., "Sustained Delivery of VEGF Maintains Innervation and Promotes Reperfusion in Ischemic Skeletal Muscles Via NGF/GDNF Signaling," *Molecular Therapy,* vol. 22, no. 7, pp. 1243–1253, 2014.

[67] R. Dennis and P. Kosnik, "Excitability and isometric contractile properties of mammalian skeletal muscle constructs engineered in vitro," *In Vitro Cell Dev Biol Anim,* vol. 36, no. 5, pp. 327-335, 2000.

[68] J. Shansky et al., "A simplified method for tissue engineering skeletal muscle organoids in vitro," *In Vitro Cell Dev Biol Anim,* vol. 33, no. 9, pp. 659-661, 1997.

[69] L. Wang, J. Shansky and H. Vandenburgh, "Induced formation and maturation of acetylcholine receptor clusters in a defined 3D bio-artificial muscle," *Mol Neurobiol.,* vol. 48, no. 3, pp. 397-403, 2013.

[70] T. Kaufman et al., "Innervation of an engineered muscle graft for reconstruction of muscle defects," *Am J Transplantation,* doi: 10.1111/ajt.14957, 2018.

[71] C. Powell et al., "Tissue-engineered human bioartificial muscles expressing a foreign recombinant protein for gene therapy," *Hum Gene Ther,* vol. 10, no. 4, pp. 565-577, 1999.

[72] Y. Lu et al, "Recombinant vascular endothelial growth factor secreted from tissue-engineered bioartificial muscles promotes localized angiogenesis," *Circulation,* vol. 104, no. 5, pp. 594-599, 2001.

[73] A. Ruijs, J. Jaquet, S. Kalmijn, H. Giele and S. Hovius, "Median and Ulnar Nerve Injuries: A Meta-Analysis of Predictors of Motor and Sensory Recovery after Modern Microsurgical Nerve Repair," *Plast. Reconstr. Surg.,* vol. 116, no. 2, pp. 484-94, 2005.

[74] R. Pahwa and I. Jialal, "Chronic Inflammation," StatPearls Publishing, Treasure Island (FL), 2018.

CHAPTER 2:

M2 Macrophage Polarizing Cytokines can be Conjugated to Gold Nanoparticles and Direct Macrophage Polarization

2.1 Introduction

Uncontrolled inflammation contributes to the pathology of non-healing wounds and many chronic diseases. In fact, chronic inflammation contributes to the pathology of 7 of the 10 leading causes of death in the United States (CDC, 2016). Beyond the critical role the inflammatory response plays in host defense, it is now understood that immune cells also play a central role in initiating tissue regeneration and when dysregulated can inhibit healing and cause tissue damage. Macrophages, in particular, play a central role in orchestrating the transition from host defense to repair, as they can adopt both inflammatory (M1) and regenerative (M2) phenotypes. While a broad array of macrophage phenotypes are generated in response to complex cytokine environments in vivo [1], potent cytokine stimulators of various phenotypes have been identified in vitro. The inflammatory, M1 phenotype, is activated by interferon gamma (IFN-γ); a reparative, M2a phenotype, by interleukin-4 (IL-4) and IL-13; and an anti-inflammatory/reparative, M2c phenotype, by IL-10 [2]. Appropriately timed transition to the M2 phenotypes is critical for the regeneration of functional tissue and disease resolution. Many non-healing injuries, including diabetic ulcers [3], nerve and spinal cord injury [4], and some muscle injuries [5, 6] as well as many chronic and degenerative conditions including diabetes and metabolic disease [7], arthritis [8, 9] and muscular dystrophies [10] are associated with a stalled M1 to M2 macrophage transition.

Macrophage-based therapeutic strategies, and specifically, biomaterial systems designed to control macrophage polarization have generated much interest as a new strategy in regenerative medicine [11, 12, 13]. While macrophage polarizing cytokines, IL-4 in particular, have been widely explored as potential therapeutics in various inflammatory models [14, 15, 16], their use has been limited by their short in vivo half-lives, poor targeting, high dose requirements and systemic side effects [17]. Further, inhibition of inflammation by non-targeted systemic therapeutics, such as inhibition of tumor necrosis

factor-α (TNF-α) which is widely used to treat rheumatoid arthritis and inflammatory bowel disease (IBD), is associated with severe side effects often including immunosuppression [18]. Biomaterials provide unique advantages in their ability to target specific tissues and cell types of interest, and provide sustained stimuli to maintain appropriate macrophage polarization throughout the regenerative process.

Nanoparticles have been explored extensively for their use as drug delivery vectors and their ability to direct macrophage polarization [19]. Nanoparticles have been used to exploit the propensity of macrophages to patrol tissue and to find and internalize foreign material to target delivery to this cell type. While most research has focused on the effect of various nanoparticle material properties in promoting inflammation [19], more recently, various nanoparticles have been developed to deliver genetic material to macrophages. Various siRNAs, such as anti-TNFα and Map4k4, and plasmid DNAs, coding IL-4 and IL-10, have been loaded into nanoparticles to promote the M1 to M2 polarization transition in the contexts of arthritis and IBD [20, 21, 22, 23, 24]. Gold nanoparticles (AuNPs) are particularity attractive as a delivery vector, as they are not toxic, can be synthesized with a monodisperse size distribution over a clinically relevant range, and allow easy surface modifications [25]. Further, covalent coupling of proteins to AuNPs can enhance their in vivo stability and therapeutic efficacy. Conjugation of TNF-α to PEGylated AuNPs was shown to target delivery to solid tumors and delay tumor growth in mice [26], and allowed for the safe administration of TNF-α at doses 3-times greater than the maximum tolerated dose for native TNF-α in a phase I clinical trial [27].

While many nanoparticle designs have focused on the induction of the M1 phenotype, and have shown clinical success, comparatively very few nanoparticles to induce M2 phenotypes have been reported [19]. The aim of the work presented here is to develop AuNPs to direct M2 macrophage polarization by the conjugation of M2 polarizing cytokines to the surface of the AuNPs in such a way that their bioactivity is preserved. Bioactivity of the particles was assessed by their ability to promote the polarization of both naïve and M1 human macrophages towards M2 phenotypes in vitro. The

methodologies developed here for the conjugation of IL-4, IL-13, and IL-10 will likely be applicable for the conjugation of other cytokines of interest.

2.2 Materials and Methods

2.2.1 Synthesis of 30nm AuNPs

AuNPs were synthesized by the hydroquinone reduction of gold onto citrate stabilized seed particles [28]. Briefly, to make 15nm seed particles, 1mL of 1%w/v gold chloride (Sigma #254169) solution was added to 100mL of milliQ water in a clean Erlenmeyer flask, stirred slowly and heated on a 400^{o}C plate. As soon as the solution came to a boil, the stirring was set as fast as possible without splashing, and 3mL of 1% w/v sodium citrate (Sigma # 4641) was rapidly added. The solution color changed from clear to purple to red over the course of ~5min, a few minutes after the color changes completed, the solution was cooled at room temperature.

The 30nm AuNPs were then synthesized by the reduction of ionic gold onto the 15nm seed particles by hydroquinone. MilliQ water was added to an Erlenmeyer flask followed by 25mM gold chloride solution, and 15nm seed particles. The solution was spun as fast as possible without splashing and then 15mM sodium citrate and 25mM hydroquinone were added simultaneously. The volume of each solution added to the hydroquinone reduction reaction depended on the desired nanoparticle size, and have been published previously [29]. The solution color changed from red to black and then to a darker red. The reaction was completed in a few minutes; then particles were stored at room temperature.

2.2.2 Direct conjugation of PEG-SH, IL-4, IL-13 and IL-10 to AuNPs

For cell experiments, AuNPs were sterilized by filtration through a 0.2μm filter before further modifications were made. Following synthesis, AuNPs were divided into 1mL aliquots in UV sterilized (9999 x 100 μJ/cm^2, 30min) Eppendorf tubes and pelleted via centrifugation (6600xg, 15min, 4°C); one aliquot was resuspended at 1x concentration in MilliQ water and the dynamic light scattering (DLS) size

and absorbance were measured. The size and absorbance were used to calculate AuNP concentration using the Beer-Lambert Law.

All subsequent AuNP conjugation reactions were performed in UV sterilized (9999 x 100 μJ/cm^2, 30min) low binding Eppendorf tubes. In experiments without PEGylation, following centrifugation, the AuNPs were resuspended in MilliQ water to the same concentration as the AuNP synthesis solution (i.e. they were resuspended in the same volume), and the desired amount of protein was added to the solution such that the total conjugation reaction volume was doubled by the addition of protein. In experiments involving the concurrent conjugation of PEG and protein ligand, the desired concentration of PEG-SH was also added to the conjugation reaction at this time. Protein and/or PEG conjugation was allowed to occur overnight at room temperature, on a slow shaker.

For sequential PEGylation then protein conjugation, following centrifugation, the AuNPs were resuspended in milliQ water containing 5kDa methoxy PEG-SH (Laysan Bio, Inc) to a final concentration 15x more concentrated than the AuNP synthesis solution. AuNP-PEG particles used as a control in cell experiments were provided enough PEG to saturate the surface, 5 ligands/nm^2, according to published data [28]. Particles used for the subsequent conjugation of protein were provided 2.5 PEG ligands/nm^2. PEGylation was allowed to occur overnight at room temperature, on a slow shaker. Following overnight PEGylation, the desired concentration of recombinant human or murine IL-4 or IL-10 (Peprotech) was added to the reaction along with trehalose (Sigma #T0167). The addition of trehalose was critical to avoid protein loss in low concentration solutions; the final concentration of trehalose was 10% w/v. Protein conjugation was allowed to occur overnight at room temperature, on a slow shaker.

2.2.3 IL-4 Conjugation to AuNP via a PEG linker

For the conjugation of IL-4 through a PEG linker 5kDa heterobifunctional thiol-PEG-carboxylate (Sigma #757845) was conjugated to the AuNP core as described above with 5 ligands/nm^2. Following overnight the PEGylation the particles were separated into 200μL aliquots in UV sterilized low binding

Eppendorf tubes, and spun at 6600xg, 10min, 4°C. They were resuspended in MilliQ water two times to remove unbound thiol-PEG- carboxylate, and finally resuspended at 15x concentration in MES buffer, pH 6.0. EDC (Sigma# E7750) was then added to the AuNPs to give a final concentration of 0.5mg EDC/mL, and immediately followed by sulfo-NHS (Thermo scientific #24510) to give a final concentration of 1.38 sulfo-NHS/mL. The reaction was allowed to proceed for 30min at room temperature. Finally, the particles were spun at 6600xg, 10min, 4°C and resuspended in PBS containing recombinant human IL-4 (Peprotech). IL-4 was added to the reaction at a ratio of 0.33 IL-4 ligands/nm^2. IL-4 was allowed to react overnight in the dark. Subsequently particles were washed by centrifugation, as described below.

2.2.4 Tracking AuNP surface modification and quantification of protein loading density.

Following AuNP synthesis, PEGylation and/or protein conjugation, the particles were resuspended in MilliQ water and the DLS size and ζ-potential were measured.

Subtractive analysis was used to quantify protein loading. Unbound protein and trehalose were removed by centrifugation following overnight conjugation, four washes in MilliQ water in total. To reduce the required spin durations, conjugated AuNPs were separated into 200uL aliquots in UV sterilized low binding Eppendorf tubes. Particles lacking PEG required long spin durations at slow speeds to avoid aggregation (Appendix A, Fig. A1). PEGylated AuNPs were spun at 5000xg, 15min, 4°C. The supernatants were collected and unbound protein was quantified with LavaPep (Gel Company #LP-022010). Care was taken to include 10%w/v trehalose in the LavaPep standard curve to ensure accurate measurement of protein concentration in the first supernatant. Subtractive analysis was used to quantify protein loading, and ligand density was calculated using the known concentration and size of the AuNPs provided in the conjugation reaction.

2.2.5 THP-1 Cell Culture and AuNP Bioactivity Assays

THP-1 cells (ATCC® TIB-202™) were cultured in RPMI-1640 media (containing 10% Heat Inactivated (HI)-FBS) as recommended by ATCC, except 2-mercaptoethanol was excluded. To differentiate the THP-1 monocytes to macrophages, cells were seeded at 10^6cells/well in non-TC treated 6-well plates with 2mL media/well containing 100ng/mL phorbol 12-myristate 13-acetate (PMA). After 3 days, the PMA-media was removed, washed off the cells with PBS, and then macrophage polarizing cytokines were added to the culture. For all experiments an equivalent dose of soluble cytokine or AuNP conjugated cytokine was added to the culture: 20ng/mL IL-4, except where otherwise noted, 20ng/mL IL-13, or 40ng/mL IL-10. Complete RPMI media without any added cytokines, and AuNP-PEG administered at a dose equivalent to the AuNP dose used in the cytokine conditions were used as negative controls. Polarization media was changed daily and macrophage polarization assessed by flow cytometry on day 3 following the addition of cytokines.

2.2.6 M1 to M2 Switching Assay

Following PMA differentiation of THP-1 cells, they were cultured in media containing 20ng/mL IFN-γ + 2400ng/mL lipopolysaccharide (LPS) for 2 days to induce the M1 phenotype. Subsequently, this media was replaced with media containing 40ng/mL IL-4 and/or 40ng/mL IL-10 delivered as soluble or AuNP conjugated cytokines. Polarization media was changed daily and macrophage polarization assessed by flow cytometry on day 5 following the addition of the M2 polarizing cytokines.

2.2.7 Flow Cytometry

Cell viability was assessed by staining with calcein AM or a fixable dead cell stain (Invitrogen) according to the manufacture instructions. Briefly, for calcein AM staining the cells were incubated in 4μM calcein AM in complete culture media containing 10% HI-FBS at 37°C, 5% CO_2, for 30min. Then the cells were harvested and stained for flow cytometry as described below. Macrophages were harvested using Accutase (ThermoFisher Scientific #A1110501) followed by scrapping. For experiments were the

fixable dead cell stain (Invitrogen) was used, following harvesting, the cells were incubated in PBS containing the viability dye at the concentration recommended by the manufacture at 4°C for 30min-1hr, protected from light. Then the cells were stained for flow cytometry as described below.

Standard flow cytometry protocols were followed. Briefly, macrophages were blocked with Fc receptor blocking solution (Human TruStain FcXTM, BioLegend #422302) and stained with the following antibodies: CD206-PE (BioLegend #321106) or CD206-APC (BioLegend #321110), CCR7-APC (BioLegend #353214) or CCR7-Pacific Blue (BioLegend #353210), and CD163-FITC (BioLegend #333618) at the concentrations recommended by the manufacturer. Unstained cells, and the isotype controls recommended by the manufacture were used as controls in the gating. With the exception of when calcein AM was used, the cells were fixed and stored in 0.4% PFA at 4°C until they were run on an LSR II flow cytometer, within 3 days following staining. Analysis was performed using FlowJo7.6 software.

2.2.8 Statistics

All analyses were performed using GraphPad Prism5 software. Statistical comparisons were performed by one way analysis of variance (ANOVA) with Tukey or Bonferroni post hoc tests. P values less than 0.05 were considered significant.

2.3 Results

2.3.1 The M2 macrophage polarizing cytokines, IL-4, IL-13, and IL-10 can be directly conjugated to AuNPs.

AuNPs were synthesized by the hydroquinone reduction of Au onto citrate stabilized seed particles [28]. Following centrifugation and washing with water to remove excess citrate ions, the M2 macrophage polarizing cytokines, IL-4, IL-13 and IL-10, were directly conjugated to the AuNP surface

(Fig. 2.1 A). Human IL-4, IL-13, and IL-10 (Fig. 2.1 B-D), as well as the murine homologues, contain disulfide bonds capable of covalently binding to Au through the formation of thiol-Au bonds [30]. All of these proteins also have isoelectric points that render them positively charged at neutral pH (Table 2.1) [31], suggesting that they may also bind to AuNPs via electrostatic interactions. In a typical conjugation reaction, following the hydroquinone growth of AuNPs to 30nm diameter, AuNPs were spun at 6600xg for 15min. and resuspended in MilliQ water. Protein was added to the AuNP solution and conjugation was allowed to occur overnight at room temperature.

Table 2.1. Isoelectric points for human and murine M2 macrophage polarizing cytokines [31]

	Human	**Murine**
IL-4	9.17	8.18
IL-13	8.69	8.34
IL-10	8.19	8.45

Protein conjugation to the AuNPs was tracked by measuring surface ζ-potential in MilliQ water, and conjugation efficiency was calculated based on subtractive analysis. In order improve protein conjugation efficiency and increase ligand density, increasing concentrations of human IL-4 were provided in the conjugation reaction. As expected, increasing the IL-4-to-AuNP stoichiometry resulted in increased conjugation efficiency (Fig. 2.1 E) and IL-4 ligand density (Fig. 2.1 F). Further, increasing IL-4 ligand density resulted in increased ζ-potential (Fig. 2.1 G), suggesting that the AuNP surface had been modified as expected.

AuNP surface conjugation, as well as stability, was assessed by using DLS to measure the hydrodynamic diameter of the particles. Following hydroquinone growth, the AuNPs were monodisperse around a 30nm diameter. Following IL-4 conjugation, the hydrodynamic diameter grew to about 50-80nm

for AuNPs with the highest and lowest tested IL-4 ligand densities, respectively, immediately following IL-4 conjugation (Appendix A, Fig. A1 A). Following centrifugation to remove unbound IL-4, AuNP-IL4 particles with the lowest ligand densities demonstrated the most significant particle aggregation; particles with greater IL-4 ligand density were more stable and demonstrated minimal aggregation following washing (Fig. 2.1 H). AuNP-IL4 particles are susceptible to aggregation following centrifugation, even at the highest ligand densities tested. Such aggregation can be minimized by adjusting the centrifugal force (Appendix A, Fig. A1 B).

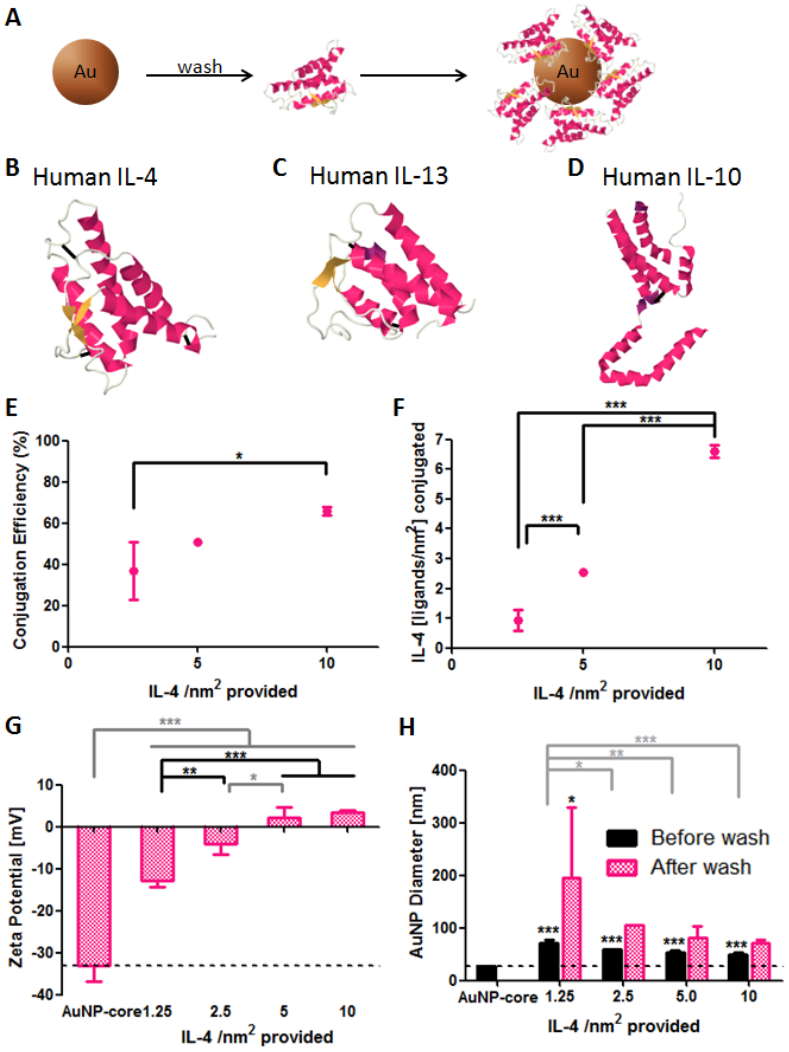


Figure 2.1. The M2 macrophage polarizing cytokines, IL-4, IL-13, and IL-10 can be directly conjugated to AuNPs, and conjugation tracked with NP ζ-potential and size. (A) Schematic showing the direct conjugation of protein (IL-4 shown) to the surface of AuNPs following a wash step to remove excess citrate ions from the surface of the AuNPs. (B-D) Crystal structure of human IL-4 (B), human IL-13 (C), and human IL-10 (D) showing that all contain disulfide bonds (shown in black) capable of binding to Au. (E) Conjugation efficiency, the percentage of IL-4 provided that was ultimately conjugated to the AuNP surface, increases as increasing amounts of IL-4 are provided (x-axis) in the conjugation reaction. (F) IL-4 ligand spacing on the surface of AuNPs (y-axis) increases as increasing amounts of IL-4 are provided (x-axis) in the conjugation reaction. (G) The ζ-potential in MilliQ water becomes less negative as increasing amounts of IL-4 are conjugated to the AuNP surface. (H) Hydrodynamic diameter of AuNPs in MilliQ water increases following IL-4 conjugation, and subsequent was steps. Increasing levels of IL-4 conjugation minimize particle growth following the wash steps. All data are means ±SD, n=3.*P<0.05, **P<0.01, ***P<0.001

The conjugation of human IL-13 to AuNPs was tracked with ζ-potential and DLS, as just described for IL-4. Similarly, increasing IL-13 ligand density increased the ζ-potential (Fig. 2.2 A), suggesting that surface modification occurred as expected. Further, the hydrodynamic diameter of the AuNP core particles grew following IL-13 conjugation. However, for IL-13, the greatest ligand densities tested resulted in the most significant levels of aggregation (Fig. 2.2 B,C). When the same ligand densities were used for IL-4 conjugation, the highest ligand densities resulted in the least aggregation (Fig. 2.3 A,B). These trends in particle size stability were also evident in the DLS polydispersity indices (PDIs) (Fig. 2.3 C,D). AuNP-IL13 particles demonstrated increased size stability at lower ligand densities (0.5 IL-13 ligands/nm^2 provided in the conjugation reaction).

In order to assess AuNP-IL4 and AuNP-IL13 stability in a biologically relevant environment, the particles were incubated in complete RPMI1640 cell culture media containing 10% HI-FBS at 37°C, 5% CO_2, and DLS was used to measure the hydrodynamic diameter for 4 days. The most stable formulations of AuNP-IL4 and AuNP-IL13, 5 IL-4 and 0.5 or 0.25 IL-13 ligands/nm^2, were used. As expected, the hydrodynamic diameter grew over the first 24 hrs, likely due to serum protein adsorption, for both the AuNP-IL4 and AuNP-IL13 particles before stabilizing for the remaining 3 days (Fig. 2.2 D).

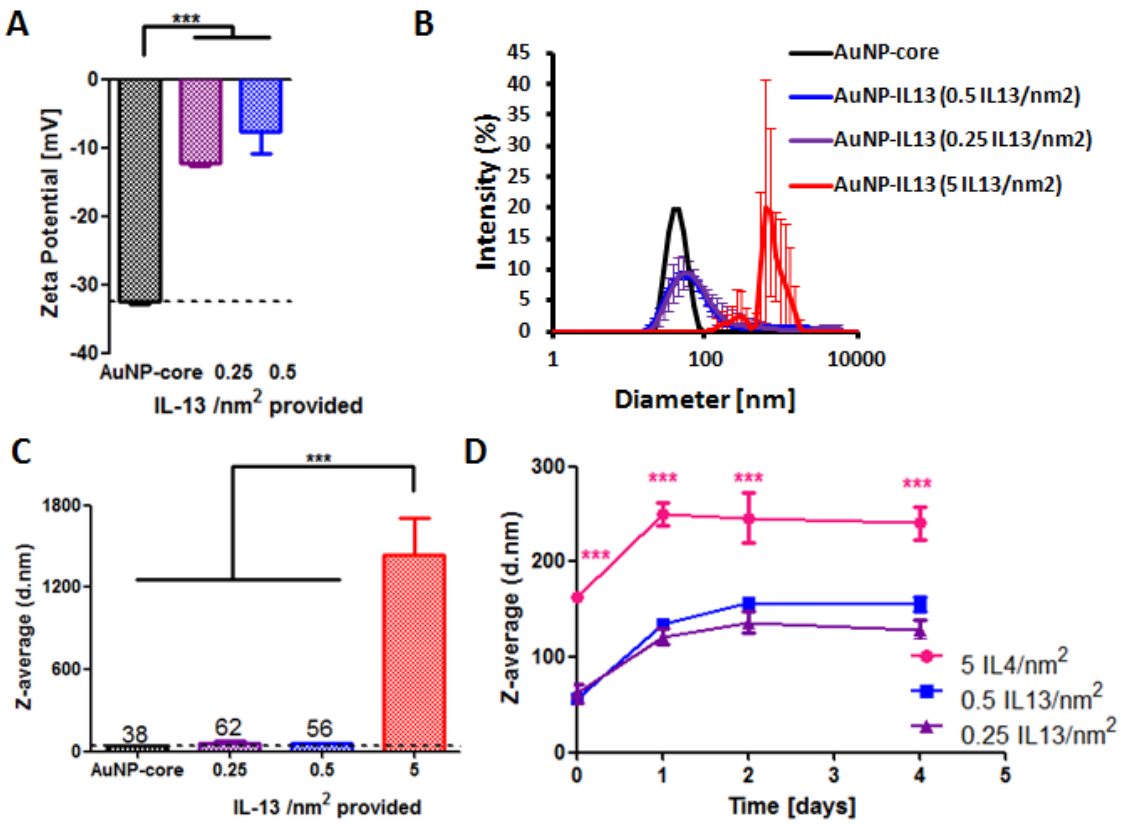


Figure 2.2. IL-4 and IL-13 conjugated AuNPs are stable in cell culture media. (A) The ζ-potential in MilliQ water becomes less negative as increasing amounts of IL-13 are conjugated to the AuNP surface. Data are means ±SD, n=3. ***P<0.001 (B) DLS size distribution in MilliQ water following conjugation with increasing amounts of IL-13. Data are means ±SD, n=3. (C) Hydrodynamic diameter of AuNPs in MilliQ water increases following IL-13 conjugation. Data are means ±SD, n=3. ***P<0.001 (D) Hydrodynamic diameter of IL-4 (pink) and IL-13 (blue and purple) conjugated AuNPs following incubation in complete RPMI1640 cell culture media (containing 10% HI-FBS), at 37°C. Data are means ±SEM, n=3. ***P<0.001 for IL-4 vs. IL-13 conditions

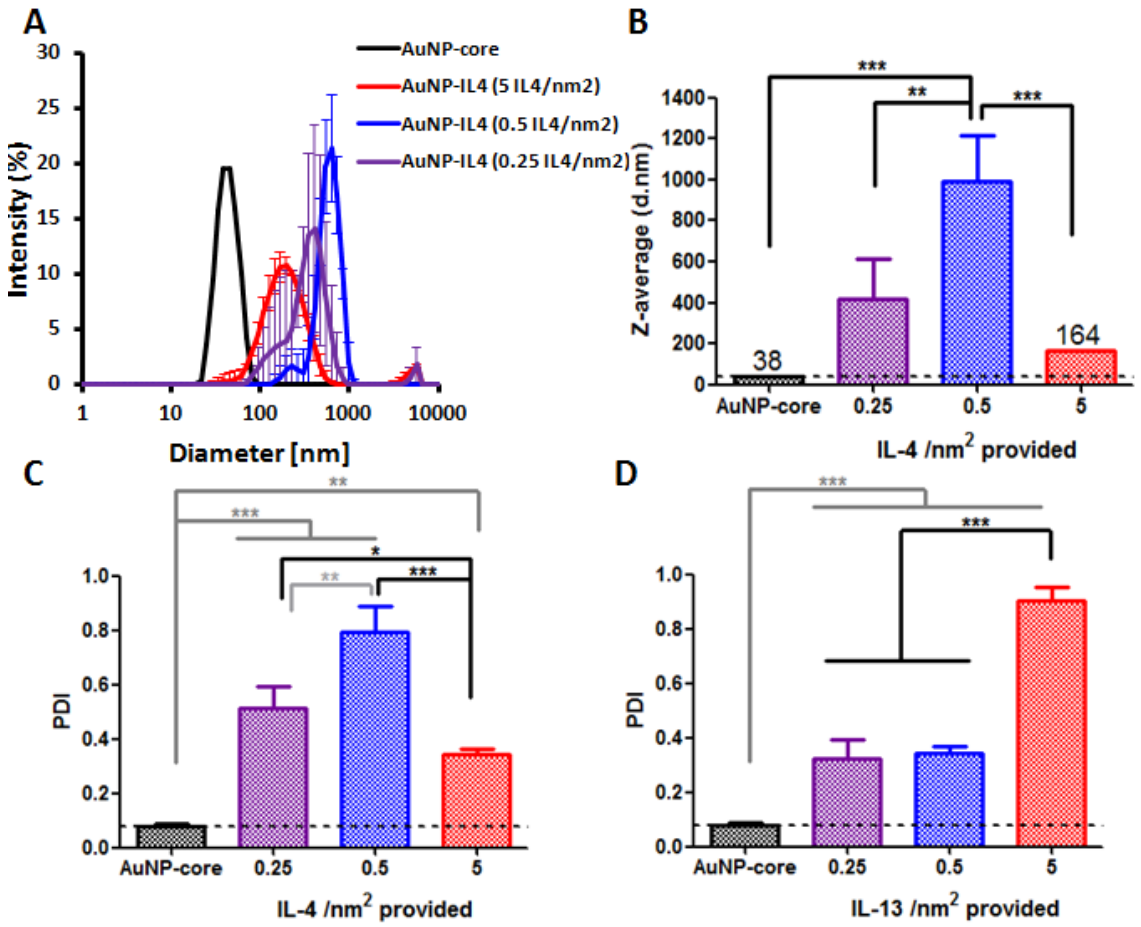


Figure 2.3. 5 IL-4 ligands/nm2 and 0.5 IL-13 ligands/nm2 provide the most stable AuNPs. (A) DLS size distribution of the AuNP core and AuNP-IL4 particles following conjugation reactions where 5 (red), 0.5 (blue), or 0.25 (purple) IL-4 ligands/nm^2 were provided in the conjugation reaction. Data are means ±SD, n=3. (B) Hydrodynamic diameter of AuNPs in MilliQ water following conjugation of IL-4. Data are means ±SD, n=3. **P<0.01, ***P<0.001 (C) Polydispersity index (PDI) of AuNPs in MilliQ water. Data are means ±SD, n=3. *P<0.05, **P<0.01, ***P<0.001 (D) PDI of AuNP-IL3 in MilliQ water. Data are means ±SD, n=3. ***P<0.001

2.3.2 IL-4 and IL-13 conjugated AuNPs direct human macrophage polarization towards the M2a phenotype in vitro.

The ability of AuNP-IL4 and AuNP-IL13 to direct M2a polarization was assessed in vitro with THP-1 derived human macrophages. AuNP-IL4 and AuNP-IL13 particles were synthesized according to the parameters described above and characterized (Appendix A, Table A1). For the in vitro bioactivity

assay, equivalent doses of soluble cytokine (40ng/mL IL-4 or 20ng/mL IL-13) and AuNP conjugated cytokine were administered, and flow cytometry was used to assess macrophage polarization. For both IL-4 and IL-13, the AuNP conjugated cytokines upregulated CD206 expression to the same extent as soluble cytokines (Fig. 2.4 A,B; Fig. 2.5), suggesting that the conjugated proteins retained full bioactivity. Further, neither AuNP-IL4 nor AuNP-IL13 upregulated expression of CCR7 (a marker of the inflammatory M1 phenotype), as compared to macrophages that were not stimulated with any cytokines (M0), suggesting that the particles were not inflammatory (Fig. 2.4 C). Neither AuNP-IL4 nor AuNP-IL13 had a substantial effect on macrophage viability (Fig. 2.4 E). Importantly, there was no difference in the percentage of macrophages specifically expressing the non-inflammatory M2a polarization state (CD206+/CCR7-) between the AuNP conjugated and soluble cytokine treatment groups (Fig. 2.4 F).

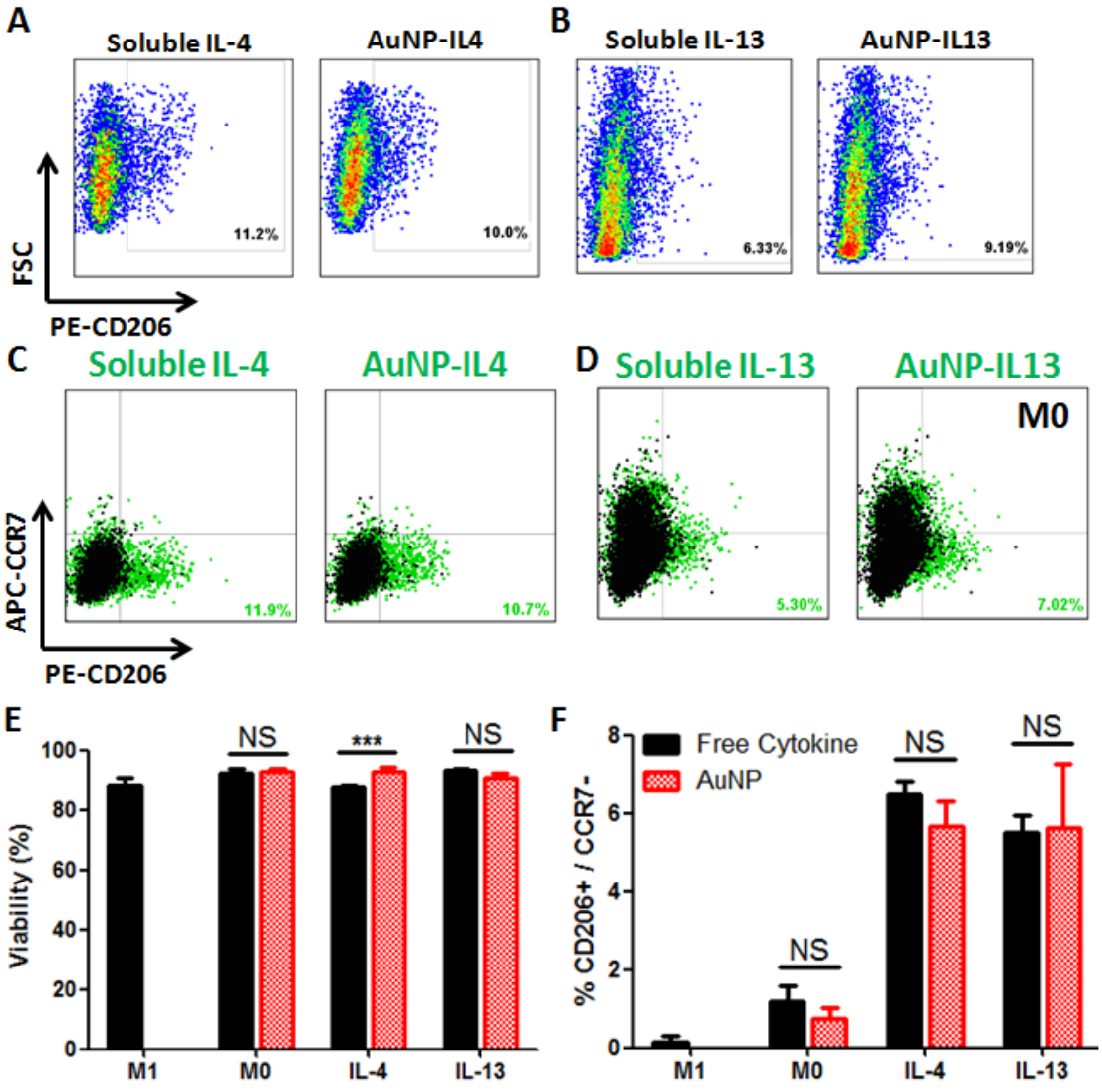


Figure 2.4. IL-4 and IL-13 conjugated AuNPs are not cytotoxic or inflammatory, and direct M2a macrophage polarization. (A,B) Representative FACS scatter plots showing comparable upregulation of CD206, a marker of M2a polarization, in response to soluble IL-4 and AuNP-IL4, or soluble IL-13 and AuNP-IL13, respectively. (C,D) Representative FACS plots showing expression of the inflammatory marker (CCR7) and the M2a marker (CD206) in response to soluble IL4 or AuNP-IL4, and soluble IL-13 or AuNP-IL13 respectively. Macrophages not exposed to any cytokines are shown in black. (E) Macrophage viability assessed using a calcein AM viability stain and flow cytometry in response to LPS and IFN-γ (M1), no cytokine stimulation (M0, black), soluble IL-4 (IL-4, black), soluble IL-13 (IL13, black); or AuNP-PEG (M0, red), AuNP-IL4 (IL4, red), or AuNP-IL13 (IL-13, red). (F) Percentage of macrophages expressing the M2a phenotype (CD206+/CCR7-). All data are means ±SD; n=6 for M1 and M0, n=3 for IL-4 and IL-13 conditions. ***P<0.001, NS = not statistically significant

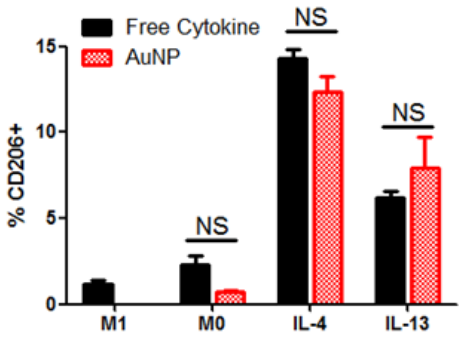


Figure 2.5. AuNP-IL4 and AuNP-IL13 are able to direct M2a macrophage polarization. FACS data showing upregulation of CD206 (M2a marker) on THP-1 derived human macrophages in response to soluble IL-4 (IL-4, black), soluble IL-13 (IL-13, black), or an equivalent dose of AuNP-IL4 (IL-4, red) or AuNP-IL13 (IL-13, red). Media lacking cytokines (M0, black) or AuNP-PEG (M0, red) was used as a negative control. Stimulation with LPS and IFN-γ was used as an M1 control. Data are means ±SD; n=6 for M1 and M0, n=3 for IL-4 and IL-13 conditions. NS = not statistically significant

2.3.3 Generation of PEGylated, IL-4 and IL-13 AuNPs

In order to increase the stability of IL-4 and IL-13 conjugated nanoparticles, the AuNP-cores were partially coated with thiolated, methoxy-terminated 5kDa PEG (Fig. 2.6 A). By only partially PEGylating the AuNP surface [28], macrophage polarizing cytokines could be directly conjugated to the remaining Au surface (Fig. 2.6 B). A 1:1 protein:PEG ratio was used, with enough protein and PEG provided in the conjugation reaction to maximally yield 2.5 protein and 2.5 PEG ligands/nm^2. Sequentially PEGylating the AuNP then conjugating the protein was essential to avoid particle aggregation. A monodisperse DLS size distribution shifted to the right following partial PEGylation and IL-4 or IL-13 conjugation; however, simultaneous addition of PEG and protein to the AuNP conjugation reaction resulted in large particle aggregation (Fig. 2.6 C,D). The slight increase in particle size following PEGylation and IL-4 or IL-13 conjugation was manifested in the increased hydrodynamic diameter of the particles (Fig. 2.6 E). Further, sequential PEGylation then protein conjugation resulted in monodisperse particle sizes, as indicated by the low PDI (Fig. 2.6 F). The conjugation efficiency and ligand density of

conjugated IL-4 and IL-13 were calculated using subtractive analysis. Importantly, both IL-4 and IL-13 demonstrated high levels of conjugation and ligand density following PEGylation (Fig. 2.6 G,H) suggesting that initially PEGylating the AuNP did not significantly inhibit cytokine conjugation.

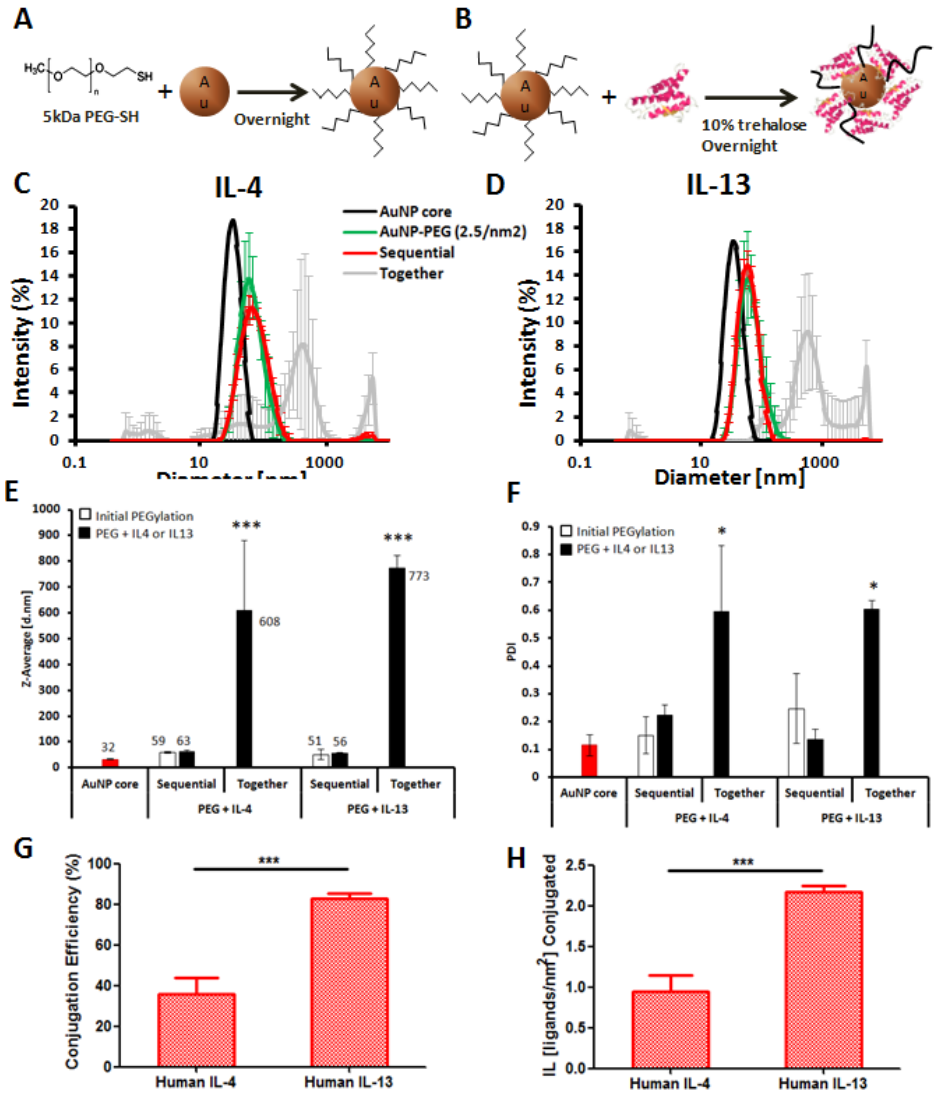


Figure 2.6. Sequential PEGylation then IL-4 or IL-13 conjugation. (A-B) Schematic showing partial PEGylation and subsequent IL-4 conjugation to AuNPs. (C,D) DLS size distribution in MilliQ water of the AuNP core (black), following sequential partial PEGylation (green), then human IL-4 (C) or IL-13 (D) conjugation (red), and concurrent PEGylation and protein conjugation (gray). (E) Hydrodynamic diameter of AuNPs in MilliQ water. (F) Polydispersity index (PDI) of AuNPs in MilliQ water. (G) Loading of IL-4 and IL-13 following partial PEGylation of AuNPs. (H) Conjugation efficiency, the percentage of protein provided that was ultimately conjugated to the AuNP surface, following partial PEGylation. All data are means ±SD, n=3. *P<0.05, ***P<0.001 vs all other conditions. There is no significant difference between the "together IL-4" and "together IL-13" conditions.

As an alternative to mixed PEG and protein monolayers, which may interfere with protein bioactivity due to steric hindrance from PEG, IL-4 was also conjugated via a PEG linker using EDC/NHS chemistry (Fig. 2.7 A). In an initial step AuNPs were PEGylated with 5kDa heterobifunctional thiol-PEG-carboxylate via thiol gold bonds. Enough thiol-PEG-carboxylate was provided to saturate the AuNP surface (5 ligands/nm^2) [28]. Subsequently, EDC/NHS chemistry was used to conjugate human IL-4 to the carboxyl group terminating the PEG linker. The resultant AuNP-PEG-IL4 particles were monodisperse around 49nm diameter (Fig. 2.7 B), with a PDI of 0.089 and ζ-potential of -28.6mV. Ultimately, 0.2 IL-4 ligands/nm^2 were conjugated, representing a conjugation efficiency of 60%.

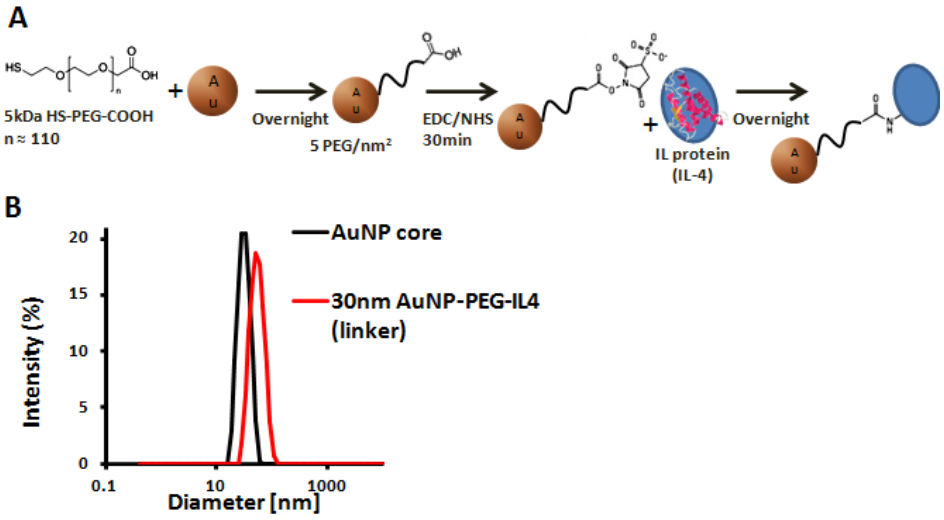


Figure 2.7. Conjugation of IL-4 to AuNP via EDC-NHS chemistry with a PEG linker. (A) Schematic showing partial PEGylation of AuNPs with heterobifunctional thiol-PEG-carboxylate and subsequent IL-4 conjugation to the PEG carboxylate group via EDC/NHS chemistry. (B) DLS size distribution of the AuNP core and AuNP-PEG-IL4 in MilliQ water.

2.3.4 PEGylation does not interfere with bioactivity.

In order to determine if PEGylation inhibited bioactivity of the conjugated cytokine, the ability of PEG-AuNP-IL4 particles to direct THP-1 derived macrophage polarization in vitro was assessed. As before, the same dose of IL-4 was administered either as soluble cytokine, or as PEG-AuNP-IL4.

PEGylated AuNPs lacking cytokine, and basal media were used as negative controls. PEG-AuNP-IL4 upregulated the marker of M2a polarization, CD206, without upregulating expression of the marker of inflammatory M1 polarization, CCR7 (Fig. 2.8 A). Further, AuNP presentation of IL-4 tended to stimulate levels of CD206 expression higher than those stimulated by soluble IL-4 (Fig. 2.8 A). As expected, PEG-AuNP-IL4 did not have a substantial effect on macrophage viability (Fig. 2.8 B). Importantly, the percentage of macrophages specifically expressing the M2a phenotype (CD206+/CCR7-) was the same between groups stimulated with soluble IL-4 and PEG-AuNP-IL4 (Fig. 2.8 C), suggesting that PEGylation of AuNPs did not interfere with the bioactivity of conjugated human IL-4.

Similarly, particles synthesized via IL-4 conjugation through a PEG linker did not have any substantial effect on macrophage viability (Fig. 2.8 D), nor did they upregulate expression of the inflammatory marker, CCR7. Further, IL-4 conjugated through a PEG linker retained full bioactivity and the percentage of macrophages driven towards M2a polarization in response to these particles was the same as that observed in response to a matched dose of soluble IL-4 (Fig. 2.8 E).

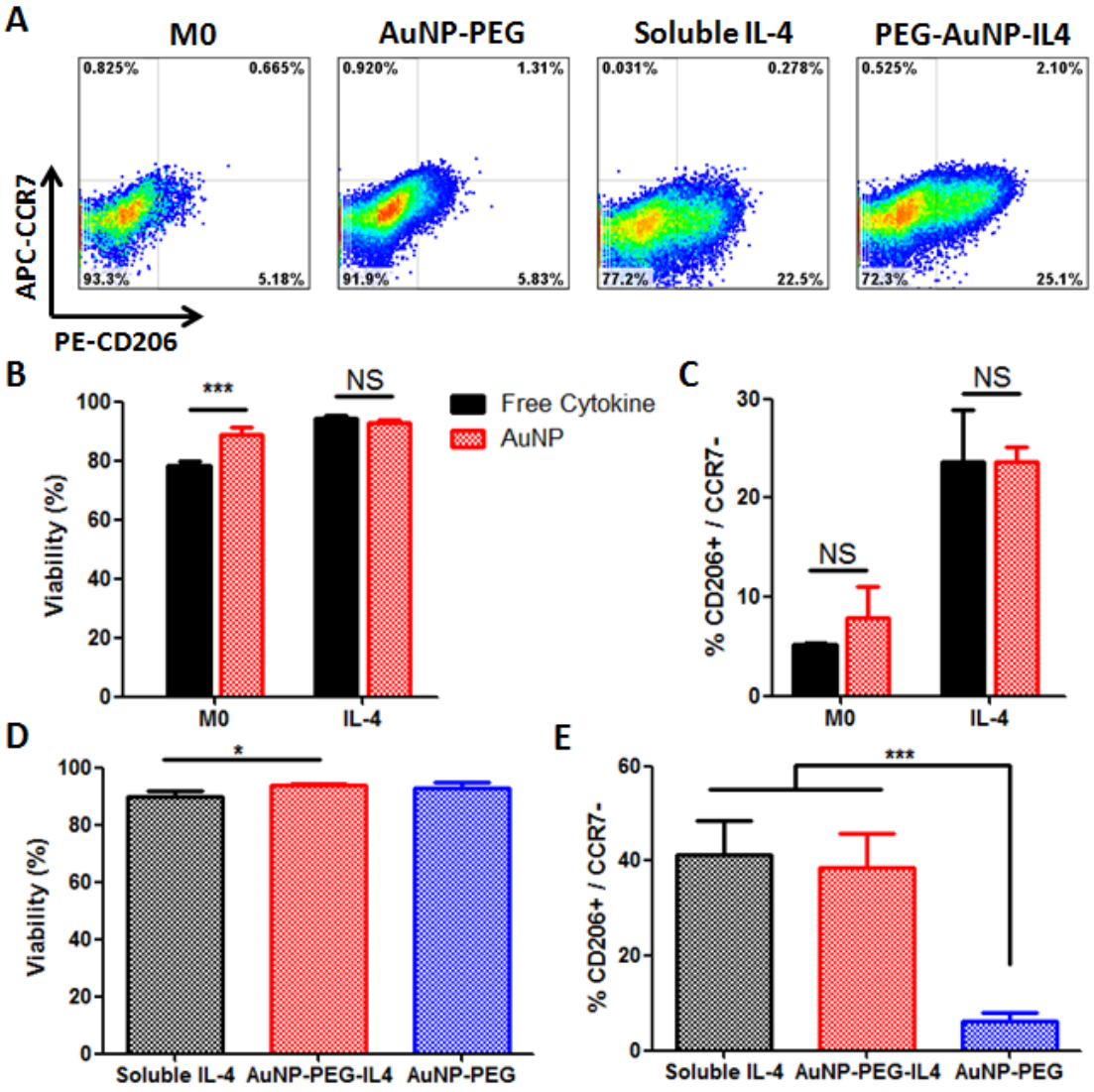


Figure 2.8. PEG-AuNP-IL4 particles direct M2a macrophage polarization. (A) Representative FACS scatter plots showing expression of the inflammatory (CCR7) vs the M2a (CD206) polarization marker. (B) Macrophage viability assessed using a fixable dead cell stain (Invitrogen) and flow cytometry in response to no cytokine stimulation (M0, black), soluble IL-4 (IL-4, black), AuNP-PEG (M0, red), or PEG-AuNP-IL4 (IL-4, red). (C) Percentage of macrophages expressing the M2a phenotype (CD206+/CCR7-). (D) Macrophage viability assessed using a fixable dead cell stain (Invitrogen) and flow cytometry in response to 20ng/mL IL-4 delivered as soluble IL-4, AuNP-PEG-IL4, or a comparable dose of AuNP-PEG as a negative control. (E) Percentage of macrophages expressing the M2a phenotype (CD206+/CCR7-). All data are means ±SD, n=3. *P<0.05, **P<0.01, ***P<0.001 NS = not statistically significant

2.3.5 Optimization of PEGylation and cytokine ligand densities

Having established that PEGylation does not interfere with the bioactivity of conjugated IL-4, the optimal cytokine:PEG ligand densities for mixed monolayers were next explored. Increasing the cytokine:PEG ratio, and increasing the total ligand density tended to increase particle aggregation (Fig. 2.9 A). Maintaining a1:1 cytokine:PEG ratio was important to minimize particle aggregation, achieve a low PDI, and maintain a small hydrodynamic diameter following both human IL-4 and IL-13 conjugation (Fig. 2.9 B; Fig. 2.10).

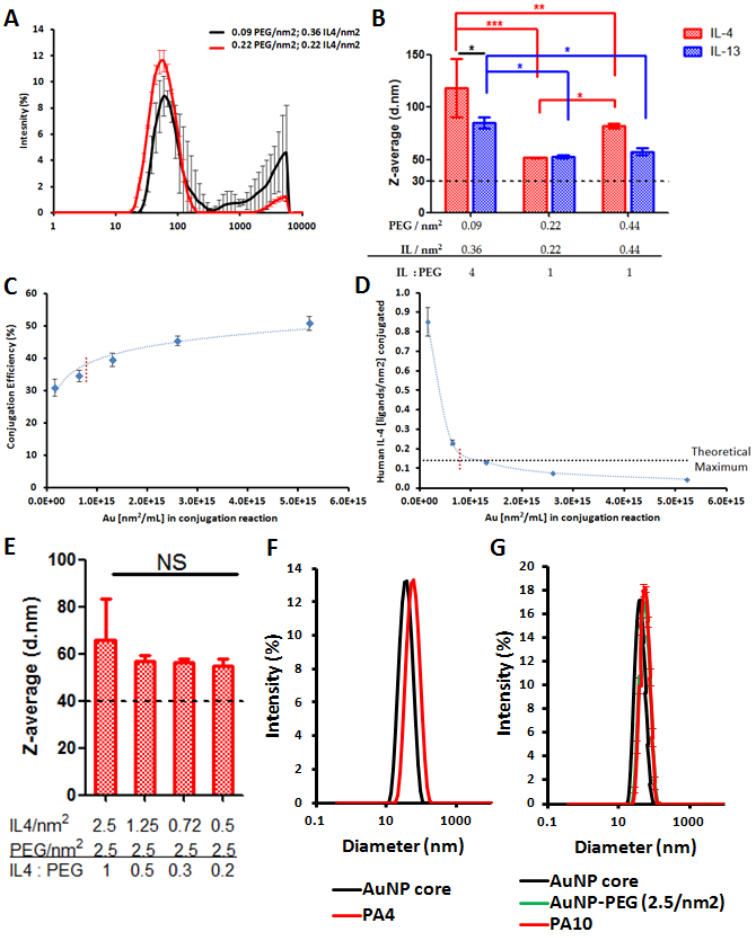


Figure 2.9. Optimization of PEGylation, and protein loading onto AuNPs. (A) DLS size distribution of PEG-AuNP-IL4 particles with a 1:1 (red) vs 4:1 (black) IL-4:PEG ligand ratio in MilliQ water. (B) Hydrodynamic diameter of PEG-AuNP-IL4 (red) and PEG-AuNP-IL13 (blue) particles in MilliQ water with varying ligand densities and protein:PEG ratios. (C) The conjugation efficiency of IL-4, following partial PEGylation, increases as increasing amounts of AuNP-PEGs are provided (x-axis) in the conjugation reaction. The concentration of IL-4 provided in the conjugation reaction was kept constant. The vertical red line indicates parameters that were used for later cell experiments. (D) IL-4 ligand density in response to increasing AuNP-PEG concentration, but constant IL-4 concentration, provided in the conjugation reaction. Horizontal black line represents the theoretical maximum IL-4 loading capacity based on sphere packing calculations, modeling IL-4 as spheres that are packed onto a spherical AuNP core. The vertical red line indicates parameters that were used for later cell experiments. (E) Hydrodynamic diameter of PEG-AuNP-IL4 resulting from decreasing the IL-4:PEG ratio < 1. (F,G) Representative DLS size distribution of the AuNP core and PEG-AuNP-IL4 (F) and PEG-AuNP-IL10 (G) particles in MilliQ water resulting from the optimized parameters (2.5 PEG and 0.5 recombinant human protein ligands/nm^2 provided in the conjugation reaction). All data are means ±SD, n=3. *P<0.05, **P<0.01, ***P<0.001 NS = not statistically significant

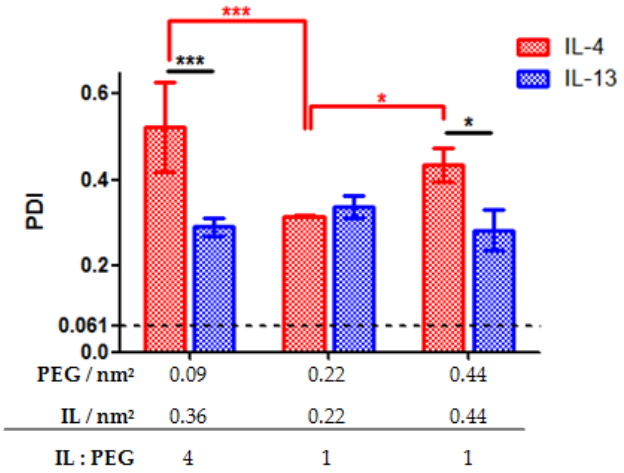
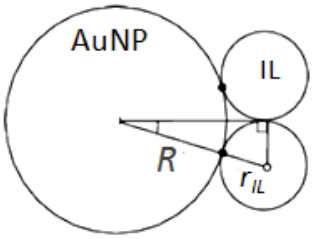


Figure 2.10. Polydispersity index (PDI) of PEG-AuNP-IL4 (red) and PEG-AuNP-IL13 (blue) particles in MilliQ water with varying ligand densities and protein:PEG ratios. The dotted line indicates the PDI of the AuNP core particles prior to any surface modification. Data are means ±SD, n=3. *P<0.05, ***P<0.001

The stability provided by partial PEGylation allowed the AuNPs to be resuspended at much higher concentrations without aggregation. This allowed the protein-to-AuNP stoichiometry to be significantly decreased, and therefore also decrease the protein:PEG ratio, without minimizing the protein concentration provided in the conjugation reaction. This provided an important technical advantage, and allowed a much greater range of stoichiometries to be explored, because low protein concentrations are impractical due to the high percentage loss to vial walls. Importantly, decreasing the protein:PEG ratio may increase particle stability. In the optimization experiment, AuNPs were PEGylated with 2.5 PEG ligands/nm^2, and 10.8ug/mL IL-4 was used in the subsequent conjugation reaction. The protein-to-AuNP stoichiometry was varied by increasing the AuNP-PEG concentration, up to 33x that previously allowed. Importantly, this allowed the stoichiometry associated with the theoretical maximum protein packing density, ~0.1 ligands/nm^2, as calculated based on sphere packing, to be achieved (Table 2.2).

Table 2.2. Theoretical maximum protein packing density calculated based on sphere packing



Interleukin	Molecular Weight [kDa]*	Radius [nm]#	Theoretical Loading [ligands/nm²]##
Human IL-4	15.1	1.63	0.12
Human IL-13	12.6	1.54	0.14
Human IL-10	18.6	1.75	0.11
Murine IL-4	13.5	1.57	0.13
Murine IL-10	18.7	1.75	0.11

*Peprotech
Calculated using equation in [32]
for a 30nm diameter AuNP core

As expected, decreasing the protein-to-AuNP stoichiometry increased IL-4 conjugation efficiency, and resulted in lower IL-4 ligand density (Fig. 2.9 C,D; Table 2.3). At the highest protein-to-AuNP ratios tested, the conjugated IL-4 ligand density was observed to be greater than the theoretical maximum, calculated based on sphere packing (Fig. 2.9 D). This may have been due to the formation of multiple layers of IL-4 associated with the surface of the particle. Based on these results, providing 0.5 protein ligands/nm^2 in the conjugation reaction, should yield conjugation that nearly achieves the theoretical maximum protein loading, indicated by the red line in Fig. 2.9 C,D. As expected, these low protein:PEG ratio particles were stable, as indicated by small hydrodynamic diameters and low PDIs (Fig. 2.9 E; Fig. 2.11). These optimized parameters were found to be broadly applicable, and were used to synthesize monodisperse particles with human and murine IL-4 and IL-10 (Fig. 2.9 F,G; Fig. 2.12).

Table 2.3. Sequential PEGylation then IL conjugation

Au [nm^2/mL] in conjugation reaction	IL-4 [ligands/nm^2] provided	Conjugation efficiency (%)	IL-4 [ligands/nm^2] conjugated
1.6E+14	2.5	31	0.85
6.4E+14	0.61	35	0.23
1.3E+15	0.3	40	0.13
2.6E+15	0.15 (theoretical maximum)	45	0.075
5.2E+15	0.075	51	0.042

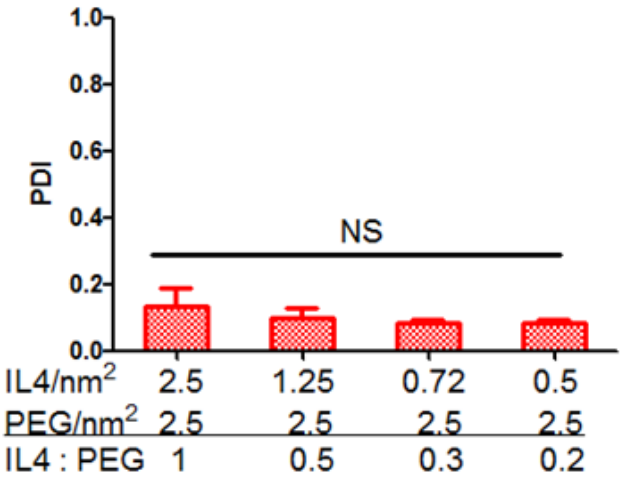


Figure 2.11. Polydispersity index (PDI) of PEG-AuNP-IL4 in MilliQ water resulting from decreasing the IL-4:PEG ratio < 1. Data are means ±SD, n=3. NS = not statistically significant

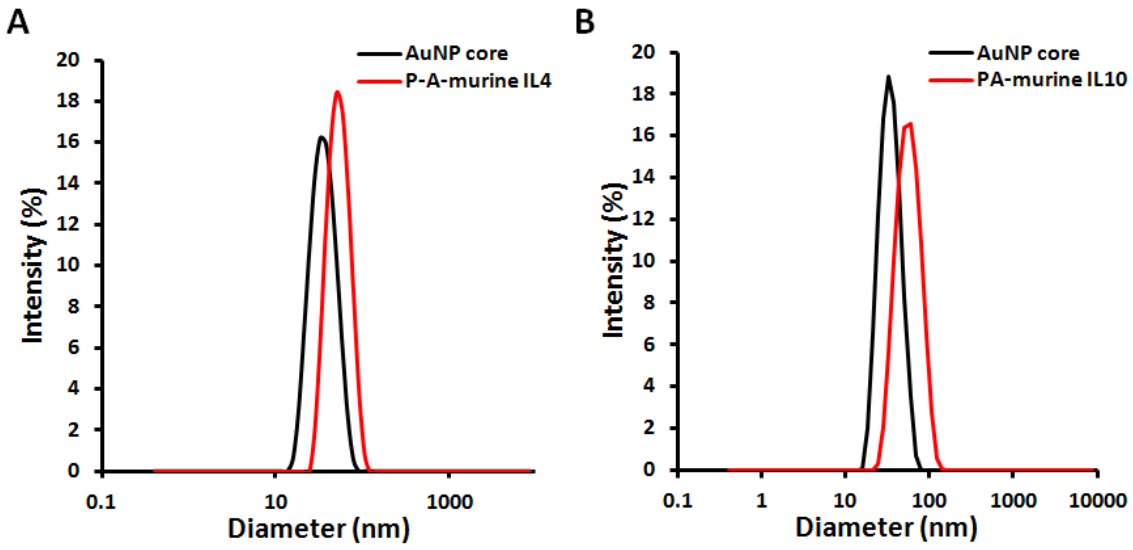


Figure 2.12. Sequential PEGylation then murine protein conjugation yields monodisperse murine IL-4 and IL-10 conjugated particles. (A,B) DLS size distribution following sequential partial PEGylation then murine IL-4 (A) or murine IL-10 (B) conjugation in MilliQ water.

Next it was important to ensure that the low protein:PEG ratio particles were able to direct macrophage polarization. As previously, matched doses of IL-4 delivered as soluble IL-4 or PEG-AuNP-IL4 were used to direct THP-1 derived human macrophage polarization in vitro (Fig. 2.13 A). As expected, neither AuNP-PEG (used as a negative control) nor PEG-AuNP-IL4 particles had a substantial effect on macrophage viability (Fig. 2.13 B). Importantly, these low protein:PEG ratio particles were not inflammatory, and were able to direct M2a (CD206+/CCR7-) macrophage polarization to the same extent as soluble IL-4 (Fig. 2.13 C).

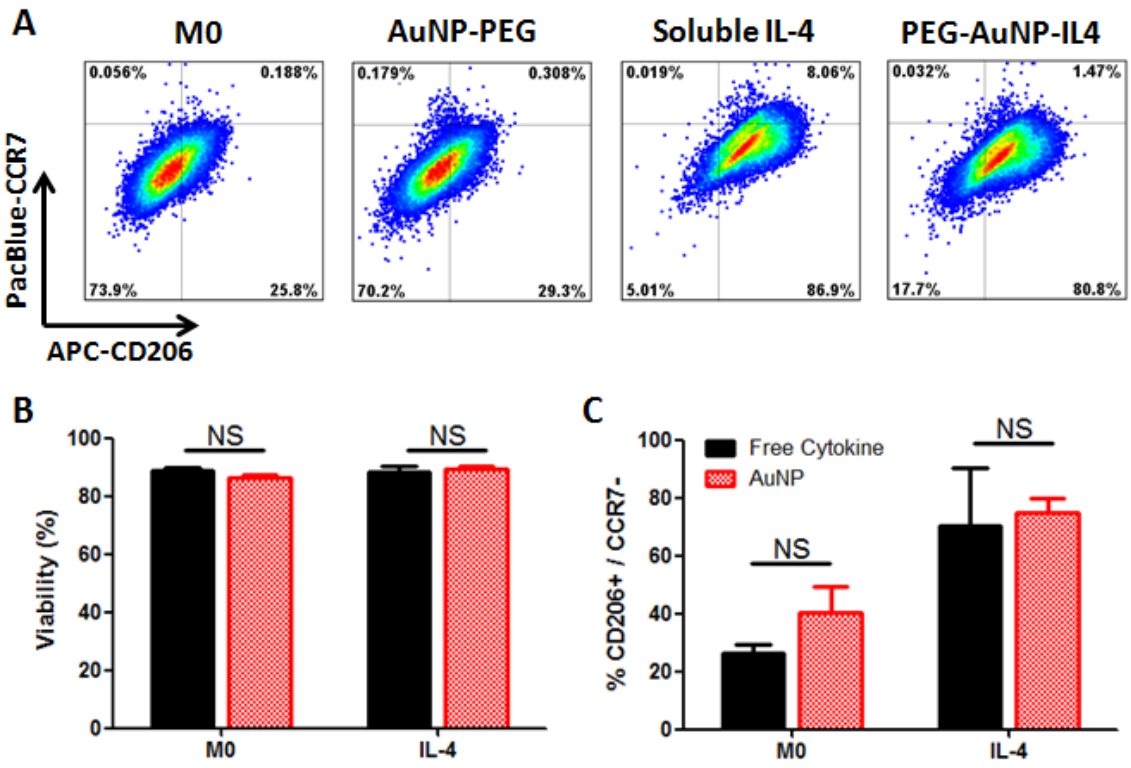


Figure 2.13. High PEG:IL-4 ratio PEG-AuNP-IL4 particles and AuNP-PEG-IL4 particles direct M2a macrophage polarization. (A) Representative FACS scatter plots showing expression of the inflammatory (CCR7) vs the M2a (CD206) polarization marker in response to 20ng/mL IL-4 delivered as soluble IL-4 or as the optimized high PEG:IL-4 ratio PEG-AuNP-IL4 particles, a comparable dose of AuNP-PEG or no cytokine stimulation (M0) were used as negative controls. (B) Macrophage viability assessed using a fixable dead cell stain (Invitrogen) and flow cytometry in response to no cytokine stimulation (M0, black), soluble IL-4 (IL-4, black), AuNP-PEG (M0, red), or high PEG:IL-4 ratio PEG-AuNP-IL4 (IL-4, red). (C) Percentage of macrophages expressing the M2a phenotype (CD206+/CCR7-). All data are means ±SD, n=3. *P<0.05, **P<0.01, ***P<0.001 NS = not statistically significant

2.3.6 PEG-AuNP-IL4 and PEG-AuNP-IL10 direct M1 macrophage polarization towards the M2 phenotype.

To further explore the ability of these nanoparticles to direct macrophage polarization in the context of chronic inflammation, they were used to treat inflammatory M1 macrophages in vitro. THP-1 derived macrophages were stimulated with LPS and IFN-γ for 2 days to promote the inflammatory M1 phenotype. M1 macrophages were then exposed to IL-4 as soluble IL-4 or PEG-AuNP-IL4, IL-10 as

soluble IL-10 or PEG-AuNP-IL10, or the combination of IL-4 + IL-10 delivered as soluble factors or PEGylated AuNPs. Basal media lacking cytokines was used as a negative control, and polarization was assessed with flow cytometry on day 5 (Fig. 2.14 A). As expected, following stimulation with soluble IL-4 and/or IL-10, M1 macrophage polarization shifted towards the M2 phenotype, and markers of M2 polarization (CD163 and CD206) were upregulated (Fig. 2.14 B,C). Importantly, nanoparticle delivery of IL-4 and IL-10 was just as potent as the soluble cytokines at promoting M2 polarization of an initially M1 macrophage population (Fig. 2.14 B,C), suggesting that nanoparticle delivery of macrophage polarizing cytokines may be useful in the context of an inflammatory microenvironment in vivo.

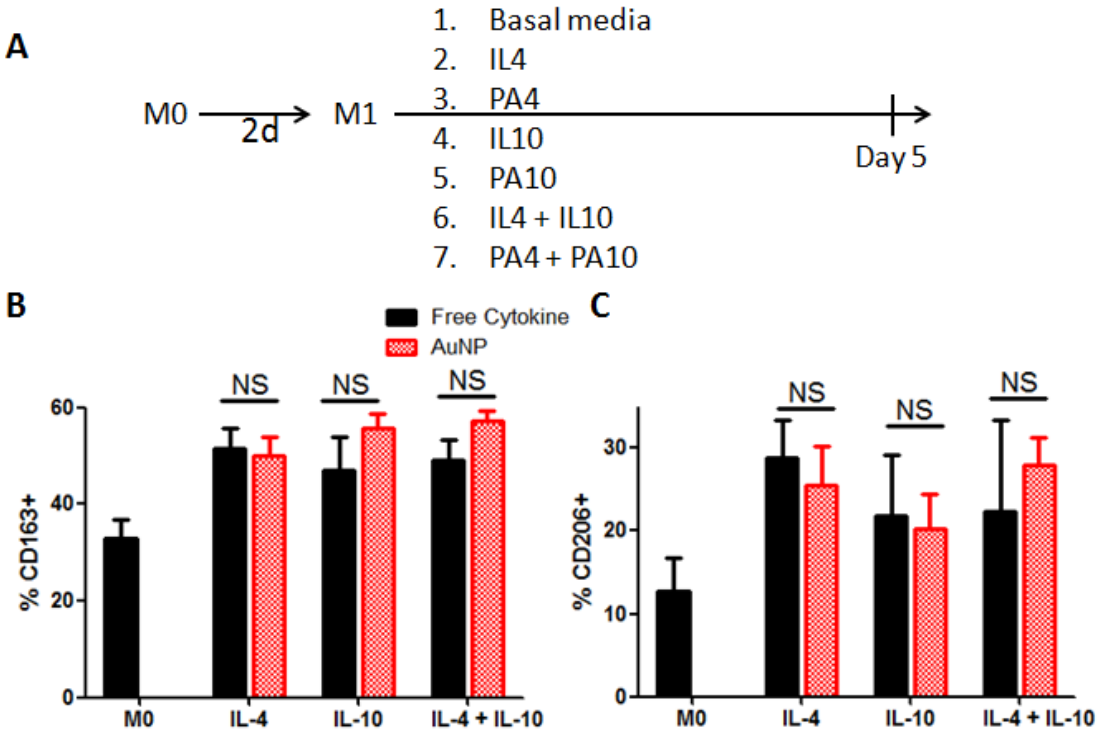


Figure 2.14. PEG-AuNP-IL4 and PEG-AuNP-IL10 are able to direct M1 macrophage polarization towards the M2 phenotype. (A) THP-1 monocytic cells were differentiated to M0 macrophages (3 days with 100ng/mL PMA) and then polarized towards the M1 phenotype (2 days with 2400ng/mL LPS, and 20ng/mL IFN-gamma). M1 macrophages were then exposed to IL-4 as soluble IL-4 or PA4, IL-10 as soluble IL-10 or PA10, or the combination of IL-4 + IL-10 delivered as soluble factors or PEGylated AuNPs. Basal media lacking cytokines was used as a negative control. (B,C) Percentage of macrophages expressing CD163 (a marker of M2c polarization) (B), or CD206 (a marker of M2a polarization). All data are means ±SD, n=3. NS = not statistically significant

2.4 Discussion

Macrophages have the capacity to both promote inflammation (M1 polarization) and stimulate tissue regeneration (M2 polarization); uncontrolled macrophage activation contributes to the progression of many diseases [33]. Therefore, the development of therapeutics to control macrophage polarization is of considerable interest. Here we show that M2 macrophage polarizing cytokines can be directly conjugated to AuNPs. Partial PEGylation stabilized the particles and allowed the subsequent conjugation of cytokines directly to the remaining Au surface, at ligand densities that approximated the theoretical maximum loading capacity. Importantly, PEGylation did not interfere with the bioactivity of conjugated cytokines; conjugated human IL-4, IL-13, and IL-10 all retained full bioactivity and were able to direct M2 macrophage polarization as efficiently as their soluble counterparts. Further, these nanoparticles were able to redirect the polarization of M1 macrophages towards the M2 phenotype, suggesting that they may be of use clinically for the treatment of inflammation.

These studies demonstrate that the M2 polarizing cytokines, IL-4, IL-13, and IL-10, can be directly conjugated to PEGylated AuNPs. The thiol-gold bond has been used extensively for the formation of monolayers on gold surfaces [30]. Here, disulfides capable of forming thiol-gold bonds available in IL-4, IL-13, and IL-10 were exploited, along with electrostatic interactions, to conjugate these cytokines to AuNP surfaces. Citrate stabilized AuNP cores were synthesized by the hydroquinone growth of AuNP seed particles [28], and as expected, 30nm AuNP cores had a ζ-potential around -33mV (Figs. 2.1 H; 2.2 A). Surface modifications to the AuNPs were easily tracked using ζ-potential and DLS size measurements, with increasing ζ-potential indicating replacement of citrate ions with conjugated ligands (either thiolated-PEG or protein) (Figs. 2.1 H, 2.2 A). Subtractive analysis following removal of unbound protein by centrifugation allowed the protein conjugation efficiency and ligand density to be calculated (Figs. 2.1 E,F; 2.6 G,H; 2.9 C,D) and by controlling the stoichiometric ratio of protein and AuNPs provided in the reaction, the conjugation efficiency and protein ligand density could be controlled. PEGylation of nanoparticle surfaces has been used previously to increase particle stability, decrease

protein adsorption and alter rates of macrophage internalization [29]. In this study, partial PEGylation of AuNPs was used to increase particle stability. Providing 2.5 PEG and 0.5 IL-4 ligands/nm^2 minimized particle aggregation while achieving protein conjugation that approximated the theoretical maximum, as calculated by sphere packing (Fig. 2.9 C,D). Further, these parameters applied broadly to M2 polarizing cytokines, and resulted in monodisperse PEG-AuNP particles with conjugated human and murine IL-4 and IL-10 (Figs. 2.9 F,G; 2.12). AuNPs have been widely investigated for their use in drug delivery as they provide a relatively biologically inert substrate, may increase retention time in the tissue of interest, and allow easy conjugation chemistry [34, 35, 36]. PEGylated AuNPs with conjugated TNF-α have been developed for the treatment of solid tumors [37]. These particles were able to avoid uptake by the reticuloendothelial system (RES), preferentially distribute to solid tumors, and promote tumor regression in preclinical models [38]; further, a phase I clinical trial has recently shown good tolerance [27]. The nanoparticles designed in this work build on these concepts to expand the application of AuNPs as a drug delivery vector in the context of chronic inflammation. Rather than promoting inflammation and tumor cell killing, the particles designed here seek to promote the resolution of inflammation and promote tissue regeneration. Formulations of gold salts have been used for over 3 decades for the treatment of rheumatoid arthritis [39, 40] because of their ability to improve inflammation. While the mechanism of these treatments is still poorly understood, their therapeutic utility in that context suggests that gold may provide particular advantages as a drug delivery platform for the treatment of chronic inflammation. Importantly, the principles developed in the current study, begin to establish a general method for the use of AuNPs for the delivery of anti-inflammatory cytokines.

AuNP conjugated IL-4, IL-13, and IL-10 are bioactive and direct macrophage polarization towards the M2 phenotype. Following conjugation to AuNPs all three M2 macrophage polarizing cytokines tested retained full bioactivity and were able to direct the same level of M2 polarization as an equivalent dose of their soluble counterparts (Fig. 2.4). Importantly, partial PEGylation of AuNPs did not interfere with cytokine bioactivity (Figs. 2.8, 2.13), and PEG-AuNP-IL4 and PEG-AuNP-IL10 were able

to repolarize M1 macrophages towards the M2 phenotype (Fig. 2.14). The ability to shift inflammatory macrophage polarization away from the M1 state and promote pro-regenerative M2 states will likely be important for the treatment of many non-healing wounds, and chronic inflammatory conditions. While it has been shown that primary human macrophages can shift their polarization from M1 to M2, and vice versa, in response to cytokine stimulation [41], the development of biomaterial therapies capable of promoting this shift is still ongoing. Recently large pore mesoporous silica NPs have been developed for the delivery of IL-4 [42]. Following intravenous injection, the particles were internalized by phagocytic myeloid cells and promoted M2 polarization in the spleen. The use of these particles to redirect M1 macrophage polarization in vitro or in vivo, in the context of inflammation, or in the targeting of tissues other than the spleen, has not been explored. Other biomaterial designs aimed at directing M1 followed by M2 polarization have focused on the use of scaffolds, such as decellularized bone [43], or biomimetic coatings, such as calcium phosphate [44], to sequentially deliver inflammatory and pro-regenerative stimuli to promote M1 followed by M2 polarization. While the use of biomimetic coatings to direct macrophage polarization switching has successfully demonstrated the ability to switch gene expression in human and murine macrophages in vitro [44], difficulty properly controlling the release kinetics from decellularized scaffolds in vivo has limited their success [43]. While promising, these designs are specific to directing macrophage polarization in bone, and will likely require the development of new chemistries to deliver a broad array of anti-inflammatory cytokines. The AuNP design presented here has been shown to preserve the bioactivity of IL-4, IL-13 and IL-10 and could likely be applied to any cytokine with disulfide or thiol groups available to participate in thiol-gold bonds, or an isoelectric point that would support electrostatic binding to AuNPs. Further, PEGylated AuNPs may find utility in the treatment of a broad range of inflamed tissues to redirect M1 polarization towards the M2 state.

The results of these studies indicate that AuNPs can be used to direct macrophage polarization towards M2 phenotypes in vitro. The use of PEGylation to stabilize AuNPs, and thiol-Au bonds to form mixed monolayers of PEG:cytokine, builds on well established research and expands the capabilities of

AuNPs as a drug delivery vector in the context of chronic inflammation. With the increasing realization that macrophages play an essential role in orchestrating both inflammation and tissue regeneration, and that M2 macrophage polarization can promote tissue healing, the ability to direct M2 polarization with cytokine conjugated AuNPs may find clinical utility in the treatment of non-healing wounds and chronic inflammatory conditions.

2.5 References

[1] D. M. Mosser and J. P. Edwards, "Exploring the full spectrum of macrophage activation," *Nature Reviews,* vol. 8, no. 12, pp. 958-969, 2008.

[2] A. Mantovani et al., "The chemokine system in diverse forms of macrophage activation and polarization," *TRENDS in Immunology,* vol. 25, no. 12, pp. 677-686, 2004.

[3] R. Mirza and T. Koh, "Dysregulation of monocyte/macrophage phenotype in wounds of diabetic mice," *Cytokine,* vol. 56, no. 2, pp. 256-264, 2011.

[4] K. Kigerl et al., "Identification of two distinct macrophage subsets with divergent effects causing either neurotoxicity or regeneration in the injured mouse spinal cord," *J Neurosci,* vol. 29, no. 43, pp. 13435-13444, 2009.

[5] J. Tonkin et al., "Monocyte/Macrophage-derived IGF-1 Orchestrates Murine Skeletal Muscle Regeneration and Modulates Autocrine Polarization," *Molecular Therapy,* vol. 23, no. 7, pp. 1189-1200, 2015.

[6] D. Ruffell et al., "A CREB-C/EBP-beta cascade induces M2 macrophage-specific gene expression and promotes muscle injury repair," *Proc Natl Acad Sci,* vol. 106, no. 41, pp. 17475–17480, 2009.

[7] A. Chawla, K. Nguyen and Y. Goh, "Macrophage-mediated inflammation in metabolic disease," *Nat Rev Immunol,* vol. 11, no. 11, pp. 738-749, 2011.

[8] N. Fahy et al., "Human osteoarthritic synovium impacts chondrogenic differentiation of mesenchymal stem cells via macrophage polarisation state," *HumaOsteoarthritis and Cartilage,* vol. 22, no. 8, pp. 1167-1175, 2014.

[9] R. W. Kinne, B. Stuhlmuller, G. Burmester, "Cells of the synovium in rheumatoid arthritis. Macrophages.," *Arthritis Res Ther,* vol. 9, no. 6, pp. 224-239, 2007.

[10] S. Villalta, B. Deng, C. Rinaldi, M. Wehling-Henricks and J. Tidball, "IFN-γ Promotes Muscle Damage in the mdx Mouse Model of Duchenne Muscular Dystrophy by Suppressing M2

Macrophage Activation and Inhibiting Muscle Cell Proliferation," *J Immunology,* vol. 187, no. 10, pp. 5419-5428, 2011.

[11] K. Spiller and T. Koh, "Macrophage-based therapeutic strategies in regenerative medicine," *Advanced Drug Delivery Reviews,* vol. 122, pp. 74–83, 2017.

[12] P. Graney, E. Lurier and K. Spiller, "Biomaterials and Bioactive Factor Delivery Systems for the Control of Macrophage Activation in Regenerative Medicine," *ACS Biomater. Sci. Eng,* vol. 4, no. 4, pp. 1137-1148, 2018.

[13] T. Smith, R. Nagalla, E. Chen and W. Liu, "Harnessing macrophage plasticity for tissue regeneration," *Advanced Drug Delivery Reviews,* vol. 114, pp. 193-205, 2017.

[14] M. Racke, A. Bonomo, D. Scott, B. Cannella, A. Levine, C. Raine, E. Shevach and M. Rocken, "Cytokine-induced immune deviation as a therapy for inflammatory autoimmune disease," *J Exp Med,* vol. 180, no. 5, pp. 1961-1966, 1994.

[15] A. Horsfall, D. Butler, L. Marinova, P. Warden, R. Williams, R. Maini and M. Feldmann, "Suppression of collagen-induced arthritis by continuous administration of IL-4," *J Immunol,* vol. 159, no. 11, pp. 5687-5696, 1997.

[16] K. Ghoreschi et al., "Interleukin-4 therapy of psoriasis induces Th2 responses and improves human autoimmune disease," *Nature Medicine,* vol. 9, no. 1, pp. 40-46, 2003.

[17] Z. Zidek, P. Anzenbacher and E. Kmonickova, "Current status and challenges of cytokine pharmacology," *Br J Pharmacol,* vol. 157, no. 3, pp. 342–361, 2009.

[18] P. Rutgeerts, G. Van Assche and S. Vermeire, "Optimizing anti-TNF treatment in inflammatory bowel disease," *Gastroenterology,* vol. 126, pp. 1593−1610, 2004.

[19] X. Miao, X. Leng and Q. Zhang, "The Current State of Nanoparticle-Induced Macrophage Polarization and Reprogramming Research," *Int. J. Mol. Sci.,* vol. 18, no. 2, pp. 336-348, 2017.

[20] S. Lee et al., "TNF-α gene silencing using polymerized siRNA/thiolated glycol chitosan nanoparticles for rheumatoid arthritis," *Mol. Ther.,* vol. 22, pp. 397-408, 2014.

[21] M. Kim et al., "Notch1 targeting siRNA delivery nanoparticles for rheumatoid arthritis therapy," *J. Controlled Release,* vol. 216, pp. 140-148, 2015.

[22] S. Jain, T. Tran and M. Amiji, "Macrophage repolarization with targeted alginate nanoparticles containing IL-10 plasmid DNA for the treatment of experimental arthritis," *Biomaterials,* vol. 61, pp. 162-177, 2015.

[23] J. Zhang, C. Tang and C. Yin, "Galactosylated trimethyl chitosan−cysteine nanoparticles loaded with Map4k4 siRNA for targeting activated macrophages," *Biomaterials,* vol. 34, pp. 3667-3677, 2013.

[24] T.H. Tran, R. Rastogi, J. Shelke and M. Amiji, "Modulation of Macrophage Functional Polarity towards Anti-Inflammatory Phenotype with Plasmid DNA Delivery in CD44 Targeting Hyaluronic Acid Nanoparticles," *Scientic Reports,* vol. 5, pp. 16632-46, 2015.

[25] S. Rana, A. Bajaj, R. Mout and V. Rotello, "Monolayer coated gold nanoparticles for delivery applications," *Advanced Drug Delivery Reviews,* vol. 64, pp. 200-216, 2012.

[26] R. Visaria et al., "Enhancement of tumor thermal therapy using gold nanoparticle-assisted tumor necrosis factor-alpha delivery," *Mol. Cancer Ther.,* vol. 5, pp. 1014-1020, 2006.

[27] S. Libutti et al, "Results of a completed phase I clinical trial of CYT-6091: A pegylated colloidal gold-TNF nanomedicine," *J Clinical Oncology,* vol. 27, no. 15S, pp. 3586-3586, 2009.

[28] S. D. Perrault and W. C. Chan, "Synthesis and Surface Modification of Highly Monodispersed, Spherical Gold Nanoparticles of 50-200 nm," *JACS,* vol. 131, no. 47, pp. 17042-17073, 2009.

[29] C. D. Walkey, J. B. Olsen, H. Guo, A. Emili and W. C. Chan, "Nanoparticle Size and Surface Chemistry Determine Serum Protein Adsorption and Macrophage Uptake," *JACS,* vol. 134, no. 4, pp. 2139-2147, 2012.

[30] M. Hasan, D. Bethell and M. Brust, "The Fate of Sulfur-Bound Hydrogen on Formation of Self-Assembled Thiol Monolayers on Gold: 1H NMR Spectroscopic Evidence from Solutions of Gold Clusters," *JACS.,* vol. 124, no. 7, pp. 1132-1133, 2002.

[31] P. Hornbeck et al., "PhosphoSitePlus, 2014: mutations, PTMs and recalibrations," *Nucleic Acids Res,* vol. 43, pp. D512-20, 2015.

[32] H. Erickson, "Size and Shape of Protein Molecules at the Nanometer Level Determined by Sedimentation, Gel Filtration, and Electron Microscopy," *Biological Procedures Online,* vol. 11, no. 1, pp. 32-51, 2009.

[33] P. Murray and T. Wynn, "Protective and pathogenic functions of macrophage subsets," *Nature Reviews,* vol. 11, no. 11, pp. 723-737, 2011.

[34] B. Merchant, "Gold, the noble metal and the paradoxes of its toxicology," *Biologicals,* vol. 26, no. 1, pp. 49-59, 1998.

[35] J. Caster, A. Patel, T. Zhang and A. Wang, "Investigational nanomedicines in 2016: a review of nanotherapeutics currently undergoing clinical trials," *WIREs Nanomed Nanobiotechnol,* vol. 9, no. 1, p. e1416, 2017.

[36] L. Yang and Y. Zhang, "Tumor-associated macrophages: from basic research to clinical application," *J Hematology & Oncology,* vol. 10, pp. 58-69, 2017.

[37] G. Paciotti et al., "Colloidal Gold: A Novel Nanoparticle Vector for Tumor Directed Drug Delivery,"

Drug Delivery, vol. 11, pp. 169-183, 2004.

[38] G. Paciotti, D. Kingston and L. Tamarkin, "Colloidal Gold Nanoparticles: A Novel Nanoparticle Platform for Developing Multifunctional Tumor-Targeted Drug Delivery Vectors," *Drug Development Research,* vol. 67, pp. 47-54, 2006.

[39] J. Ward et al., "Comparison of auranofin, gold sodium thiomalate, and placebo in the treatment of rheumatoid arthritis," *Arthritis & Rheumatology,* vol. 26, no. 11, pp. 1303-1315, 1983.

[40] G. Bendix and A. Bjelle, "A 10 year follow up of parenteral gold therapy in patients with rheumatoid arthritis," *Ann Rheum Dis,* vol. 55, no. 3, pp. 169-176, 1996.

[41] A. Gratchev et al., "M1 and M2 can be re-polarized by Th2 or Th1 cytokines, respectively, and respond to exogenous daanger signals," *Immunobiology,* vol. 211, pp. 473-486, 2006.

[42] D. Kwon et al., "Extra-Large Pore Mesoporous Silica Nanoparticles for Directing in Vivo M2 Macrophage Polarization by Delivering IL-4," *Nano Letters,* vol. 17, no. 5, pp. 2747−2756, 2017.

[43] K. Spiller et al., "Sequential delivery of immunomodulatory cytokines to facilitates the M1-to-M2 transition of macrophages and enhance vascularization of bone scaffolds," *Biomaterials,* vol. 37, pp. 194-207, 2015.

[44] J. Alhamdi et al., "Controlled M1-to-M2 transition of aged macrophages by calcium phosphate coatings," *Biomaterials,* 2018, https://doi.org/10.1016/j.biomaterials.2018.07.012.

[45] I. Somasuntharam et al., "Knockdown of TNF-alpha by DNAzyme gold nanoparticles as an antiinflammatory therapy for myocardial infarction," *Biomaterials,* vol. 83, pp. 12-22, 2016.

CHAPTER 3:

Functional Muscle Recovery with Nanoparticle-Directed M2 Macrophage Polarization in Mice

3.1 Introduction

Acute inflammation is a protective response that kills invading pathogens, should be self limiting and lead to healing. However, uncontrolled activation of immune cells, and failure of the acute inflammatory response to be self limiting leads to chronic inflammation resulting in tissue damage [1]. Following tissue injury or infection, monocytes (Mc) are recruited from circulation and differentiate to M1 macrophages (Mφs) which promote inflammation by the release of inflammatory cytokines, reactive oxygen species, proteases, and antimicrobial peptides [2]. Subsequently, Mφs adopt potent anti-inflammatory and pro-regenerative activity, broadly referred to as M2 Mφs. Beyond antagonizing M1 responses, M1 to M2 phenotype switching is important in promoting tissue regeneration and restoring homeostasis [2-4]. M1-Mφ dominated aberrant inflammation contributes to the pathogenesis of many chronic inflammatory conditions including atherosclerosis, inflammatory bowel disease, asthma, rheumatoid arthritis, osteoarthritis, multiple sclerosis, and chronic venous leg ulcers [5-10]. Hence, development of therapeutics that can dampen acute inflammation and promote M2 polarization are of considerable interest.

Mφ polarization plays a central role in directing skeletal muscle regeneration following injury [11-12]. Satellite cells, muscle resident stem cells, become activated to proliferate, migrate to the injury, fuse, and differentiate to form new myofibers [13-14]. Mφs directly control satellite cell activation and maturation and are crucial to muscle regeneration [15-16]. M1 Mφs promote the proliferation of satellite and myogenic precursor cells, in vitro and in vivo, following human muscle injury, while M2 Mφs promote their differentiation [15]. Imbalanced Mφ polarization, specifically skewing towards M1 phenotypes, has been shown to inhibit skeletal muscle repair [3,16-17]. Transition to M2 phenotypes is critical to ultimately yield functional muscle [18].

The hypothesis underlying this study is that IL-4 conjugated gold nanoparticles (AuNPs) can direct M2a Mφ polarization, thereby enhancing regeneration of functional skeletal muscle following ischemic injury. IL-4 is an anti-inflammatory cytokine that can induce the polarization of M1 Mφs towards the M2a state. Exogenous IL-4 is sufficient to drive accumulation of M2 Mφs through self-renewal, suggesting that IL-4 delivery can induce the expansion of therapeutic M2 Mφs without necessitating further recruitment of destructive M1 Mφs [19]. IL-4 has been widely explored as a potential therapeutic in various inflammatory disease models including autoimmune demyelinating disease, arthritis and chronic skin inflammation [20-22]. However its use has required repeated infusions due to its short half-life in vivo. Resultant high dose requirements and systemic side effects have limited the use of IL-4 treatments [23]. Here we utilize nanoparticles (NPs) for IL-4 delivery, as they allow distribution throughout the targeted tissue and can extend retention time as compared to bolus delivery. AuNPs were specifically used because they can be synthesized with monodisperse size over a clinically relevant range [24], can be injected and show minimal toxic or immunogenic activity in humans [25-26]. Formulations of gold (Au) are FDA approved for the treatment of arthritis, a chronic inflammatory condition [27].

3.2 Materials and Methods

3.2.1 Surgery

Animal work was in compliance with NIH and institutional guidelines. Hindlimb ischemia was induced in female C57BL/6J mice (6-8wks; Jackson Laboratories) by left unilateral femoral artery and vein ligation [40]. On day 3, ischemic tibialis anterior (TA) muscles were injected with 2ug IL-4 as PEG-AuNP-IL4 (PA4) or soluble IL-4, AuNP-PEG or PBS; 2,10uL injections were given to each TA.

3.2.2 Macrophage Depletion

Clodronate and PBS liposomes were purchased from Liposoma (SKU: LIP-01). Liposomes (70uL) were administered retro-orbitally 2 days before surgery, and again on days 1 and 5 after surgery

(Appendix B, Fig. B1 A); 10uL were also administered intramuscularly into the ischemic TA 1 day before surgery, and again on days 2 and 7 after surgery.

3.2.3 Blood Perfusion

Measurements of blood perfusion were performed using a Laser Doppler Perfusion Imaging (LDPI) analyzer (PeriScan PIM II; Perimed) on anesthetized mice.

3.2.4 Muscle Force Measurements

All animal work was performed in compliance with NIH and institutional guidelines. Intact TA muscles were dissected, and immediately mounted vertically midway between two cylindrical parallel steel wire electrodes (1.6 mm diameter, 21 mm long) by attaching their tendons to microclips connected to a force transducer (FORT 25, WPII) [45]. Muscles were bathed in physiologic saline solution in a chamber with continuously bubbled oxygen at 37^{o}C, and the muscle was adjusted to a physiologically relevant length. A wave pulse was initiated using a custom-written LabVIEW program and delivered to the stimulation electrodes via a purpose built power amplifier (QSC USA 1310). Three tetanic contractions were evoked at 250, 270, 300 Hz and 25, 27, 30 V, respectively, with a constant pulse width of 2ms and a train duration of 1s. The muscle was allowed to rest for 5min between each stimulation. Contraction force was determined as the difference between the maximum force during contraction and the baseline level (Appendix B, Fig. B2). Following ex vivo stimulation muscles were weighed and forces were then normalized to muscle wet weight. Contraction velocity was determined as the slope of the force curve at the time electrical stimulation was initiated (Appendix B, Fig. B2).

3.2.5 AuNP Synthesis

AuNPs were synthesized by the hydroquinone reduction of gold onto citrate stabilized seed particles [24]. Briefly, to make 15nm seed particles, 1mL of 1%w/v gold chloride (Sigma #254169) solution was added to 100mL of MilliQ water in a clean Erlenmeyer flask, stirred slowly and heated on a

400°C plate. As soon as the solution came to a boil, the stirring was set as fast as possible without splashing, and 3mL of 1% w/v sodium citrate (Sigma # 4641) was rapidly added. The solution color changed from clear to purple to red over the course of ~5min, a few minutes after the color changes completed, the solution was cooled at room temperature.

The 30, 60, and 100nm-core AuNPs were then synthesized by the reduction of ionic gold onto the 15nm seed particles by hydroquinone. MilliQ water was added to an Erlenmeyer flask followed by 25mM gold chloride solution, and 15nm seed particles. The solution was spun as fast as possible without splashing and then 15mM sodium citrate and 25mM hydroquinone were added simultaneously. The volume of each solution added to the hydroquinone reduction reaction depended on the desired nanoparticle size, and have been published previously [47]. The solution color changed from red to black and then to a darker red. The reaction was completed in a few minutes; then particles were stored at room temperature.

3.2.6 PEGylation and IL-4 conjugation to the AuNPs

AuNPs were sterilized by filtration through a 0.2μm filter. Then they were divided into 1mL aliquots in Eppendorf tubes and pelleted via centrifugation; an aliquot was resuspended at 1x concentration in MilliQ water and the dynamic light scattering (DLS) size and absorbance were measured. The size and absorbance were used to calculate the AuNP concentration using the Beer-Lambert Law. The remaining AuNPs were then resuspended in MilliQ water containing 5kDa methoxy PEG-SH (Laysan Bio, Inc) to a final concentration 15x more concentrated than the AuNP synthesis solution; 2.5 PEG ligands/nm^2 were provided, only enough to partially cover the AuNP core. PEGylation was allowed to occur overnight at room temperature, on a slow shaker.

Following overnight PEGylation, recombinant human or murine IL-4 (Peprotech) was added to the reaction along with trehalose (Sigma #T0167). Enough IL-4 was added to provide 0.5 ligands/nm^2, and the final concentration of trehalose was 10% w/v. IL-4 conjugation was allowed to occur overnight at

room temperature, on a slow shaker. The unbound IL-4 and trehalose were removed by centrifugation, four washes in total. The supernatants were collected and the unbound IL-4 in the supernatants was quantified with LavaPep (Gel Company #LP-022010); subtractive analysis was used to quantify the bound IL-4. Following PEGylation and IL-4 conjugation, PA4s were resuspended in MilliQ water and the DLS size and zeta-potential were measured.

3.2.7 In vitro IL-4 release

PA4s were incubated in 1% BSA in PBS, or RPMI-1640 media (10% heat inactivated (HI)-FBS, 1% penicillin-streptomycin, HEPES, sodium bicarbonate, sodium pyruvate) at 37^{o}C, 5% CO_2. Supernatants were collected and released IL-4 was quantified with ELISAs. After 1 day, size distribution was measured by DLS (Zsizer, Marvern Instruments).

3.2.8 In vitro PA4 bioactivity assay with human THP-1 cells

THP-1 cells (ATCC® TIB-202^{TM}) were cultured in RPMI-1640 media (containing 10% HI-FBS) as recommended by ATCC, except 2-mercaptoethanol was excluded. To differentiate the THP-1 monocytes to macrophages, cells were seeded at 10^6cells/well in non-TC treated 6-well plates with 2mL media/well containing 100ng/mL phorbol 12-myristate 13-acetate (PMA). After 3 days, the PMA-media was removed and the following conditions were used to polarize the macrophages: 20ng/mL soluble IL-4 or 20ng/mL IL-4 delivered as PA4 for M2a polarization, complete RPMI media without additives or AuNP-PEG (dose matched to the AuNP dose in the PA4 condition) for M0 polarization. Polarization media was changed daily.

3.2.9 In vitro THP-1 macrophage polarization switching

After PMA differentiation, the following M1 polarization media was used: 20ng/mL IFN-γ + 2400ng/mL LPS for 2 days. After M1 polarization, the media was replaced with media containing 40ng/mL soluble IL-4, 40ng/mL IL-10, 40ng/mL IL-4 + 40ng/mL IL-10, or RPMI media without

additives. Flow cytometry was used to assess polarization after the 2 day M1 polarization, and at various timepoints after exposure to IL-4 and/or IL-10. Media was changed daily.

3.2.10 In vitro macrophage polarization in response to varying degrees of IL-4 valency on PA4

Following PEGylation of 30nm-core AuNPs as described above, varying amounts of IL-4 were added to the conjugation reaction to give 1x, 0.5x, 0.1x or 0.01x the amount of IL-4 typically provided per Au surface area, as described above in "3.2.6 PEGylation and IL-4 conjugation to the AuNPs." Conjugation of IL-4 to the AuNP was again quantified by subtractive analysis using LavaPep, also as described above.

After PMA differentiation of THP-1 cells, they were polarized with 20ng/mL IL-4 presented as soluble IL-4 or as the 1x, 0.5x, 0.1x or 0.01x PA4s described above. Basal medial lacking any IL-4 was used as a negative control. Polarization media was changed daily, for 3 days, then macrophage polarization was assessed using flow cytometry.

3.2.11 Histological Assessment of Skeletal Muscle

Following ex vivo muscle force measurements, the TA muscles were fixed in 4% PFA, washed, paraffin embedded and stained with H&E. H&E stained cross sections were imaged with a 10x lens on an Olympus-IX81 light microscope connected to a Olympus DP70 digital image capture system, and images were tiled across the entire muscle cross section. To assess the percentage of the muscle cross sectional area that was composed of muscle fibers and the percentage that consisted of cell nuclei, color deconvolution was performed with ImageJ. A threashold was then applied to the pink (eosin) color channel such that only muscle fibers were included in the threashold and background was excluded. The "analyze particles" function in ImageJ was then used to quantify the area within the threashold. To assess the nuclear area, the blue (hematoxylin) channel was processed by first increasing the contrast, then applying a threashold to include nuclei and exclude background. The threasholded image was then made binary, and finally the "watershed" function in ImageJ was used to separate distinct cell nuclei. Again the

"analyze particles" function was used to quantify the area within the blue (hematoxylin) threashold. The total cross sectional area of the muscle was measured in ImageJ by using freehand selection and the percentage of that cross section falling within the eosin and hematoxylin channels was calculated. The empty area was calculated by subtracting the muscle fiber area and the nuclear area from the total muscle cross sectional area. The investigator was blinded to treatment before performing the ImageJ analysis.

3.2.12 Statistics

All analyses were performed on GraphPad Prism5. For experiments that involved more than one comparison, ANOVA with Tukey or Bonferroni post hoc test was used. Where noted, Dunnett's comparison vs a control condition was used. For assessment of muscle function, a power analysis was performed on G*Power3.1 [46]. PA4 and PBS groups were performed with n=16 (per the analysis) and Bonferroni planned comparison was used.

3.3 Results

3.3.1 Mφs are required for regeneration of muscle function following ischemic injury.

We first explored the impact of Mc/Mφ depletion on spontaneous recovery from severe muscle damage. Ischemic injury of the left tibialis anterior (TA) muscle of C57BL6/J mice was induced by femoral artery/vein ligation. To deplete Mc/Mφs, mice were treated starting 2 days prior to surgery with clodronate or PBS liposomes (Liposoma) as a control (Fig. 3.1 A; Appendix B, Fig. B1 A). Clodronate treatment significantly reduced CD45+ immune cell recruitment to the ischemic TA (Fig. 3.1 B); due primarily to the depletion of myeloid cells (Fig. 3.1 C). Flow cytometry showed a significant reduction in the percentage and absolute number of Mφs, Mc, and Mc/Mφs in the ischemic TAs in following clodronate treatment, as expected (Fig. 3.1 D-F; Appendix B, Fig. B1 B-D).

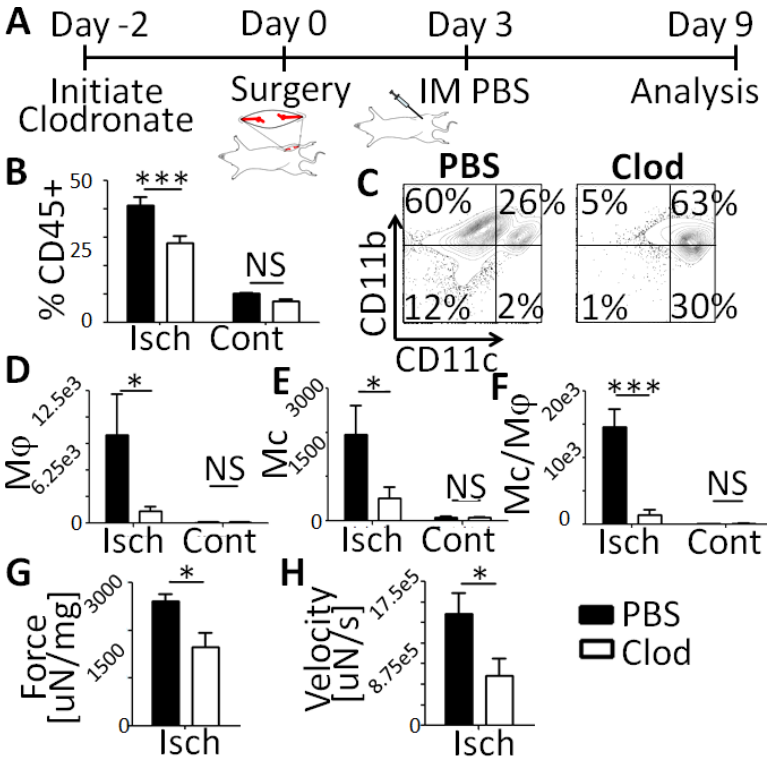


Figure 3.1. Mc/Mφs are required for regeneration of muscle function following ischemic injury. (A) Timeline showing clodronate treatment, injury and injection to the ischemic TA (B) Quantification of CD45+ cells in the TA, day 9, flow cytometry data. (C) Gating of CD45+ cells. (D-F) Number of Mφs (CD11c-/CD11b+/Ly6G-/Ly6C-/F4/80+) (D), Mc (CD11c-/CD11b+/Ly6G-/Ly6C+/F4/80-) (E), and Mc/Mφs (CD11c-/CD11b+/Ly6G-/Ly6C+/F4/80+) (F) in the TA. (G-H) Maximum TA contraction force and velocity of 3 tests. Force was normalized to TA mass. Data are means±SEM, n=7 *P<0.05, ***P<0.001

To determine if depletion of Mc/Mφs inhibited recovery of TA function, TAs were stimulated ex vivo (Appendix B, Fig. B2). A significant reduction in TA mass was observed on day 9 in mice treated with clodronate (Appendix B, Fig. B1 E). Although the overall weight of the mice was not affected, normalized TA mass was also significantly reduced with clodronate treatment (Appendix B, Fig. B1 F,G). Ultimately, clodronate depletion of Mc/Mφs resulted in significantly reduced TA contraction force and velocity following ischemic injury (Fig. 3.1 G-H).

3.3.2 Generation of NPs presenting the Mφ polarizing cytokine IL-4

We next designed PEG stabilized NPs presenting IL-4 (Fig. 3.2) to determine if promoting M2 polarization in damaged muscle could enhance recovery. First, it was demonstrated that soluble IL-4 shifts M1 Mφs to the M2 state in vitro (Fig. 3.3). AuNPs were then synthesized by hydroquinone reduction of Au onto citrate stabilized seed particles [24], and stabilized by partial PEGylation with 5kDa PEG-SH (Fig. 3.2 A). Subsequently, human or murine IL-4 was conjugated to the remaining Au surface (Fig. 3.2 B). IL-4 conjugation likely occurred via thiol-Au bonds and electrostatic interactions. Dynamic light scattering (DLS) showed that AuNPs were monodisperse around 30, 60 and 100nm diameters; a slight right-shift in size distribution following partial PEGylation, and a second right-shift following human and murine IL-4 conjugation (Fig. 3.2 C-E; Fig. 3.4). ζ -potential was used to track surface modification of the AuNPs. Following synthesis, 30-100nm AuNP cores had ζ-potentials from -44 to -38mV (measured in MilliQ water), following PEGylation and human IL-4 conjugation, the ζ-potentials became increasingly less negative, ranging from -10 to -15mV for the 30-100nm AuNP cores, and -1.67mV with murine IL-4 (Table 3.1). IL-4 loading onto AuNPs was calculated based on subtractive analysis and compared to the theoretical maximum capacity. The theoretical maximum was calculated based on sphere packing (Appendix B, Fig. B3). IL-4 conjugation efficiency was fairly consistent for human and murine IL-4, and showed no statically significant differences across the 30-100nm AuNP cores, representing ~40-60% of the theoretical maximum (Table 3.2). As the AuNPs were partially PEGylated, IL-4 conjugation efficiencies ~50% were expected.

Table 3.1. AuNP size and ζ-potential

	Z-average [nm]	PDI	ζ Potential [mV]
100nm AuNP	98.7	0.062	-38.7
100nm AuNP-PEG	115.5	0.063	-27.8
100nm PA4	130.6	0.082	-15.5
60nm AuNP	61.4	0.130	-37.9
60nm AuNP-PEG	76.3	0.113	-29.6
60nm PA4	85.7	0.133	-15.7
30nm AuNP	34.3	0.122	-44.1
30nm AuNP-PEG	47.7	0.098	-24.0
30nm PA4	50.3	0.112	-10.5
30nm murine PA4	50.3	0.092	-1.67

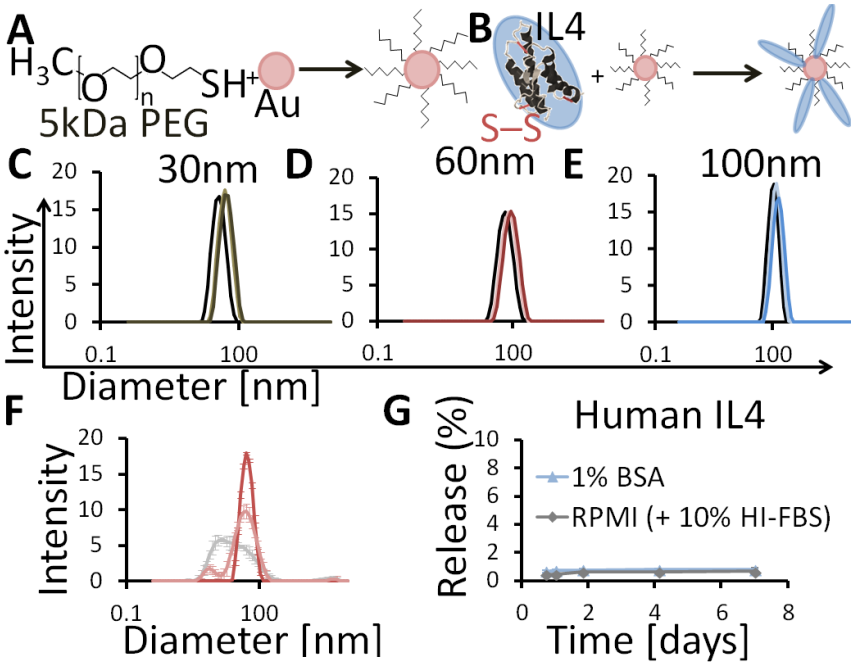


Figure 3.2. AuNP Synthesis and human IL-4 conjugation. (A-B) Schematic showing partial PEGylation and subsequent IL-4 conjugation to AuNPs. (C-E) DLS size distribution of 30-100nm AuNP core (black), AuNP-PEG (light color), and PA4 (dark color) particles. Data from a representative synthesis. (F) PA4 DLS size distribution after IL-4 conjugation (dark pink), and after 1day in RPMI+10% HI-FBS, 37°C (light pink). DLS distribution of RPMI+10% HI-FBS (gray). Data are means±SD, n=3 (G) 30nm-core PA4 were incubated at 37°C, 5% CO_2 for 7 days and the release of IL-4 into 1% BSA or RPMI+10% HI-FBS was quantified with ELISA. Data are means±SD, n=3

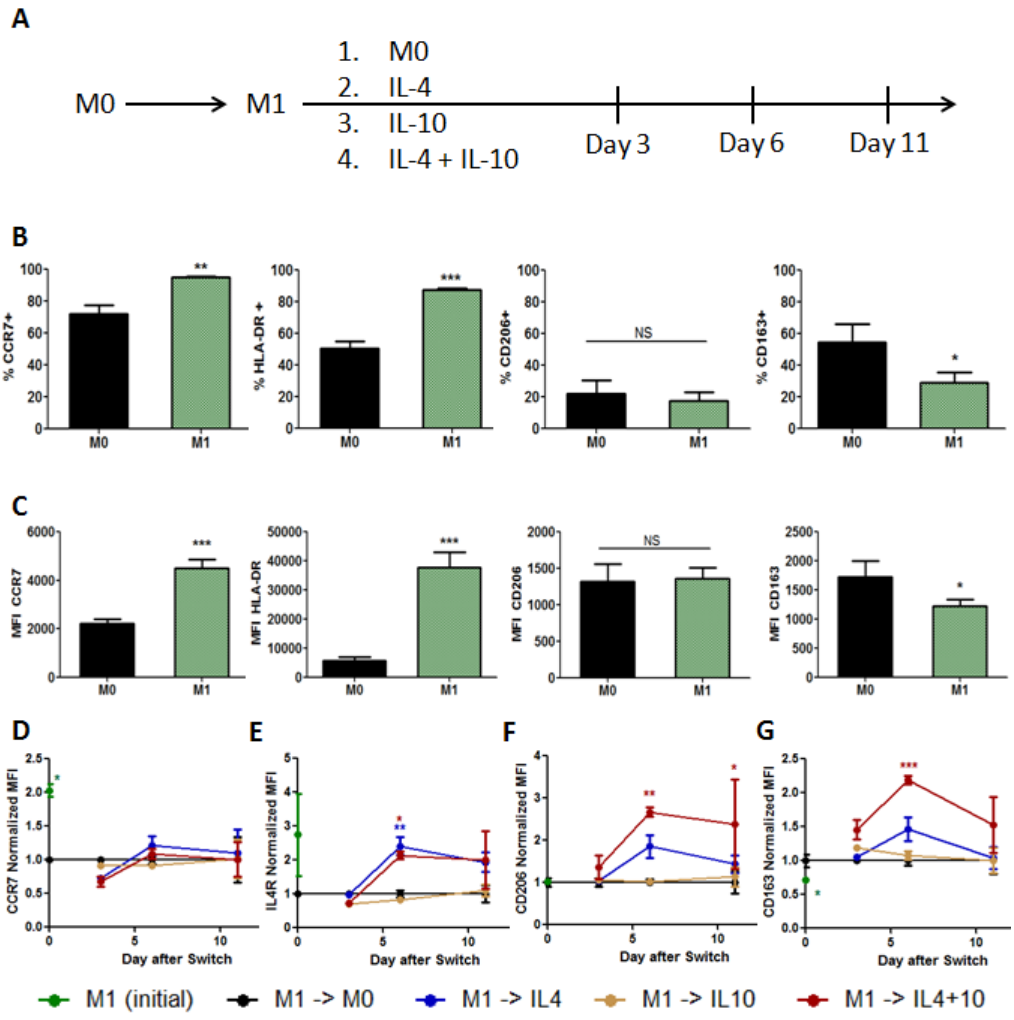
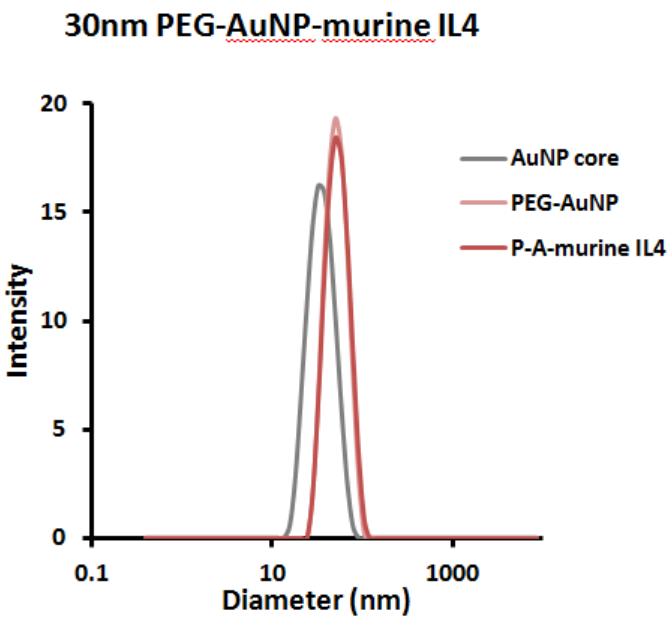


Figure 3.3. IL-4 and IL-10 can shift an M1 macrophage population towards the M2 phenotype. (A) THP-1 monocytic cells were differentiated to M0 macrophages (3 days with 100ng/mL PMA) and then polarized towards the M1 phenotype (2 days with 2400ng/mL LPS, and 20ng/mL IFN-gamma). M1 macrophages were then exposed to 40ng/mL IL-4, 40ng/mL IL-10, 40ng/mL of each cytokine, or to complete media with no additives (M0) for 3, 6, or 11 days and then analyzed by flow cytometry. (B) The percentage of the initial M1 and M0 macrophage populations that were expressing markers of M1 polarization (CCR7, HLA-DR) and M2 polarization (CD206, CD163) were assessed with flow cytometry. (C) Median fluorescent intensity (MFI) per cell of the initial M1 and M0 populations. Data are means ±SD of n=3. *P < 0.05, **P < 0.01, ***P < 0.001 (D-G) Macrophage MFI data were normalized by the time matched M0 condition to allow for accurate comparison across different timepoints. The expression levels of CCR7 (D), IL-4R (E), CD206 (F), and CD163 (G) on the initial M1 macrophage population (green) in response to IL-4 (blue), IL-10 (yellow), or IL-4 + IL-10 (red) were assessed by flow cytometry. Data are means ±SD of n=3. CCR7: *P < 0.05; IL4R: *P < 0.05 IL-4 + IL-10 vs IL-10 and M0 conditions, **P < 0.01 IL-4 vs IL-10 and M0 conditions; CD206: *P < 0.05 IL-4 + IL-10 vs M0, **P < 0.01 IL-4 + IL-10 vs IL-10 and M0 conditions; CD163: ***P < 0.001 IL-4 + IL-10 vs IL-10 and M0 conditions, also P < 0.05 vs IL-4, *P < 0.05 IL-4 + IL-10 vs M0 condition.



	Z-average (d.nm)
AuNP Core	29.9 ± 0.2
AuNP-PEG	49.2 ± 0.5
PEG-AuNP-murineIL4	50.1 ± 0.1

Figure 3.4. Representative DLS size distribution for 30nm AuNP core particles (gray) following PEGylation (light pink), and murine IL-4 conjugation (dark pink), measured in MilliQ water.

Table 3.2. Human and Murine IL-4 Conjugation

	IL-4/nm^2	% of max. packing
100nm PA4	0.075	50
60nm PA4	0.065	43
30nm PA4	0.061	41
30nm murine PA4	0.084	57

The stability of PEGylated, IL-4 conjugated particles (PA4) was assessed in vitro. Particle size was stable for 24hrs in cell culture conditions (37^{o}C, 5% CO_2, 10% HI-FBS), as there was no shift in PA4 size distribution over this time (Fig. 3.2 F). AuNP-PEG were also stable in vitro (Fig. 3.5 A). Less than 1% of human IL-4 was released into complete RPMI media or 1% BSA after 7 days, and only ~3% of murine IL-4 was released after 61 days (Fig. 3.2 G; Fig. 3.5 B).

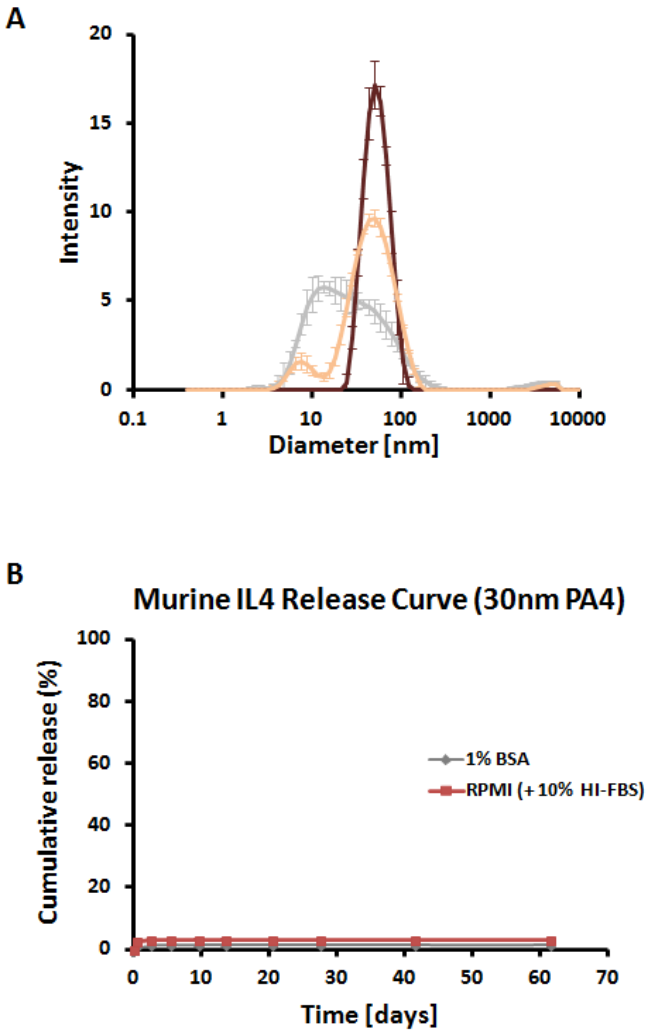


Figure 3.5. AuNP-PEG particles and murine IL-4 conjugation to AuNPs is stable. (A) The stability of AuNP-PEG particles, lacking IL-4, in cell culture media was assessed by measuring the DLS size distribution of the 30nm-core particles immediately after PEGylation and washes in MilliQ water (brown) and comparing this to the DLS size distribution of the AuNP-PEG particles after 1 day incubation in cell culture media containing 10% HI-FBS at 37°C, 5% CO_2 (orange; 12ug/mL Au). The gray line shows the DLS distribution of cell culture media containing 10% HI-FBS without nanoparticles. Data are means ±SD of n=3. (B) The release of murine IL-4 from the surface of 30nm core PA4 into 1% BSA (gray) or RPMI containing 10% HI-FBS (red) at 37°C, 5% CO_2 was quantified over the course 61 days with ELISAs. Data are means ±SD of n=3.

3.3.3 PA4 direct M2a Mφ polarization.

PA4 bioactivity was assessed in vitro with THP-1 derived human Mφs. An equivalent dose of soluble IL-4 (20ng/mL) was used as a positive control and AuNP-PEG as a negative control. PA4 and AuNP-PEG did not have a substantial effect on Mφ viability, even at 10x the IL-4 concentration used to polarize Mφs in vitro (Fig. 3.6). While 100nm-core AuNPs were slightly inflammatory, neither 30nm-core PA4 nor AuNP-PEG induced the M1 state, even at concentrations 10x those used to polarize Mφs (Fig. 3.7).

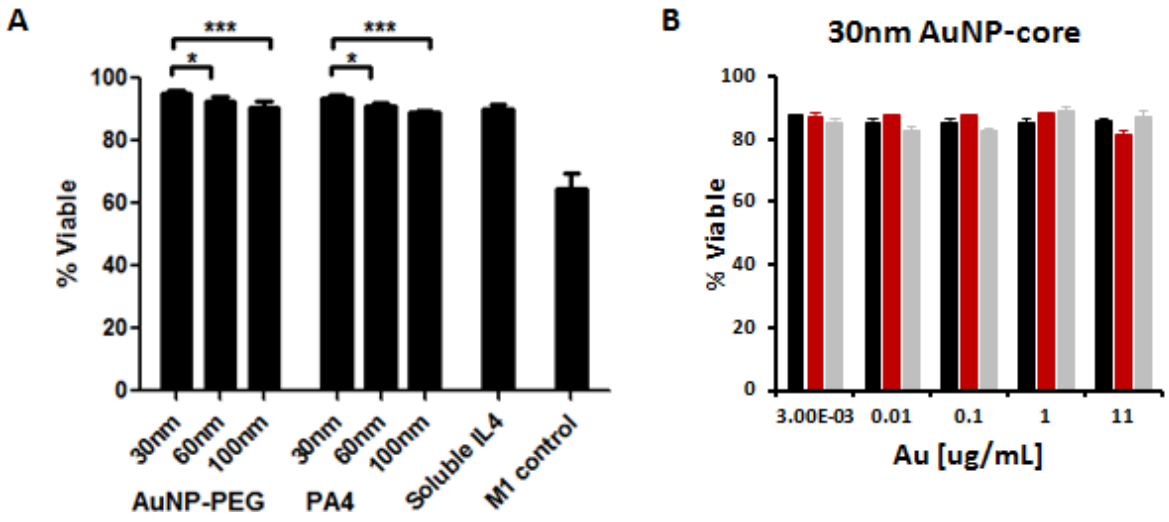


Figure 3.6. PA4 do not reduce cell viability. (A) THP-1 derived macrophages were treated for 3 days with 30, 60, or 100nm core PA4 particles delivering 20ng/mL IL-4, 20ng/mL soluble IL-4, or the same concentration of AuNP-PEG particles lacking IL-4; stimulation with 2400ng/mL LPS, and 20ng/mL IFN-gamma was used as an inflammatory M1 control. Macrophage viability was assessed with flow cytometry by staining cells with an Invitrogen fixable dead cell stain. Data are means ±SD of n=4. *P < 0.05, ***P < 0.001 (B) A dose curve of PA4 (red), AuNP-PEG (gray), and soluble IL-4 extending through the equivalent of 200ng/mL IL-4 (11ug Au/mL) shows no significant reduction in viability, assessed by flow cytometry. Data are means ±SD of n=3.

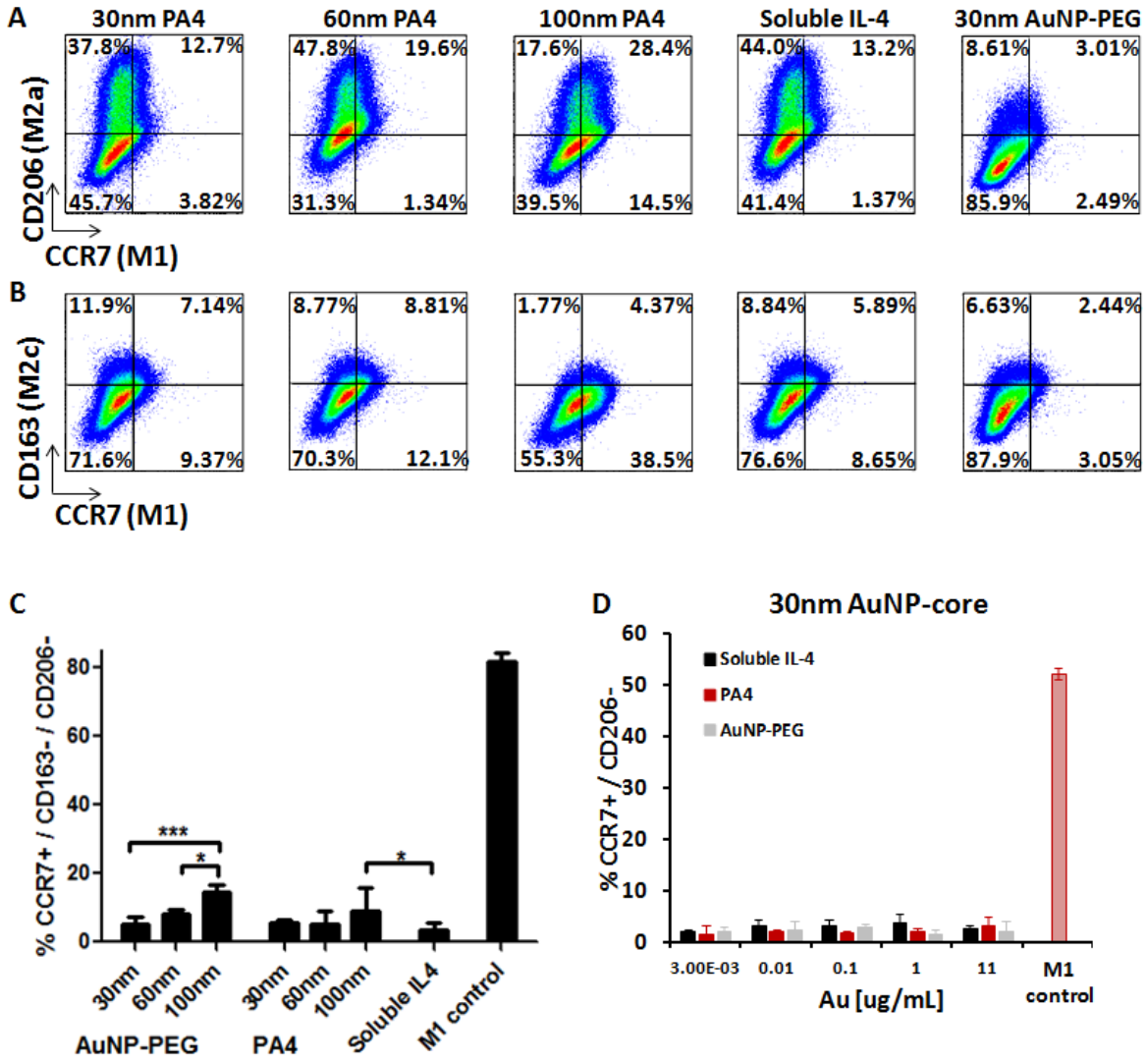


Figure 3.7. PA4 direct M2a polarization and are not inflammatory. (A-B) THP-1 derived macrophages were treated for 3 days with 20ng/mL IL-4 as PA4 or soluble IL-4; or AuNP-PEG. Plots show expression of the M2a (CD206) or M2c (CD163) vs the M1 marker (CCR7). (C) Flow cytometry was also used to assess the percentage of macrophages expressing the inflammatory M1 phenotype (CCR7+/CD163-/CD206-) following exposure to the different size nanoparticles; stimulation with 2400ng/mL LPS, and 20ng/mL IFN-gamma was used as an inflammatory M1 control. Data are means ±SD of n=4. *P < 0.05, ***P < 0.001 (D) Inflammatory phenotype expression in response to increasing doses of nanoparticles and soluble IL-4. Data are means ±SD of n=3.

Importantly, PA4 upregulated CD206 to the same extent as soluble IL-4, suggesting that conjugated IL-4 retained full bioactivity (Fig. 3.8 A; Fig. 3.7 A). As expected, neither PA4 nor soluble IL-4 induced the expression of CD163 (Fig. 3.8 B; Fig. 3.7 B), further supporting that PA4 specifically directed M2a polarization. There was no difference in the percentage of Mφs that adopted the M2a state

between PA4 and soluble IL-4 treatments (Fig. 3.8 C). Interestingly, the level of CD206 expression on M2a Mφs was significantly higher on those polarized with 30nm, as opposed to 60 or 100nm-core PA4 (Fig. 3.8 D). This may relate to the greater volume and number of 30nm-core particles in culture (Table 3.3).

Table 3.3. PA4 concentration in cell culture.

Core (nm)	ug AuNP/mL	nm^2 Au core/mL ($x10^{13}$)	coated nm^2/mL ($x10^{15}$)	coated nm^3/uL ($x10^{13}$)	number of AuNP's/uL
34.3	1.2	1.1	5.7	4.8	7.17E+08
61.4	2.4	1.2	3.0	4.4	1.32E+08
98.7	4.2	1.3	1.2	2.6	2.22E+07

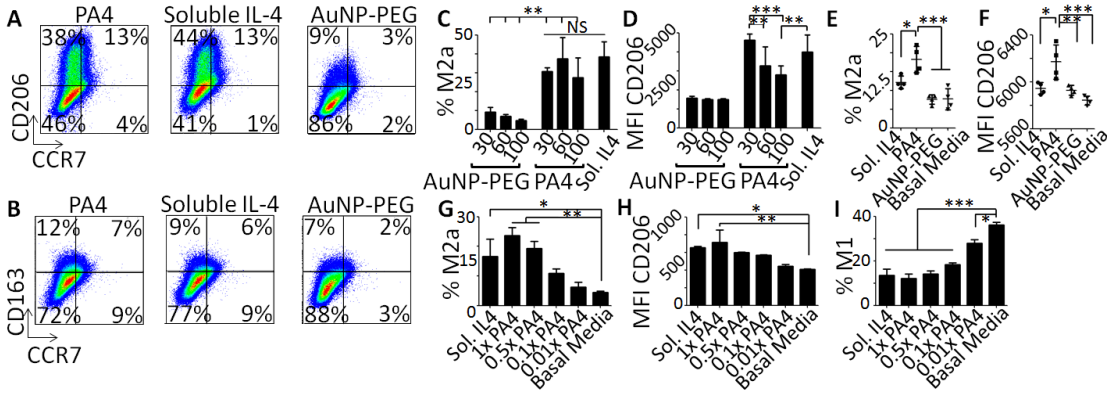


Figure 3.8. PA4 direct M2a Mφ polarization. (A-B) THP-1 derived Mφs were treated for 3 days with 20ng/mL IL-4 as 30nm PA4 or soluble (sol.) IL-4, or 30nm AuNP-PEG. Plots show expression of the M2a (CD206) or M2c (CD163) vs the M1 marker (CCR7). (C) Percentage of M2a (CCR7-/CD163-/CD206+) Mφs. (D) CD206 median fluorescent intensity (MFI), within the CD206+ gate. (E-F) Mφs were treated for 1 day with 20ng/mL IL-4 as 30nm PA4 or soluble IL-4, AuNP-PEG, or basal RPMI. On day 5, flow cytometry was used quantify M2a (CCR7-/CD206+) Mφs. (F) CD206 MFI, within the CD206+/CCR7- gate. Data are means±SD, n=4 *P<0.05, **P<0.01, ***P<0.001 (G-I) Mφs were treated with 20ng/mL IL-4 as soluble IL-4 or PA4 with varying degrees of IL-4 conjugation, 1x, 0.5x, 0.1x and 0.01x (relative to the PA4s used throughout the paper). (G) Flow cytometry was used quantify M2a (CD206+/CCR7-) Mφs. (H) CD206 MFI, within the CD206+ gate. (I) Percentage of M1 (CD206-/CCR7+) Mφs. Data are means±SEM, n=4 *P<0.05, **P<0.01, ***P<0.001, Dunnett's comparison vs basal media control.

To determine if the stability of polarization driven by soluble IL-4 and PA4 was distinct, the initial soluble IL-4 or PA4 media was replaced with basal media after 1 day. A higher fraction of Mφs treated with PA4 retained M2a polarization (Fig. 3.8 E). Furthermore, the level of CD206 expression on PA4-induced M2a Mφs was still elevated on day 5, while Mφs that had been polarized with soluble IL-4 demonstrated levels comparable to those in negative controls (Fig. 3.8 F).

To determine if the multivalency of IL-4 presentation on PA4 contributed to the polarization effects, PA4 with varying degrees of IL-4 conjugation were made. Mφs polarized with PA4 with higher IL-4 valency demonstrated higher levels of M2a polarization (Fig. 3.8 G-H) and lower levels of the inflammatory state (Fig. 3.8 I). All groups were treated with 20ng/mL IL-4.

3.3.4 PA4 enhance muscle fiber regeneration and contraction force following ischemic injury.

Mice with ischemic hindlimbs were treated on day 3 with TA intramuscular (IM) injection of 2ug IL-4 as 30nm-core PA4 or soluble IL-4; AuNP-PEG or PBS, and analyzed on days 6 and 15 (Fig. 3.9 A). Immediately following surgery, blood flow was reduced by 60% in all conditions (Fig. 3.10 A). Ischemic injury also resulted in reduced TA mass on day 6, but was normalized by day 15 (Fig. 3.10 B,C). Visual inspection revealed that AuNPs distributed throughout the TA, but not surrounding muscle, and were retained at least 3 days following injection (Fig. 3.9 B).

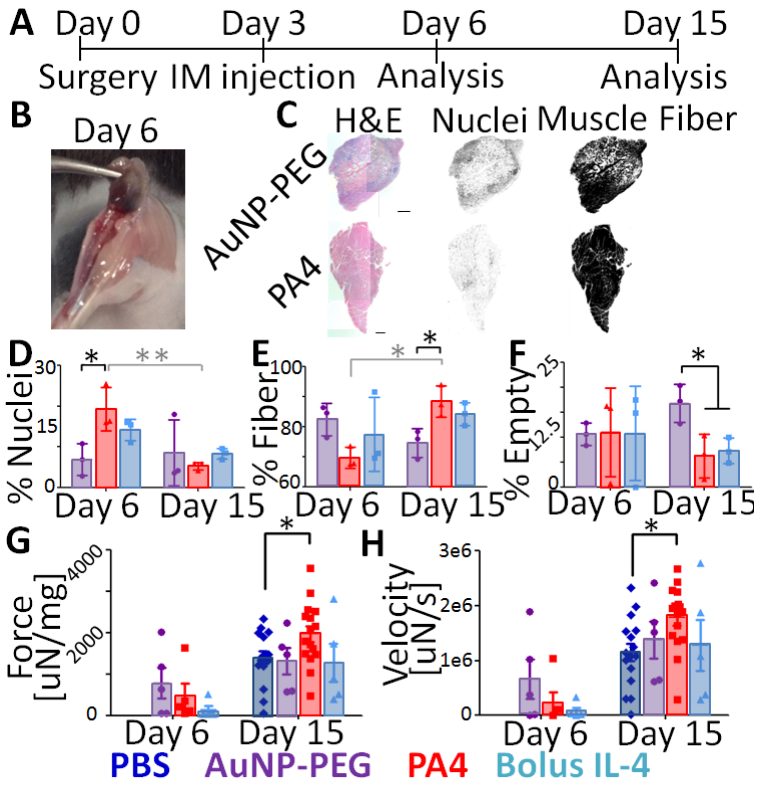


Figure 3.9. PA4 enhance muscle fiber regeneration and contraction force following ischemic injury. (A) Timeline showing surgery, treatment and TA analysis. (B) Representative image showing the purple hue of AuNPs throughout the TA, day 6. (C) Representative H&E of ischemic TAs on day 15, haematoxylin (middle) and eosin (last column) channels. (Scale bars=1.5mm) (D-F) Percentage of the TA cross-section associated with cell nuclei, muscle fibers or empty area. Data are means±SD, n=3 *P<0.05, **P<0.01. Due to large variations in empty area on day 6 this data was excluded from statistics. (G-H) Maximum contraction force (25V, 250Hz) and velocity. Force was normalized to TA mass. Data are means±SEM. Day 6, n=5; day 15: n=16 for PA4 and PBS, n=5 for A-PEG and bolus IL-4. *P<0.05, Bonferroni planned comparison

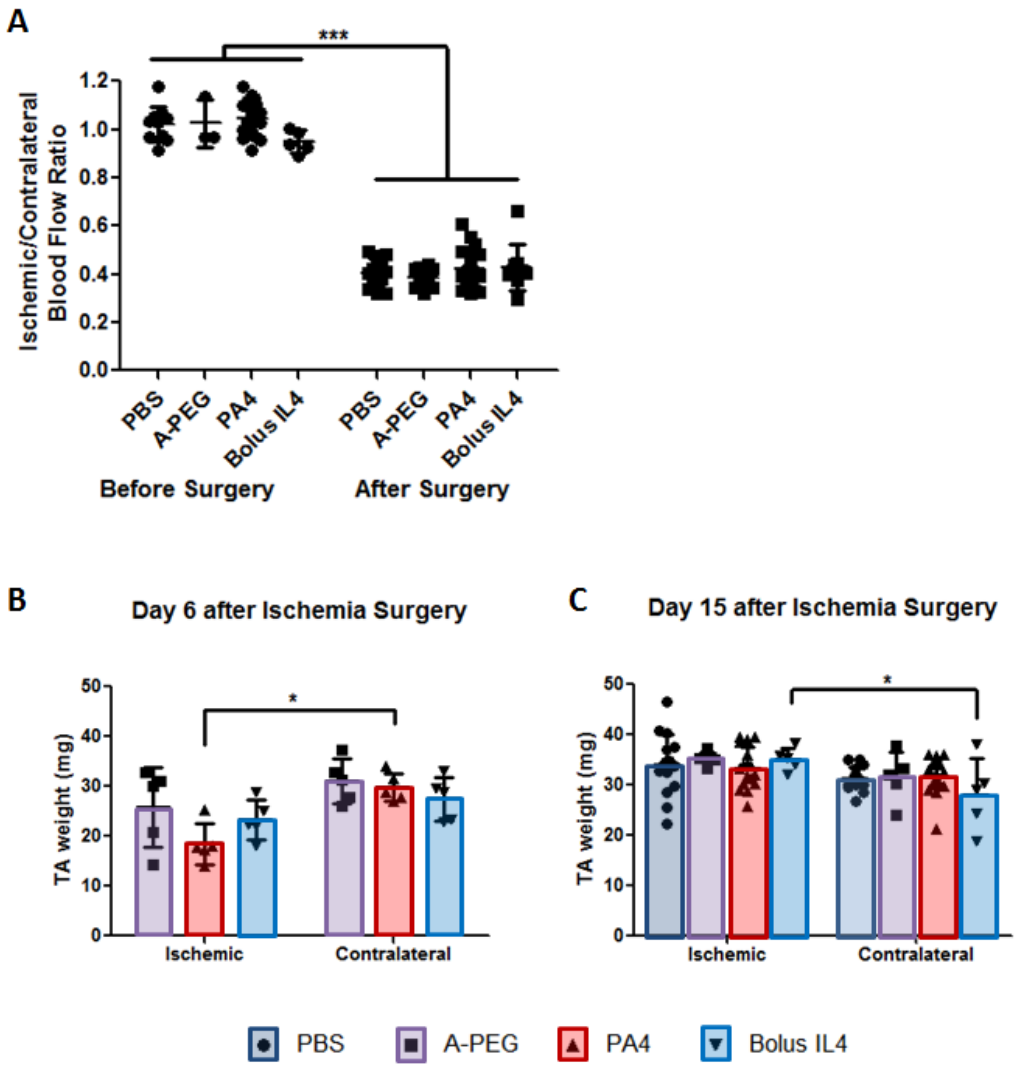


Figure 3.10. Surgical induction of ischemia reduces blood flow and decreases muscle mass. (A) LDPI blood perfusion measured immediately before and after surgical induction of ischemia. LDPI readings were normalized to the contralateral (uninjured) limb. (B-C) TA muscle mass measured ex vivo, on day 6 (B), and day 15 (C) after surgery. Data are means ±SD of 3-16 mice per group.

To analyze the TA muscle, H&E and Mason's trichrome staining was used to quantify muscle fiber area, cell nuclei [28], and fibrosis (Fig. 3.9 C, Fig. B4). Immune cell infiltration was greater in TAs treated with PA4 compared to TAs treated with AuNP-PEG, day 6 (Fig. 3.9 D). However by day 15, immune cell densities had decreased substantially in all groups (Fig. 3.9 C,D). Muscle fiber area was significantly increased on day 15 in TAs treated with PA4 compared to AuNP-PEG (Fig. 3.9 C,E), and

minimal to no fibrosis was observed (Fig. B4). Consistently, TAs treated with AuNP-PEG showed the greatest area of empty space (lacking muscle fibers or cell infiltration) compared to TAs treated with either soluble IL-4 or PA4, day 15 (Fig. 3.9 F).

Contraction force and velocity of damaged and treated TAs were analyzed on days 6 and 15 to assess function. Mass normalized force and velocity were measured after tetanic stimulation (Fig. 3.9 G,H). Six days after induction of ischemia, mice in all treatment groups showed reduced muscle function, in comparison to the uninjured contralateral TA (Fig. 3.11). By day 15 however, ischemic TAs treated with PA4 showed significant increases in contraction force, 1.4-fold compared to ischemic TAs treated with PBS, and 1.6-fold compared to the contralateral TA. Treatment with bolus IL-4 or AuNP-PEG resulted in no improvement in force over mice treated with PBS. A similar trend was seen in contraction velocity. Improved TA function was not associated with improved blood perfusion, as perfusion was similar in all groups (Fig. 3.12).

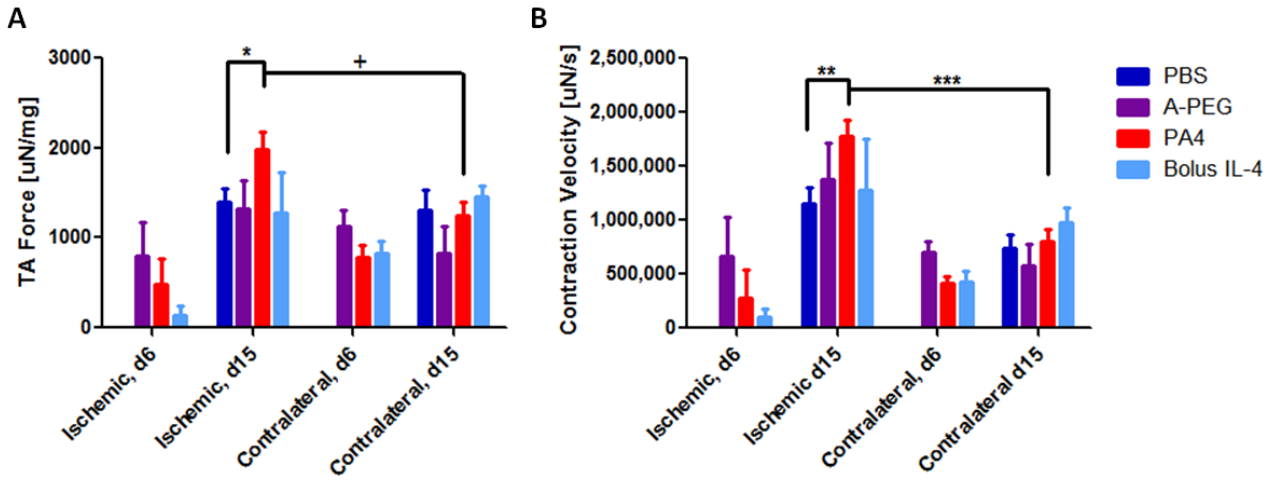


Figure 3.11. PA4 improve muscle contraction force and velocity following unilateral ischemic injury. (A) Maximum contraction force of the TA muscle isolated from the ischemic limb in comparison to that from the uninjured contralateral limb on days 6 and 15 after surgery. Force was normalized to TA mass. (B) Contraction velocity of the TA muscles isolated from the ischemic and uninjured contralateral limbs on days 6 and 15 after surgery. Data are means±SEM. Day 6: n=5; day 15: n=16 for PA4 and PBS, n=5 for A-PEG and bolus IL-4 groups. *P<0.05, Bonferroni planned comparison; +P<0.05, 2-way ANOVA (considers each condition, ischemic vs. contralateral); **P<0.01, ***P<0.001, 2-way ANOVA

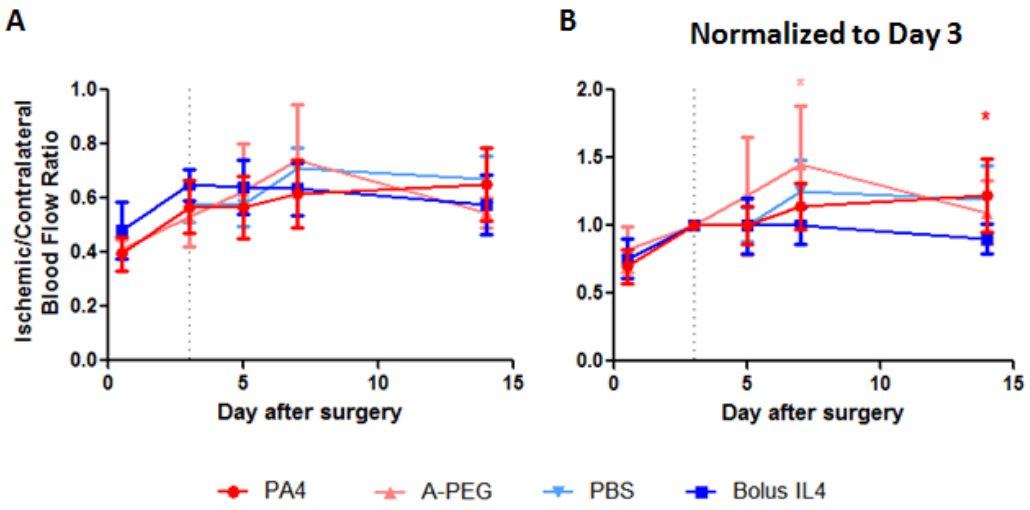


Figure 3.12. PA4 treatment does not significantly impact blood perfusion. (A) LDPI blood perfusion measured at various timepoints after surgical induction of ischemia. LDPI readings were normalized to the contralateral (uninjured) limb. (B) The ischemic/contralateral ratio LDPI measurements were normalized to the day 3 reading, to more easily compare the effect of treatment (administered on day 3 after surgery). Data are means ±SD of 5-16 mice per group. *(pink) $P < 0.05$ AuNP-PEG vs bolus IL-4 and PA4; *(red) $P < 0.05$ PA4 vs bolus IL-4

3.3.5 Mφs are the predominant infiltrating immune cell following ischemic injury.

To probe the mechanism by which PA4 treatment improved muscle structure and function, flow cytometry was used to analyze cell recruitment and phenotype in the injured TA. As suggested by H&E, CD45+ immune cells were cleared more rapidly following PA4 treatment compared to PBS (Fig. 3.13 A). On day 15, the percentage of CD45+ cells in the injured TA was elevated in the PBS group but returned to levels comparable to those observed in the contralateral TA in the PA4 group (Fig. 3.14 A). Flow cytometry data was normalized to TA mass (Fig. 3.14 B). The same trend was seen in the mass of CD45+ cells in the TAs (Fig. 3.13 B). Recruited CD45+ cells were characterized by expression of surface markers (Fig. 3.14 C). The level of Mc in the injured TAs returned to levels comparable to that observed in the contralateral by day 6, and the level of Mφs returned to uninjured levels by day 15 in mice treated with PA4 (Fig. 3.13 C,D). Conversely, both Mc and Mφs were still elevated on day 15 in the PBS group. PA4 treatment specifically reduced the level of inflammatory Mc ($Ly6C^{hi}$/ $Gr1^{lo}$) (Fig. 3.13 F).

Inflammatory Mc were normalized to levels seen in the contralateral TA by day 6, while their presence was still elevated in the PBS group (Fig. 3.13 G).

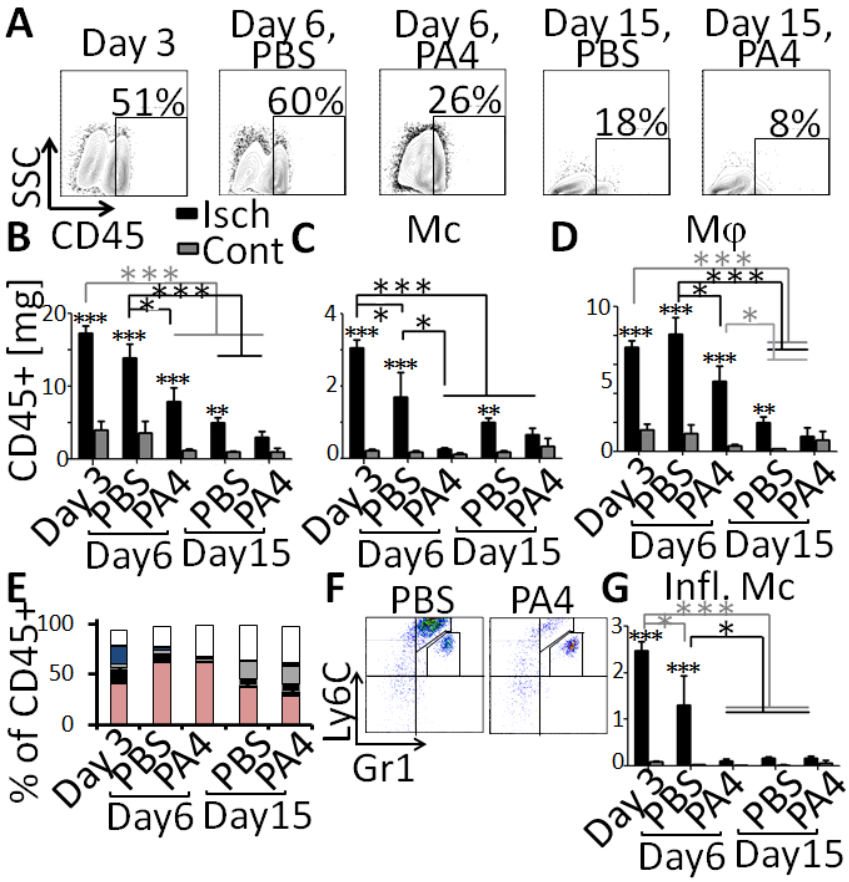


Figure 3.13. Immune cells are cleared more rapidly following PA4 treatment. (A) Plots show the percentage of TA cells that were CD45+. (B-D) CD45+, Mc (CD45+/CD11b+/CD3-/F4/80-/Gr1$^{lo\ or\ -}$) and Mφ (CD45+/CD11b+/CD3-/F4/80+) data normalized to TA mass [mg]. (E) Distribution of CD45+ cells in the TA: Mφs (pink; CD11b+/CD3-/F4/80+), inflammatory Mc (black; Ly6C^{Hi}/Gr1^{Lo}), Mc (black above gray border; Ly6C^{Hi}/Gr1-), patrolling Mc (gray; Ly6C$^{Lo\ or\ -}$/Gr1-), neutrophils (blue; Ly6C^{Lo}/Gr1^{Hi}), T cells (gray above the blue; CD3+), CD11b-/CD3- (white). (F) Gating of myeloid (CD45+/CD11b+/CD3-/F4/80-) cells on day 6. Plots show diminishing inflammatory Mc (Ly6C^{Hi}/Gr1^{Lo}) with PA4 treatment. (G) Inflammatory Mc (CD45+/CD11b+/CD3-/F4/80-/Gr1^{Lo}/Ly6C^{Hi}) in TA normalized by mass [mg]. Data are means±SEM, n=5-10 *P<0.05, **P<0.01, ***P<0.001, stars above columns indicate significance vs contralateral

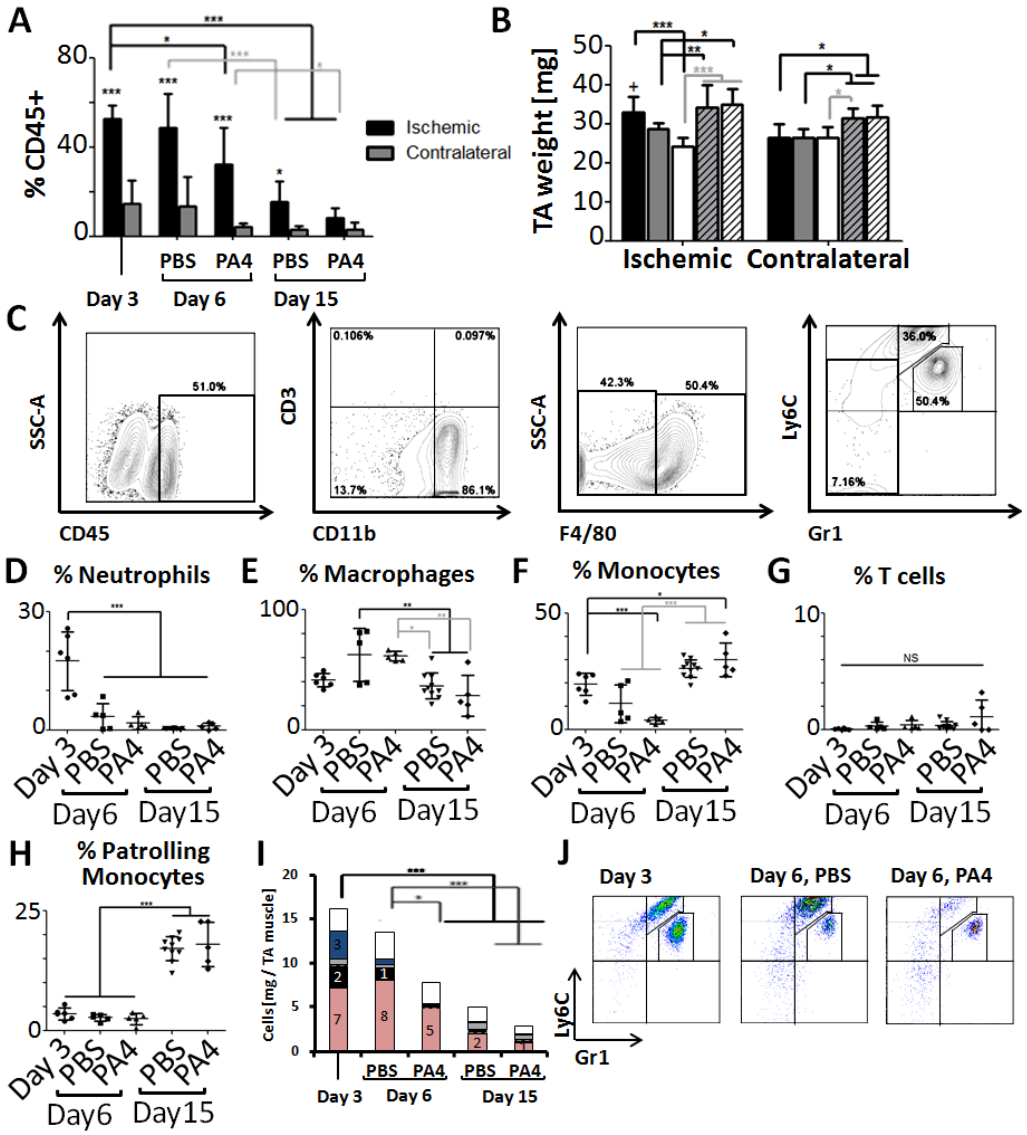


Figure 3.14. Characterization of immune cell recruitment to the TA muscle following ischemic injury. (A) The percentage of cells isolated from the ischemic and contralateral (uninjured) TA muscles that were CD45+ immune cells were quantified with flow cytometry. (B) Weight of the isolated TA muscles at the time of treatment, day 3 (black bars), day 6 after surgery and PBS treatment (gray bars) or PA4 treatment (white bars), and day 15 after surgery and PBS treatment (gray stripped bars) or PA4 treatment (white stripped bars). (C) Gating strategy used to identify the immune cell populations. (D-H) The percentage of CD45+ immune cells collected from the TA muscles that were neutrophils (CD11b+/CD3-/ F4/80-/Gr1^{hi}/Ly6C^{lo}) (D), macrophages (CD11b+/CD3-/ F4/80+) (E), monocytes (CD11b+/CD3-/ F4/80-/Gr1$^{lo\ or\ -}$) (F), T cells (CD11b-/CD3+) (G), or patrolling monocytes (CD11b+/CD3-/ F4/80-/Gr1-/Ly6C$^{lo\ or\ -}$) (H). (I) The presence of each immune cell population was normalized to the TA mass; macrophages (pink; CD11b+/CD3-/F4/80+), inflammatory monocytes (black; Ly6C^{Hi}/Gr1^{Lo}), monocytes (black above gray border; Ly6C^{Hi}/Gr1-), patrolling monocytes (gray; Ly6C$^{Lo\ or\ -}$/Gr1-), neutrophils (blue; Ly6C^{Lo}/Gr1^{Hi}); T cells (dark gray above the blue box; CD11b-/CD3+), T cells (light gray above the blue box; CD11b+/CD3+), CD11b-/CD3- (white). (J) Gating of myeloid (CD45+/CD11b+/CD3-/ F4/80-) cells. Plots show diminishing inflammatory monocytes (Ly6C^{Hi} /Gr1^{Lo}) with PA4 treatment. All data are means ±SD of 5-10 mice per group. *P < 0.05, **P < 0.01, *** P < 0.001

Although PA4 treatment resulted in more rapid clearance of immune cells, it did not alter the distribution of CD45+ cells. The relative percentage of neutrophils, Mφs, Mc, T cells and patrolling Mc were unaltered by PA4 treatment (Fig. 3.14 D-H). These cell types followed patterns expected of a typical inflammatory response; neutrophils were present on day 3 and rapidly cleared, peak Mφ infiltration occurred on day 6, and patrolling Mc were replenished on day 15. Importantly however, Mφs were the predominant infiltrating immune cell representing 42% on day 3 and 60% on day 6 of the CD45+ cells (Fig. 3.13 E; Fig. 3.14 I).

3.3.6 PA4 enhance muscle regeneration by directing M2a Mφ polarization

To determine if PA4 treatment promoted a shift in Mφ phenotype away from the M1 and towards the M2a state, levels of CD206 (M2a) and CD80 (M1) expression were assessed (Fig. 3.15 A,C,E). ~20% of Mφs from TAs treated with PA4 expressed the M2a phenotype (CD80-/CD86-/CD163+/CD206+), but only ~10% were M2a in the PBS group (Fig. 3.15 B). Further, mice treated with PA4 showed lower levels of M1 (CD80+/CD163-/CD206-) Mφs on days 9-15 than mice treated with PBS (Fig. 3.15 D). While both bolus IL-4 and PA4 reduced the percentage of CD80+ Mφs on day 6, bolus IL-4 was as ineffective as AuNP-PEG at promoting the M2a state on day 15 (Fig. 3.16).

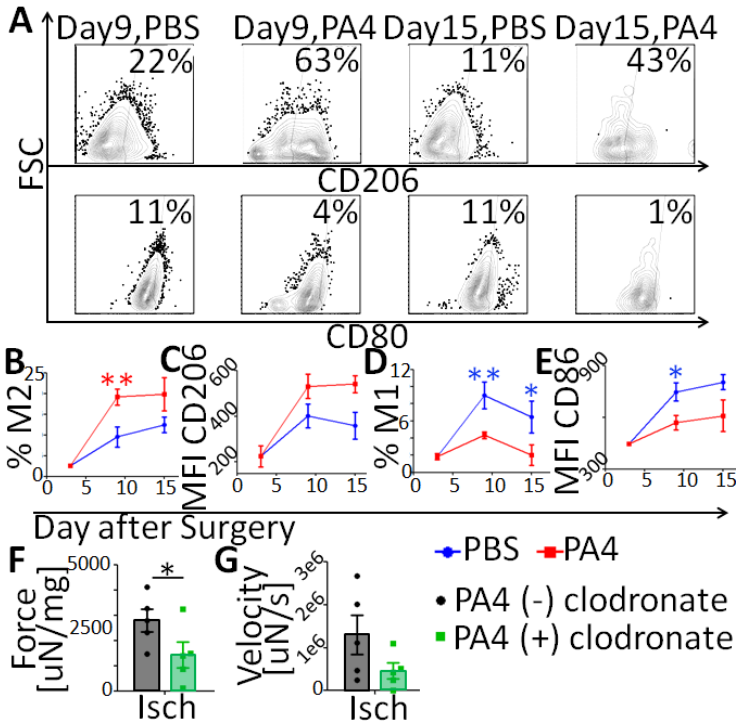


Figure 3.15. PA4 enhance muscle regeneration by directing M2a polarization. (A) Plots show the percentage of Mφs (F4/80+/CD11b+) from the ischemic TAs expressing CD206 (M2a), CD80 (M1). (B,D) Percentage of Mφs expressing the M2 (CD80-/CD86-/CD163+/CD206+) or M1 phenotype (CD80+/CD163-/CD206-). (C,E) CD206 (M2a) or CD86 (M1) MFI. Data are means±SEM, n=3-5 *P<0.05, **P<0.01 (F-G) Mice were treated with either clodronate or PBS-liposomes and PA4. Maximum TA contraction force and velocity of 3 tests, day 9. Force was normalized to TA mass. Data are means±SEM, n=5 *P<0.05

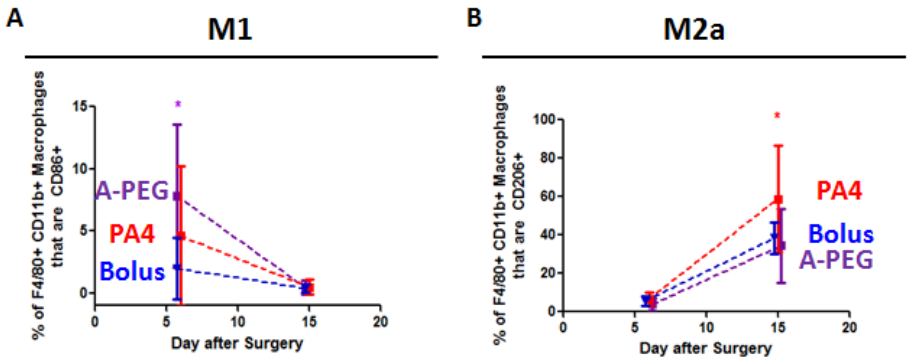


Figure 3.16. Bolus IL-4 is not as effective as PA4 at shifting macrophage polarization in vivo at longer timepoints. Flow cytometry was used to characterize the polarization state of macrophages isolated from the injured TA muscles on days 6 and 15 after surgery. CD86 expression was used to identify M1 macrophages (A), and CD206, M2a macrophages (B). Data are means ±SD, n=5. For CD86 expression (A) *P < 0.05 for bolus IL-4 vs. AuNP-PEG; for CD206 expression (B) *P < 0.05 for PA4 vs. AuNP-PEG.

To determine if the shift from the M1 towards the M2a state played a role in promoting muscle regeneration, clodronate was used to deplete Mφs prior to surgery. Following Mφ depletion and PA4 treatment, TA contraction force and velocity were reduced 1.9 and 2.8-fold, respectively, compared to mice that received PA4 treatment without Mφ depletion (Fig. 3.15 F,G). These data suggest that Mφs play a central role in the mechanism by which PA4 promotes functional muscle regeneration.

3.4 Discussion

The development of therapeutics that can control inflammation are of considerable interest, as failed resolution of inflammation and uncontrolled Mφ activation contribute to the progression of many diseases [1,29]. Here we show that IL-4 conjugated gold nanoparticles shift Mφs away from the M1 and towards the M2a state in vivo following ischemic skeletal muscle injury. PA4 driven Mφ polarization was more stable than that driven by soluble IL-4 in vitro, and resulted in improved muscle fiber regeneration and more rapid immune cell clearance in vivo. Ultimately, PA4 treatment improved TA contraction force and velocity 2wks following injury.

The findings of these studies demonstrate that Mc/Mφs play a critical role in promoting muscle regeneration following ischemic injury. Mφs were the predominant infiltrating immune cell (Fig. 3.13 E) and their depletion with clodronate inhibited regeneration of muscle contraction force and velocity (Fig. 3.1 G,H), and was coincident with a significant reduction in TA mass (Appendix B, Fig. B1). This is in accord with previous reports that showed that Mc/Mφ depletion resulted in prolonged clearance of necrotic myofibers and increased muscle fat accumulation, and knock-out of a Mφ chemotaxtic factor impaired histologic muscle regeneration [30-31]. Mφs have been shown to support myogenesis through the secretion of growth factors and conditional deletion of the IGF-1 gene in myeloid cells significantly impaired muscle regeneration [3]. The interplay between Mc/Mφs and myogenesis suggests that manipulation of Mφ function has the potential to improve muscle regeneration.

This study demonstrates that partial PEGylation of AuNPs, then IL-4 conjugation, yields monodisperse and stable PA4 for bioactive IL-4 delivery. AuNPs have been widely investigated for their use in drug delivery as they provide a biologically inert, non-immunogenic substrate [25,26,32,33]. Furthermore, by modifying surface chemistry, via PEGylation, their pharmacokinetics and in vivo biodistribution can be tuned [34]. Partial PEGylation in this study allowed the subsequent conjugation of human and murine IL-4 directly to the remaining Au surface (Tables 3.2), and importantly, resulted in PA4 that were stable in 10% serum in vitro (Fig. 3.2 F), and following IM injection in vivo (Fig. 3.9 B). PA4 showed no negative effects on Mφ viability in vitro, nor was it inflammatory, negatively effect blood perfusion (Figs. 3.6, 3.7, 3.12), TA weight, or contraction function in vivo (Fig. 3.9, 3.10). Importantly, conjugated IL-4 retained full bioactivity, as indicated by PA4 driven M2a polarization (Fig. 3.8). Mφs that had been polarized with PA4 expressed higher and more stable levels of CD206 than those polarized with soluble IL-4, and increasing IL-4 valency resulted in increasing levels of M2a polarization (Fig. 3.8 E-H). Various methods for delivery of IL-4 have previously been studied, including conjugation to decellularized scaffolds, encapsulation into mesoporous silica NPs, and the delivery of IL-4 encoding DNA in hyaluronic acid-poly(ethyleneimine) NPs [35-37]. However, to date these approaches have not resulted in therapeutic improvements in models of inflammation or injury. Conjugation of a targeting antibody to IL-4, in combination with dexamethasone, has shown therapeutic improvements in a murine arthritis model, but this approach may result in complications accompanying antibody therapy and require the development of new conjugation chemistries to target tissues affected by other diseases [38-39]. IL-4 conjugation to Au allowed for IM injection of non-immunogenic PA4 into the ischemic muscle; providing a clinically relevant model to probe both their ability to direct Mφ polarization in an inflammatory microenvironment in vivo, and the effects of Mφ polarization on therapeutic muscle regeneration.

PA4 treatment significantly enhanced functional muscle regeneration following ischemic injury. Inflammatory Mc were cleared more rapidly (Fig. 3.13 F,G), histologic muscle fiber regeneration (Fig.

3.9 C-F) and muscle contraction force and velocity were improved (Fig. 3.9 G,H) with PA4 treatment compared to negative controls. TAs treated with PA4 showed a 1.4 and 1.6-fold increase in contraction force and velocity, respectively, compared to muscles treated with PBS. Previous studies using mouse models of ischemic muscle injury report comparable enhancements in muscle force 2wks after delivery of growth factors and myogenic cells. In those studies, scaffold delivery of VEGF, IGF-1, and/or myoblasts resulted in 1.5-3.0-fold increases in TA contraction force over control conditions [40-42]. The present study suggests that similar functional improvements in muscle regeneration can be achieved by immune modulation with a single factor.

PA4 treatment enhanced muscle regeneration by directing M2a Mφ polarization. PA4 injection shifted the balance of Mφs away from the M1 and towards the M2a state (Fig. 3.15, 3.16). Treating TAs via IM injection on day 3 allowed the initial recruitment of M1 Mφs to occur, timing PA4 treatment with Mφ recruitment. Clodronate depletion of Mc/Mφs prior to treatment with PA4 significantly diminished the recovery of TA contraction force and velocity (Fig. 3.15 F,G).This is consistent with previous findings that genetic deletion of microRNA-155, an RNA that does not regulate satellite cells but rather JAK-STAT signaling and the balance between M1 and M2 Mφs, substantially delayed muscle regeneration [16]. Other studies have shown that conditional deletion of the IGF-1 gene or CREB-binding, both of which inhibit induction of the M2 state, severely inhibited muscle fiber regeneration [3,17]. M2 Mφs are critical for regeneration of functional muscle fibers, in part, because they promote differentiation of myogenic precursor cells and formation of mature myotubes [15]. In addition to directing M2a polarization, PA4 may have also directly affected myogenesis, as it has been shown that IL-4 directs myoblast fusion with myotubes [43]. However, the loss of functional improvement following Mc/Mφ depletion in the current study suggests that directing Mφ phenotype is a key aspect of PA4 treatment. Further, as it has been shown that IL-4 is capable of driving the accumulation of M2 Mφs through self-renewal [19], PA4 treatment may sustain M2a polarization via both polarization of recruited M1 Mφs and through direct self-renewal of M2 Mφs.

The results of these studies indicate that IL-4 conjugated gold nanoparticles can be used to direct M2a Mφ polarization in an inflammatory microenvironment following ischemic muscle injury in vivo. With the increasing realization that chronic inflammation plays a role in many diseases, and that M2 Mφ polarization can potentially ameliorate many conditions, the ability of PA4 to direct Mφ polarization may be beneficial in the treatment of diverse conditions, including muscular dystrophies, inflammatory metabolic diseases like diabetes [44] and degenerative diseases.

3.5 References

[1] N. Kamaly et al., "Development and in vivo efficacy of targeted polymeric inflammation-resolving nanoparticles," *Proc Natl Acad Sci USA,* vol. 110, no. 16, pp. 6506-6511, 2013.

[2] P. Murray and T. Wynn, "Protective and pathogenic functions of macrophage subsets," *Nature Reviews,* vol. 11, no. 11, pp. 723-737, 2011.

[3] J. Tonkin et al., "Monocyte/Macrophage-derived IGF-1 Orchestrates Murine Skeletal Muscle Regeneration andModulates Autocrine Polarization," *Molecular Therapy,* vol. 23, no. 7, pp. 1189-1200, 2015.

[4] A. Mantovani, S. Biswas, M. Galdiero, A. Sica and M. Locati, "Macrophage plasticity and polarization in tissue repair and remodeling," *J Pathol,* vol. 229, pp. 176-185, 2013.

[5] A. Mantovani, C. Garlanda and M. Locati, "Macrophage Diversity and Polarization in Atherosclerosis: A Question of Balance," *Arterioscler Thromb Vasc Biol,* vol. 29, pp. 1419-23, 2009.

[6] X. Zhang and D. Mosser, "Macrophage activation by endogenous danger signals," *J Pathol,* vol. 214, pp. 161-78, 2008.

[7] R. Kinne, B. Stuhlmuller and G. Burmester, "Cells of the synovium in rheumatoid arthritis. Macrophages," *Arth Res Ther,* vol. 9, no. 6, pp. 224-39, 2007.

[8] N. Fahy et al., "Human osteoarthritic synovium impacts chondrogenic differentiation of mesenchymal stem cells via Macrophage polarization state," *Huma Osteoarth Carti,* vol. 22, no. 8, pp.1167-75, 2014.

[9] J. Mikita et al., "Altered M1/M2 activation patterns of monocytes in severe relapsing experimental rat model of multiple sclerosis. Amelioration of clinical statue by M2 activated monocyte administration," *Mult Scler J,* vol. 17, no.1, pp. 2-15, 2011.

[10] A. Sindrilaru et al., "An unrestrained proinflammatory M1 Macrophage population induced by iron impairs wound healing in humans and mice," *J clinic invest,* vol. 121, no. 3, pp. 985-97, 2011.

[11] Y. Kharraz, J. Guerra, C. Mann, A. Serrano and P. Munoz-Canoves, “Macrophage Plasticity and the Role of Inflammation in Skeletal Muscle Repair,” *Medi Inflamm,* doi: 10.1155/2013/491497, 2013.

[12] J. Tidball and S. Villalta, “Regulatory interactions between muscle and the immune system during muscle regeneration,” *Am J Physiol Regul Integr Comp Physio,* vol. 298, pp. R1173-R1187, 2010.

[13] A. Wagers and I. Conboy, “Cellular and molecular signatures of muscle regeneration: Current concepts and controversies in adult myogenesis,” *Cell,* vol. 122, no. 5, pp.659-67, 2005.

[14] J. Engert, E. Berglund and N. Rosenthal, “Proliferation precedes differentiation in IGF-1-stimulated myogenesis,” *J Cell Biol,* vol. 135, no. 2, pp. 431-40, 1996.

[15] M. Saclier et al., “Differentially Activated Macrophages Orchestrate Myogenic Precursor Cell Fate During Human Skeletal Muscle Regeneration,” *Stem Cell,* vol. 31, no. 2, pp. 384–396, 2013.

[16] M. Nie et al., “MicroRNA-155 facilitates skeletal muscle regeneration by balancing pro- and anti-inflammatory Macrophages,” *Cell Death Dis,* vol. 7, p. e2261, 2016.

[17] D. Ruffell et al., “A CREB-C/EBP-beta cascade induces M2 Macrophage-specific gene expression and promotes muscle injury repair,” *Proc Natl Acad Sci USA, vol.* 106, no. 41, pp. 17475-80, 2009.

[18] L. Arnold et al., “Inflammatory monocytes recruited after skeletal muscle injury switch into antiinflammatory macrophages to support myogenesis,” *JEM,* vol. 204, pp. 1057-69, 2007.

[19] S. Jenkins et al., “Local Macrophage Proliferation, Rater than Recruitment from the Blood, Is a Signature of Th2 Inflammation,” *Sci,* vol. 332, pp. 1284-88, 2011.

[20] M. Racke et al., “Cytokine-induced immune deviation as a therapy for inflammatory autoimmune disease,” *J Exp Med,* vol. 180, pp. 1961-66, 1994.

[21] A. Horsfall et al., “Suppression of collagen-induced arthritis by continuous administration of IL-4,” *J Immunol,* vol. 159, pp. 5687-96, 1997.

[22] K. Ghoreschi et al., “Interleukin-4 therapy of psoriasis induces Th2 responses and improves human autoimmune disease,” *Nat Med,* vol. 9, no. 1, pp. 40-46, 2003.

[23] Z. Zidek, P. Anzenbacher and E. Kmonickova, "Current status and challenges of cytokine pharmacology," *Br J Pharmacol,* vol. 157, no. 3, pp. 342–361, 2009.

[24] S. D. Perrault and W. C. Chan, "Synthesis and Surface Modification of Highly Monodispersed, Spherical Gold Nanoparticles of 50-200 nm," *JACS,* vol. 131, no. 47, pp. 17042-17073, 2009.

[25] B. Merchant, “Gold, the noble metal and the paradoxes of its toxicology,” *Biologicals,* vol. 26, no. 1, pp. 49-59, 1998.

[26] S. Root, G. Andrews, R. Kniseley and M. Tyor, “The distribution and radiation effects of intravenously administered colloidal Au^{198} in man,” *Cancer,* vol. 7, no. 5, pp. 856-866, 1954.

[27] J. Ward et al., “Comparison of auranofin, gold sodium thiomalate, and placebo in the treatment of rheumatoid arthritis,” *Arthritis Rheuma,* vol. 26, no. 11, pp. 1303-1315, 1983.

[28] M. Van Putten et al., "A 3 months mild functional test regime does not affect disease parameters in young mdx mice," *Neuromuscular Discord,* vol. 20, no. 4, pp. 273-280, 2010.

[29] S. Serhan et al., “Resolution of inflammation: state of the art, definitions and terms,” *FASEB J,* vol. 21, no. 2, pp. 325-332, 2007.

[30] M. Summan et al., “Macrophages and skeletal muscle regeneration: a clodronate-containing liposome depletion study,” *Am J Physiol Regul Integr Comp Physiol,* vol. 209, no. 6, pp. R1488-95, 2006.

[31] S. Bryer, G. Fantuzzi, N. Van Rooijen and T. Koh, “Urokinase-Type Plasminogen Activator Plays Essential Roles in Macrophage Chemotaxis and Skeletal Muscle Regeneration,” *J Immunol,* vol. 180, no. 2, pp. 1179-88, 2008.

[32] J. Caster, A. Patel, T. Zhang and A. Wang, “Investigational nanomedicines in 2016: a review of nanotherapeutics currently undergoing clinical trials,” I*nterdiscip Rev Nanomed Nanobiotechnol,* vol. 9, no. 1, p. e1416, 2017.

[33] X. Yang, M. Yang, B. Pang, M. Vara and Y. Xia, “Gold Nanomaterials at Work in Biomedicine,” *Chem Rev,* vol. 115, no. 19, pp. 10410-88, 2015.

[34] S. Perrault, C. Walkey, T. Jennings, H. Fischer and W. Chan, “Mediating Tumor Targeting Efficiency of Nanoparticles Through Design,” *Nano Lett,* vol. 9, no. 5, pp. 1909-15, 2009.

[35] K. Spiller et al., “Sequential delivery of immunomodulatory cytokines to facilitates the M1-to-M2 transition of Macrophages and enhance vascularization of bone scaffolds,” *Biomat,* vol. 37, pp. 194-207, 2015.

[36] D. Kwon et al., “Extra-Large Pore Mesoporous Silica Nanoparticles for Directing in Vivo M2 Macrophage Polarization by Delivering IL-4,” *Nano Lett,* vol. 17, no. 5, pp. 2747-56, 2017.

[37] T. Tran, R. Rastogi, J. Shelke and M. Amiji, “Modulation of Macrophage Functional Polarity towards Anti-Inflammatory Phenotype with Plasmid DNA Delivery in CD44 Targeting Hyaluronic Acid Nanoparticles,” *Sci Rep,* vol. 5, p. 16632, 2015.

[38] T. Hemmerle, F. Doll and D. Neri, “Antibody-based delivery of IL4 to the neovasculature cures mice with arthritis,” *Proc Natl Acad Sci USA,* vol. 111, no. 33, pp. 12008-12, 2014.

[39] P. Chames, M. Van Regenmortel, E. Weiss and D. Baty, “Therapeutic antibodies: successes, limitations and hopes for the future,” *Br J Pharmacol,* vol. 157, no. 2, pp. 220-33, 2009.

[40] C. Borselli et al., “Functional muscle regeneration with combined delivery of angiogenesis and myogenesis factors,” *Proc Natl Acad Sci USA,* vol. 107, no. 8, pp. 3287-92, 2010.

[41] C. Borselli, C. Cezar, D. Shvartsmana, H. Vandenburgh and D. Mooney, "The role of multifunctional delivery scaffold in the ability of cultured myoblasts to promote muscle regeneration," *Biomat,* vol. 32, pp. 8905-14, 2011.

[42] L. Wang et al., "Minimally Invasive Approach to the Repair of Injured Skeletal Muscle With a Shape-memory Scaffold," *Mol Ther,* vol. 22, no. 8, pp. 1441-9, 2014.

[43] V. Horsley, K. Jansen, S. Mills and G. Pavlath, "IL-4 Acts as a Myoblast Recruitment Factor during Mammalian Muscle Growth," *Cell,* vol. 113, no. 4, pp. 483-94, 2003.

[44] A. Chawla, K. Nguyen and Y. Goh, "Macrophage-mediated inflammation in metabolic disease," *Nat Rev Immunol,* vol. 11, no. 11, pp. 738-49, 2011.

[45] C. Cezar et al., "Biologic-free mechanically induced muscle regeneration," *Proc Natl Acad Sci USA,* vol. 113, no. 6, pp. 1534-9, 2016.

[46] F. Faul, E. Erdfelder, A. Lang and A. Buchner, "G*Power3: A flexible statistical power analysis program for the social, behavioral, and biomedical sciences," *Behav Res Meth,* vol. 39, no. 2, pp. 175-91, 2007.

[47] C.D. Walkey, J.B. Olsen, H. Guo, A. Emili and W.C. Chan, "Nanoparticle Size and Surface Chemistry Determine Serum Protein Adsorption and Macrophage Uptake," *JACS,* vol. 134, no. 4, pp. 2139-2147, 2012.

CHAPTER 4:

Combined delivery of VEGF and IGF-1 promotes functional innervation and improves muscle transplantation in mice and rabbits

4.1 Introduction

Reconstructive craniofacial surgery is the standard of care following facial trauma, tumor resection, facial paralysis, and for some genetic disorders such as Mobius syndrome [1, 2], but often results in sub-optimal outcomes. Traditional treatment for facial paralysis includes suture-based face lifts, and sling procedures using fascia and implantable materials, to provide static facial suspension and restore normal anatomic relationships [3]. However no dynamic motion is possible with these approaches. Direct nerve repair by decompression or cross-face grafting is limited to early timepoints after injury. Muscle atrophy associated with chronic facial paralysis necessitates complex reconstructive methods [4]. The current gold standard for facial reanimation following chronic facial paralysis is the microvascular transfer of autologous gracilis muscle to the affected side of the face [5, 6]. However, reinnervation of grafted muscle is unpredictable, and inadequate reinnervation leaves many patients with a poorly functional result [7, 8]. While peripheral motor nerves have the capacity to regenerate following injury [9], surgical repairs result in only 51.6% satisfactory motor recovery [10]. Following peripheral nerve injury Schwann cells produce large amounts of growth factors, such as glial derived neurotrophic factor, and extend processes to guide regenerating axons to denervated motor endplates [11]. However, over time Schwann cells decrease their production of neurotrophic factors and retract their processes [12], resulting in progressive obstacles to axon regrowth into muscle. Despite this, it has been shown in mice and rats that regenerating nerves are able to reach motor end plates and anatomically reform the neuromuscular junction (NMJ) even after extended periods (1 month) of denervation. Despite anatomical regeneration and normal ultrastructural appearance of the NMJ, however, there is a consistent failure to regain synaptic function after prolonged denervation [13].

Muscle transplantation in aged animals often results in poor function due to characteristics of the host microenvironment [14], including changes in tissue-specific stem cells, satellite cells [15], and decline in the neuromuscular system [16]. Satellite cells are believed to be primarily responsible for muscle regeneration [17]. A loss of Notch signaling [18] and disruptions to the self-renewing capacity of satellite cells associated with ageing [19] impair regeneration. IGF-1 plays a central role in maintaining skeletal muscle mass and function with age [20, 21]. Decreased production and activity of the growth hormone/IGF-1 axis with age contributes to limited regenerative capacity [20, 22]. Data from Brigham & Women's Hospital, Boston, show that the age range of patients undergoing face transplants is from 25-59yrs (2015), suggesting it will be important to investigate muscle reinnervation and transplantation in appropriately aged animal models.

Engineering strategies may enable one to provide appropriate cues to damaged skeletal muscle and regenerating motor nerves to improve functional outcomes. Tissue engineering approaches to create functional new muscle typically use a material to promote the assembly of myoblasts in vitro prior to transplantation [23, 24]. While promising, the vascularization, innervation, and ultimately the motor function of the engineered muscle remain significant challenges. In contrast, one may utilize biomaterials that release appropriate morphogens to damaged host tissue to enhance host muscle innervation and function. In addition to its well established role in enhancing vascularization and perfusion [25], vascular endothelial growth factor (VEGF) has also been shown to promote reinnervation following ischemic muscle injury [26]. Upregulation of nerve growth factor and glial-derived neurotrophic factor by sustained, local release of VEGF promoted the maintenance and regrowth of axons into damaged muscle tissue in vivo [26]. Insulin-like growth factor 1 (IGF-1) plays a central role in modulating muscle regeneration. By activating three different signaling pathways, IGF-1 regulates satellite cell activation and myogenic differentiation, protein synthesis, and myofiber survival and hypertrophy [27]. The combined delivery of VEGF and IGF-1 has been shown to simultaneously promote neoangiogenesis, reinnervation,

and muscle stem cell activation following ischemic muscle injury, ultimately resulting in improved muscle regeneration and strength [28].

In this study, we hypothesized that the sustained presentation of VEGF + IGF-1 in damaged and transplanted muscle may significantly improve functional outcomes in both young and aged animals, by preserving undamaged NMJs and promoting axon growth. Alginate hydrogels were used for delivery of these factors, as the concentration gradient of growth factors previously measured in muscle following treatment with these gels [25] mimics that provided by Schwann cells [29] and is expected to provide directional cues to guide motor axon growth into the transplant. These gels are also considered biocompatible, and can be formulated to allow controlled gel degradation and minimally invasive delivery via injection [30, 31, 32, 25, 33]. These gels were previously used to deliver VEGF in murine models of hindlimb ischemia, leading to angiogenesis and restoration of perfusion to levels that could not be achieved via bolus injection of VEGF [25, 34]. These findings contrast with those resulting from bolus VEGF delivery in large clinical trials of ischemia, which have not demonstrated significant benefit. Rapidly depleted local concentrations, inappropriate gradients, high dose requirements and the subsequent off-target effects have all limited bolus delivery strategies [35, 36]. Alginate hydrogel-based delivery of VEGF + IGF-1 was also shown to enhance perfusion in young and aged murine and adult rabbit models of ischemia, while bolus delivery of the factors had only minimal effects on regeneration [28, 37]. Here, a murine model of sciatic nerve injury, with gel injection distal to the injury, was used to assess the ability of alginate delivery to promote functional innervation and improve foot function. This model mimics the nerve ligation and suturing that occurs clinically in microvascular muscle transfer procedures and allowed reinnervation downstream of nerve ligation (i.e down the length of the hindlimb and into the toes) to be investigated both histologically and functionally. To study animals representative of the patient population, both young (6wk) and aged (14wk) mice were used. According to previously published correlations for the progression of neuropathy with age, a 6wk old mouse corresponds to a 4yr old human, and a 14wk old mouse to a 60yr old human [38]. This strategy was also tested in an adult rabbit model of

gracilis muscle transplantation that provides a model of human microvascular craniofacial muscle transfer, and approximates the size of a human graft.

4.2 Materials and Methods

4.2.1 Alginate gel formulation and growth factor incorporation

Ultrapure alginate, 1% oxidized, was provided by the Wyss Institute, Harvard University. Gels were formed from a combination of low and high molecular weight alginate in a 3:1 volume ratio, as previously described [39, 25]. Alginates were reconstituted in EBM-2 (Cambrex) and mixed with recombinant human $VEGF_{165}$ (Peprotech) and/or IGF-1 (Peprotech) to obtain a 2% wt/vol solution before gelation, such that 50uL of gel contains 3μg protein, upon completion. Gels were cross-linked with aqueous slurries of calcium sulfate (0.21g $CaSO_4$/mL alginate) at a ratio of 25:1 (40μL of $CaSO_4$/mL alginate). In vitro release at 37°C into 1% BSA media containing Ca^{2+} ions was measured using ELISA.

4.2.2 Murine Surgical Procedures and Alginate Injection

Animal work was performed in compliance with National Institutes of Health and institutional guidelines. Female C57BL/6J mice (aged 6 or 14wks, Jackson Laboratories) were anesthetized with an i.p. injection of ketamine 80 mg/kg and xylazine 5 mg/kg before surgery. Muscle denervation was induced by unilateral ligation and microvascular neurorrhaphy of the sciatic nerve supplying the right hindlimb. Under a microscope (25-40x magnification), careful dissection of muscle and soft tissues was carried out to expose the sciatic nerve, and at a site 10-12mm from the sciatic foramen, the nerve was transected sharply with microscissors and immediately reapproximated using 12-0 monofilament polyamide epineurial sutures (Ethilon®; Ethicon Ltd., England). Muscles and soft tissues were carefully reapproximated. At this time, 50μL of alginate gel containing 3μg of $VEGF_{165}$ and/or IGF-1, or blank alginate lacking growth factors was injected into muscle tissue surrounding the distal end of the tibialis anterior (TA) muscle. Then the skin was closed using 5-0 polypropylene sutures. To administer booster

injections of alginate, mice were anesthetized with inhaled isoflurane. Booster injections of 50μL alginate were administered between days 20-30 to the same anatomical location as the initial injection via intramuscular (IM) injection through the skin.

4.2.3 Free Gracilis Muscle Transfer and Alginate Injection in Rabbits

Animal work was performed in compliance with National Institutes of Health and institutional guidelines. An autologous gracilis muscle biopsy transferred to a retroauricular location was used as a rabbit model of microvascular craniofacial muscle transplantation, as described previously [40]. Adult female New Zealand rabbits (4 - 4.5 kg) were anesthetized with subcutaneous ketamine (35 mg/kg) and xylazine (5 mg/kg) and maintained with inhalational isoflurane (1-3%). The gracilis muscle was dissected with the associated branch of the obturator nerve and deep femoral vessels. Simultaneously, the recipient site was prepared by dissecting the facial nerves and vessels to expose the neurovascular structures for microvascular anastomosis. Microvascular anastomosis was then performed between the carotid artery and deep femoral artery, facial vein (or external jugular vein) and deep femoral vein; and nerve coaptations performed between the facial nerve and obturator nerve branch, using 9-0 nylon sutures under a standard operating microscope. Muscles, soft tissue, and skin were closed using 4-0 polygalactin-910 and 5-0 polypropylene sutures followed by 2-octyl cyanoacrylate to seal the skin. 5 alginate gels (50μL each), spaced 2cm apart across the length of the 10cm long gracilis transplant were injected at the time of surgery, and booster injections were administered via IM injections every 20-30 days.

4.2.4 COMSOL modeling of VEGF Diffusion

COMSOL Multiphysics was used to model VEGF diffusion and degradation in muscle tissue in order to determine the number and spacing of growth factor-loaded gel injections required to generate and maintain an adequate VEGF tissue concentration (> 5 ng/ml). The equation governing VEGF diffusion and degradation following gel injection is given below,

$$\frac{\partial C}{\partial t} = D_c \nabla^2 C - kC$$

where C = VEGF concentration, D_c = VEGF diffusion coefficient, and k = VEGF degradation rate.

The initial loading concentration and volume of VEGF was 3μg in each 50μL injection of alginate gel. The stipulation that 5ng/mL VEGF in the tissue is required for bioactivity, along with the diffusion coefficient ($7x10^{-7}$ cm^2/s) and degradation constant of VEGF ($1x10^{-5}/s$), were based on previously published experimental data, where the VEGF concentration in mouse muscle tissue was measured over time at various distances from gel injection [25].

4.2.5 Histologic Assessment of Skeletal Muscle

TA muscles were isolated, fixed in 4% PFA, washed, paraffin embedded and stained with H&E. H&E stained cross sections were imaged on a Zeiss Axio Zoom V16 microscope connected to an AxioCam MRm camera, and images were tiled across the entire muscle cross section. Muscle fiber area was assessed by performing color deconvolution in ImageJ. A threashold was applied to the pink (eosin) color channel such that myofibers were included and background excluded. The "analyze particles" function was used to quantify the area within the threashold. The total cross sectional area of the muscle was measured in ImageJ by using freehand selection and the percentage of that cross section falling within the eosin channel was calculated.

4.2.6 Analysis of Anatomic Reinnervation

TA muscles were isolated, fixed in 4% PFA, and embedded in agarose (Lonza #50101). Embedded TAs were sectioned on a vibratome, 100-200μm thick. Sections were stained with Alexa594-bungarotoxin (1/500 dilution, Invitrogen B-13423) to visualize acetylcholine receptors of motor end plates and anti-200kDa neurofilament heavy Ab (1/500 dilution, #ab8135) to visualize nerve filaments. Stained sections were mounted on glass slides and visualized on an upright Zeiss LSM 710 NLO ready

confocal microscope. Colocalization of motor end plates and nerve filaments in the x, y, and z directions indicated structural innervations.

4.2.7 Muscle Force Testing in Mice

Ex vivo muscle strength and contraction velocity were tested as described previously [39]. Intact TA muscles were dissected, and immediately mounted vertically midway between two cylindrical parallel steel wire electrodes (1.6 mm diameter, 21 mm long) by attaching their tendons to microclips connected to a force transducer (FORT 25, WPII). Muscles were bathed in physiologic saline solution in a chamber with continuously bubbled oxygen at 37°C, and the muscle was adjusted to a physiologically relevant length. A wave pulse was initiated using a custom-written LabVIEW program and delivered to the stimulation electrodes via a purpose built power amplifier (QSC USA 1310). Tetanic contractions were evoked at 250 and 270 Hz, and 25 and 27 V, respectively, with a constant pulse width of 2ms and a train duration of 1s. The muscle was allowed to rest for 5min between each stimulation. Contraction force was determined as the difference between the maximum force during contraction and the baseline level and normalized by muscle wet weight. Contraction velocity was determined as the slope of the force curve at the time electrical stimulation was initiated.

4.2.8 Toe Spreading and Sciatic Nerve Function in Mice

Animal imaging and functional studies were performed in compliance with National Institutes of Health and institutional guidelines. Functional recovery was assessed serially (on day 1, and every 10 days) by using imaging of the plantar aspect of the hind feet during occasional rest periods in a clear plastic-bottomed corridor, based on [41]. The clear plastic corridor was suspended between 2 cages to allow a webcam, connected to a laptop, to be placed directly under the mouse for imaging. Each mouse was imaged until at least 5 images meeting the following criteria were obtained: mouse was in a static position, both hind feet and at least 1 of the front feet were flat on the corridor, all 5 toes of each hind foot were clearly visible. ImageJ was used to measure the spread between digits 1-5 (TS), and 2-4 (ITS) on

each hind foot to calculate TSF and ITSF according to the formulas: TSF = ($TS_{injured}$ - $TS_{uninjured}$)/$TS_{uninjured}$; ITSF = ($ITS_{injured}$ - $ITS_{uninjured}$)/$ITS_{uninjured}$. The static sciatic index (SSI) was calculated with the following formula: SSI = (108.44 x TSF) + (31.85 x ITSF) – 5.49 [41]. At least 5 images of each animal were analyzed by a blinded researcher.

4.2.9 Statistical Analysis

All analyses were performed on GraphPad Prism5. ANOVA with Tukey or Bonferroni post hoc tests were used, and differences were considered significant at $P < 0.05$.

A power analysis was performed on GPower3.1 [42] based on anatomic innervation data from young mice following treatment at the time of surgery with either blank or VEGF + IGF-1 alginate. The power analysis accounted for 1 independent output variable, and 4 equally sized experimental groups, with an $\alpha = 0.05$. Assuming a difference of 10 percentage points between the negative control and most effective treatment, the analysis yielded that n=15/group will provide 80% power.

4.3 Results

4.3.1 Establishment of the mouse model and appropriate analysis for recovery

A mouse model of denervation by unilateral ligation and microvascular neurorrhaphy of the sciatic nerve supplying the right foot and tibialis anterior (TA) muscle was first used to examine the impact of gel delivery of growth factors on muscle innervation. A series of trial studies with small sample sizes were initially performed to determine the relationship between histological and functional analysis of innervation in this model, and to determine variability in order to appropriately power subsequent definitive experiments. NMJs were stained for α-bungarotoxin (that binds to the nicotinic AChR of motor end plates) and for neurofilament (heavy polypeptide in nerve axons, ab8135), and morphological establishment of the NMJ was assessed by colocalization of α-bungarotoxin with neurofilament, as imaged on a confocal microscope. Analysis of motor end plates and nerves in the TA showed that by 1

day after surgery in young (6wk old) mice, significant nerve regression resulted in only 14% of motor end plates demonstrating contact with nerve filaments (Fig. 4.1), confirming the impact of the procedure on hindlimb innervation. By day 60 after surgery, however, the majority (78%) of motor end plates in untreated mice had structurally regained contact with regenerated nerve filaments (Fig. 4.1 F). Mice were subsequently treated at the time of surgery with an intramuscular (IM) injection, at the distal end of the hindlimb, adjacent to the TA muscle, of a degradable [28] alginate gel (Fig. 4.2 A) with no factors, or gels releasing VEGF + IGF-1. VEGF is released slowly over the course of 30 days, while IGF-1 is released more quickly, in vitro [28]. This sustained release of VEGF + IGF-1 is expected to yield a concentration gradient of growth factors, with increasing concentration towards the distal end of the hindlimb (Fig. 4.2 B), as previously validated experimentally in a similar model [25]. TA histology was assessed in these young mice following treatment. No significant differences in morphological innervations were observed between the blank alginate and VEGF + IGF-1 alginate treated groups, as 42% of motor end plates were contacted by neurofilaments on day 20 after surgery, and 68% and 78% were innervated in the blank and VEGF + IGF-1 treated groups on day 50, respectively (Fig. 4.2 C-D).

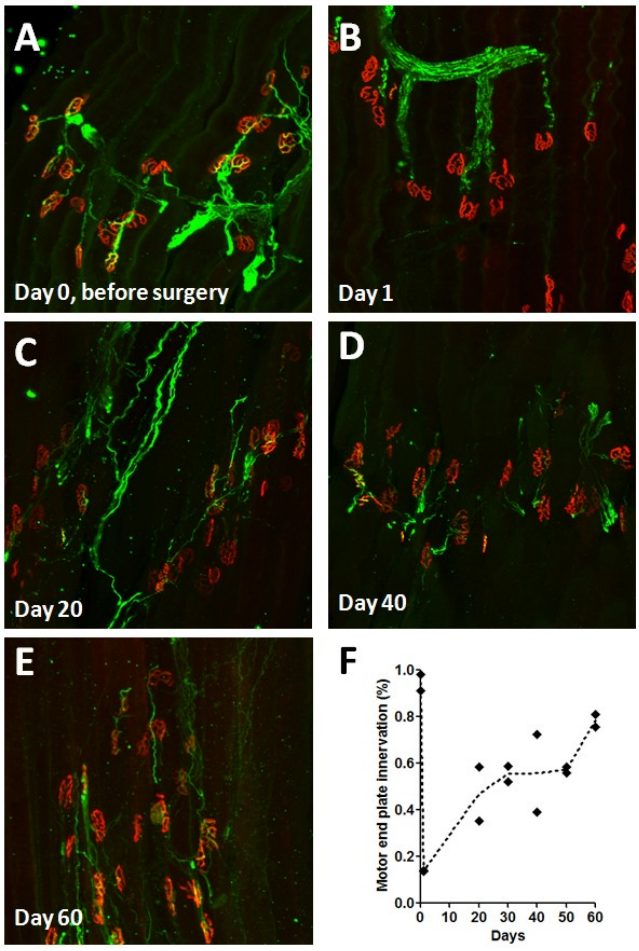


Figure 4.1. Spontaneous recovery of anatomic innervations in the TA following sciatic nerve ligation and microvascular neurorrhaphy. (A-E) Representative confocal maximum intensity projections of NMJs in the TA before surgery (A), and on d1 (B), d20 (C), d40 (D), and d60 (E) after surgery in young (6wk) mice without any treatment. Bungarotoxin staining of MEPs is shown in red and nerve filaments in green. (F) Quantification of anatomic innervations, defined as the percentage of motor end plates colocalized with nerve filaments. Mean of 2 mice is shown by the dotted line (n=2). At least 25 MEPs were analyzed for each animal, with an average of 56 analyzed per animal.

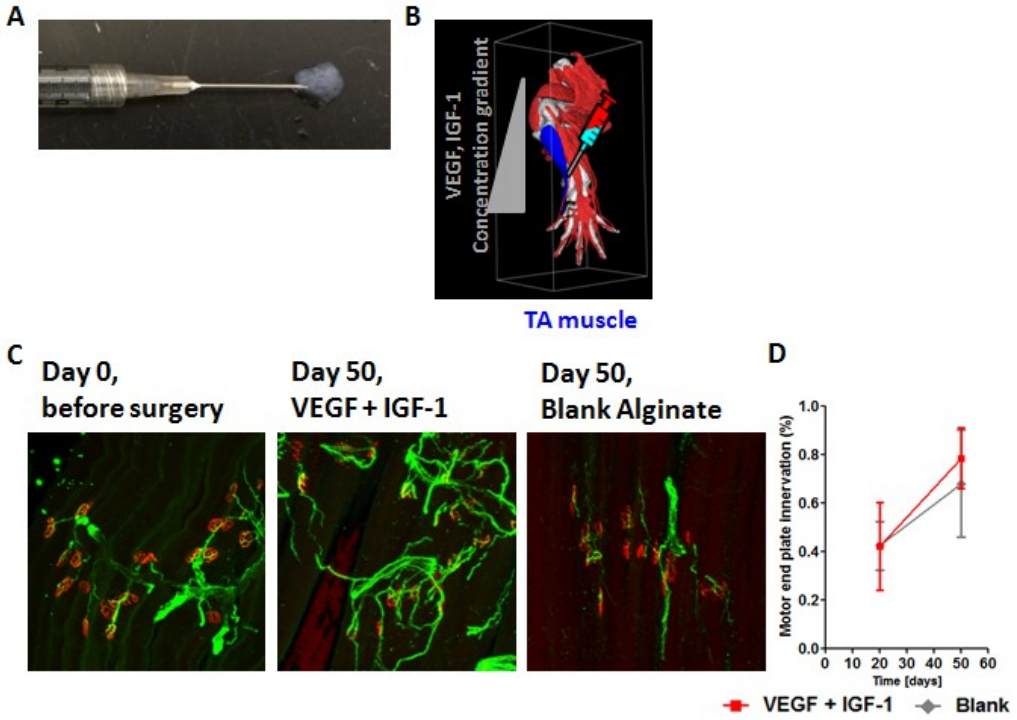


Figure 4.2. Sustained release of VEGF and IGF-1 from alginate hydrogels creates a concentration gradient in the murine hindlimb. (A) Alginate gel being injected through a 27 gauge needle. (B) Model of the murine hindlimb showing injection of the gel at the distal end of the limb into muscle adjacent to the TA, and the resultant concentration gradient of VEGF and IGF-1. (C) Confocal maximum intensity projections of NMJs in the TA before surgery and on day 50 after surgery and treatment with blank or VEGF + IGF-1 alginate in young mice. Bungarotoxin staining of MEPs is shown in red and nerve filaments in green. (D) Quantification of anatomic innervations, defined as the percentage of MEPs colocalized with nerve filaments. Values are mean ±SD, n=6 (day 20), n=7 (day 50); no statistically significant differences were observed.

Functional innervation throughout the length of the hindlimb was next assessed by measuring the extent to which the mice could spread their toes between the first and fifth digits (toe spreading, TS), and the second and fourth digits (intermediary toe spreading, ITS) (Fig. 4.3 A). This analysis was done by an investigator blinded to the treatments. Both of these measurements were normalized by toe spreading in the uninjured contralateral foot to give the toe spreading factor (TSF) and the intermediary toe spreading factor (ITSF); TSF and ITSF were used to calculate a composite index commonly used to assess sciatic nerve function, the static sciatic index (SSI) [43, 41]. Mice treated with VEGF + IGF-1 alginate maintained a consistent TSF through day 50, while those treated with blank alginate demonstrated

continual loss of toe spreading function (Fig. 4.4). However, due to the broad variability in toe spreading between individual mice, this trend was not statistically significant (n=6).

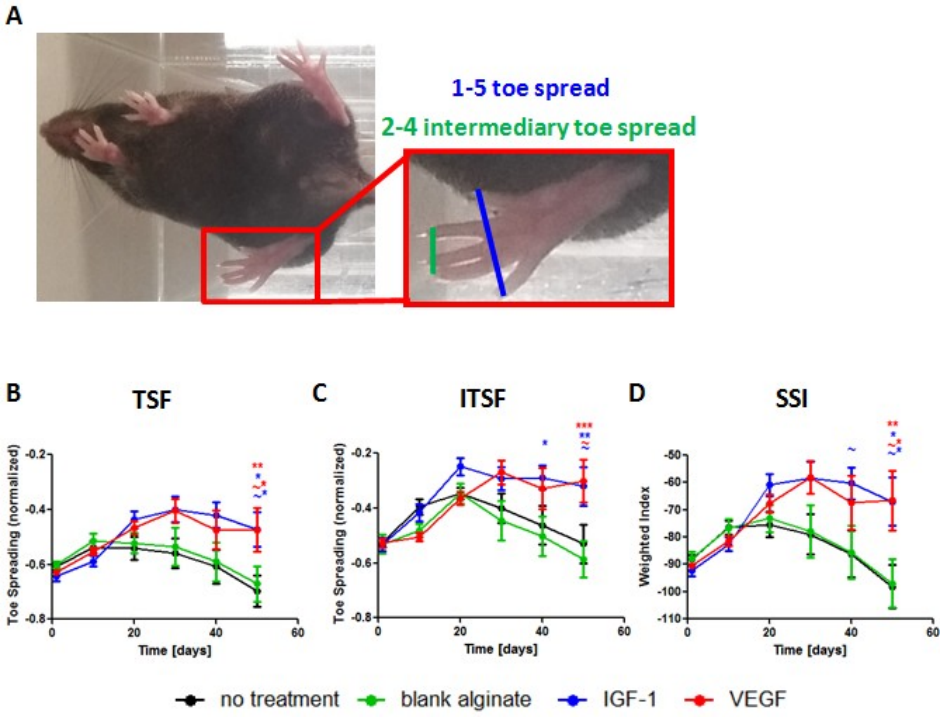


Figure 4.3. Sustained VEGF or IGF-1 presentation enhance functional toe spreading in young mice. (A) View from below the mouse used to assess functional toe spreading between digits 1-5 and 2-4. (B) Assessment of functional toe spreading using TSF through day 50 following treatment with VEGF, IGF-1 or blank alginate, or no treatment at the time of surgery. A TSF=0 implies no impairment, TSF=-1 indicates total loss of function with no toe spreading. (C) Assessment of functional toe spreading using ITSF. An ITSF=0 implies no impairment, ITSF=-1 indicates total loss of function with no toe spreading. (D) Assessment of sciatic nerve function using SSI, calculated from the TSF and ITSF for each mouse. SSI $\geq$ -5.49 indicates no impairment, SSI $\leq$ -145, complete loss of function. For TSF, ITSF, and SSI plots (B-D), values are mean ±SEM, n=15. * $p<0.05$, ** $p<0.01$, *** $p<0.001$ vs blank alginate; ~$p<0.05$, ~*$p<0.01$ vs no treatment, matched 2-way ANOVA with Bonferroni post-test.

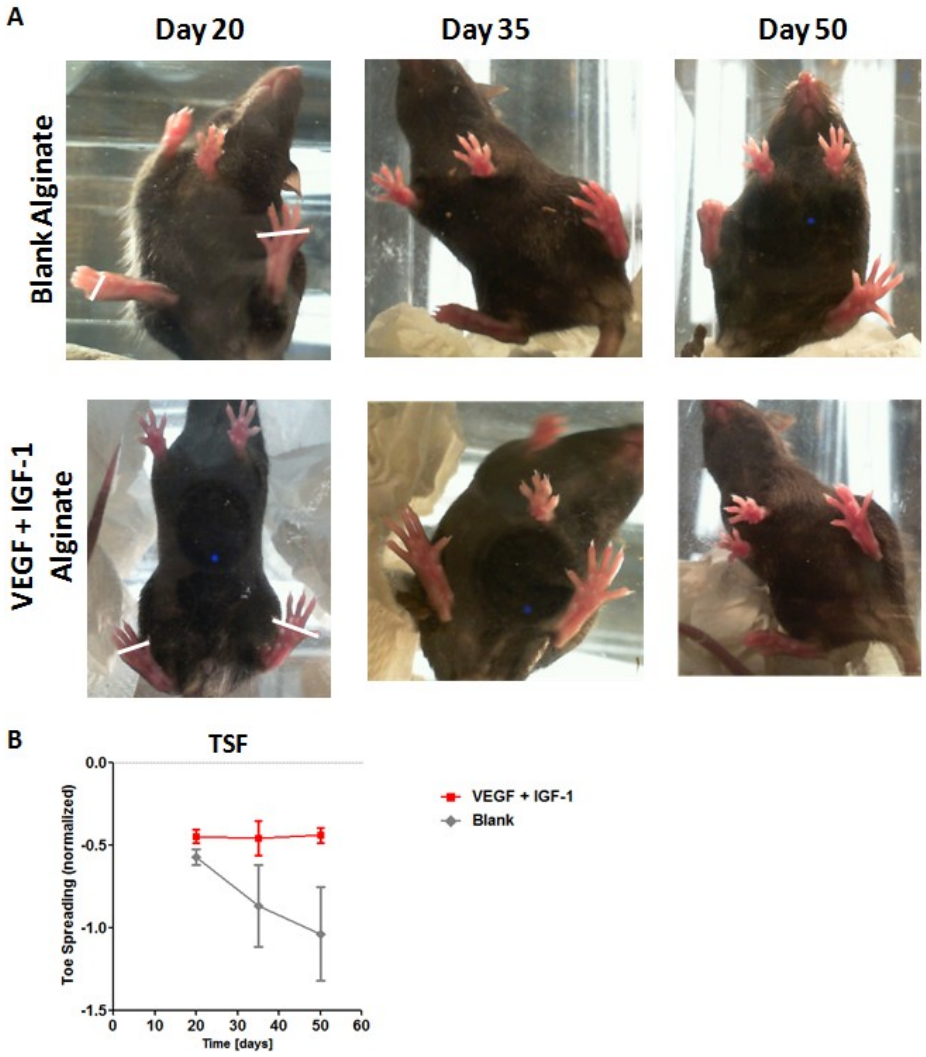


Figure 4.4. Alginate delivery of VEGF + IGF-1 may improve functional toe spreading in young mice. (A) Representative images of the plantar aspect of the feet used to quantify toe spread in the injured (shown on the left) and contralateral (shown on the right) hind feet following treatment at the time of surgery with blank or VEGF + IGF-1 alginate. (B) Assessment of functional toe spreading using TSF through day 50, following treatment with VEGF + IGF-1 or blank alginate at the time of surgery. A TSF = 0 implies no impairment, TSF = -1 indicates total loss of function with no toe spreading. Values are mean ±SEM, n=6. No statistically significant differences were identified with a 2-way ANOVA with Bonferroni post-test.

Altogether these data suggest that apparent histological contact between neurofilaments and motor end plates does not correlate well with synaptic function, which is consistent with a previous report [13]. Given the spontaneous recovery of anatomic NMJ connections without treatment, and the lack of a

clear correlation between structural connections and function, subsequent experiments focused on recovery of nerve function and muscle contractility as more relevant metrics for the impact of treatment. Further, based on the results of the preliminary study, a power analysis was performed and subsequent murine studies were fully powered with n=15.

4.3.2 Sustained VEGF or IGF-1 presentation enhances functional recovery in young mice

Alginate gels delivering either VEGF or IGF-1 alone were next analyzed in comparison to blank alginate or no treatment in young mice in order to analyze the impact of delivery of each factor (n=15). Immediately following surgery, TSF, ITSF, and SSI declined, and then a period of functional recovery was observed in all groups regardless of whether treatment was administered. Gel delivery of either VEGF or IGF-1 however, resulted in a prolonged period of recovery following surgery, ultimately resulting in statistically significant improvements in TSF, ITSF, and SSI by day 50 after surgery (Fig. 4.3 B-D) as compared to the negative control groups. After day 50, however, mice in all treatment groups exhibited a decline in toe spreading function at approximately the same rate (Fig. 4.5).

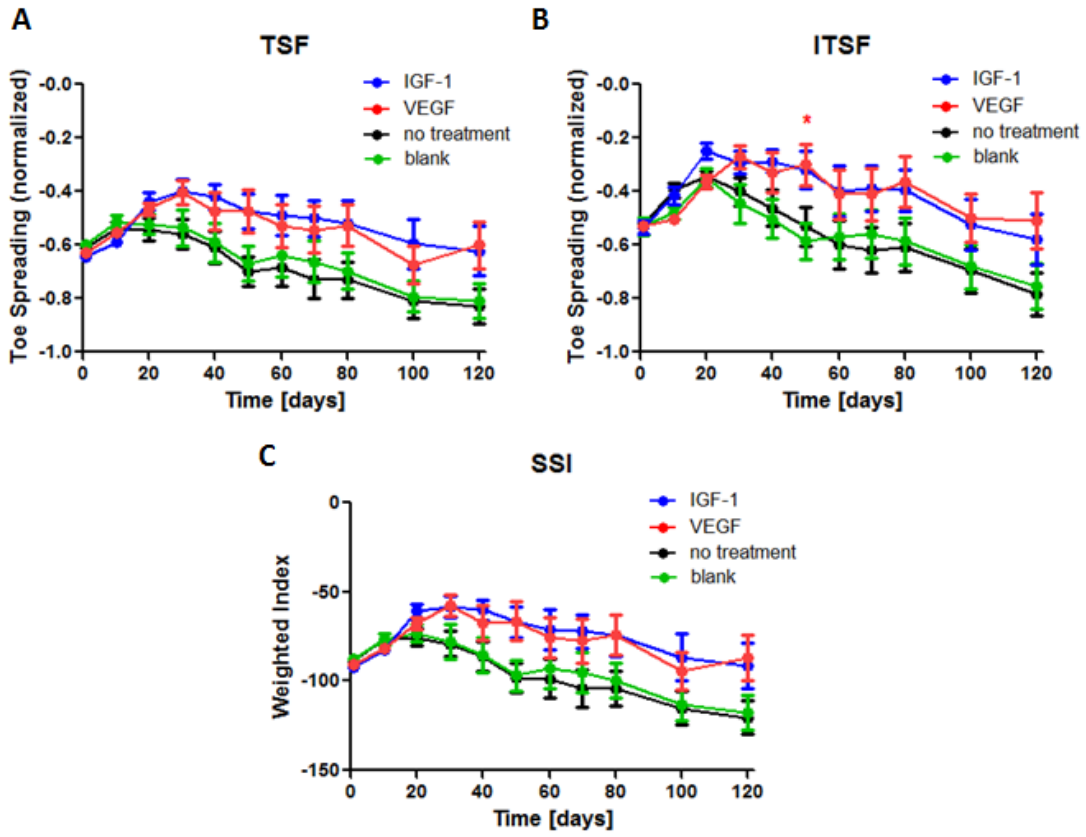


Figure 4.5. After an initial period of improvement, functional toe spreading in young mice declines following a single VEGF or IGF-1 alginate injection at the time of surgery. (A) Assessment of functional toe spreading using TSF (A) and ITSF (B) through day 120 following a single treatment at the time of surgery with blank, VEGF, or IGF-1 alginate, or no treatment. I/TSF = 0 implies no impairment, I/TSF = -1 indicates total loss of function with no toe spreading. (C) Assessment of sciatic nerve function using SSI, calculated from the TSF and ITSF for each mouse. SSI $\geq$ -5.49 indicates no impairment, SSI $\leq$ -145, complete loss of function. Values are mean ±SEM, n=15. No statistically significant differences were identified with a matched 2-way ANOVA with Bonferroni post-test.

To determine if a second injection of VEGF or IGF-1 alginate would prolong the period of functional improvement following injury, a booster injection of VEGF or IGF-1 alginate was administered at the distal end of the hindlimb, adjacent to the TA muscle, between days 20-30 after surgery (Fig. 4.6 A). Approximately 90% of the mice that received a booster injection of VEGF alginate between days 20-30 showed improvement in TSF and SSI (Fig. 4.6 B,D) between those time points. In contrast, only about half of the mice that initially received VEGF alginate but no second treatment

showed improved toe spreading between days 20-30. IGF-1 alone was not as effective as VEGF at enhancing toe function. Mice in all treatment groups had diminished TA mass at day 85 in the injured, as compared to the contralateral muscle at this time point (Fig. 4.7). TAs from all groups demonstrated normal H&E histological muscle architecture, indicating that the alginate gels did not have any local negative effects on the tissue (Fig. 4.8). Further, both TA contraction force and velocity (Fig. 4.6 E-F) showed significant improvements in mice that had received a booster injection of IGF-1 alginate. There was a 35% and 45% increase in contraction force and velocity, respectively, in mice that had received a booster injection of IGF-1 alginate as compared to mice that only received the initial injection. VEGF was also effective at promoting functional muscle regeneration, but not to the same extent as IGF-1.

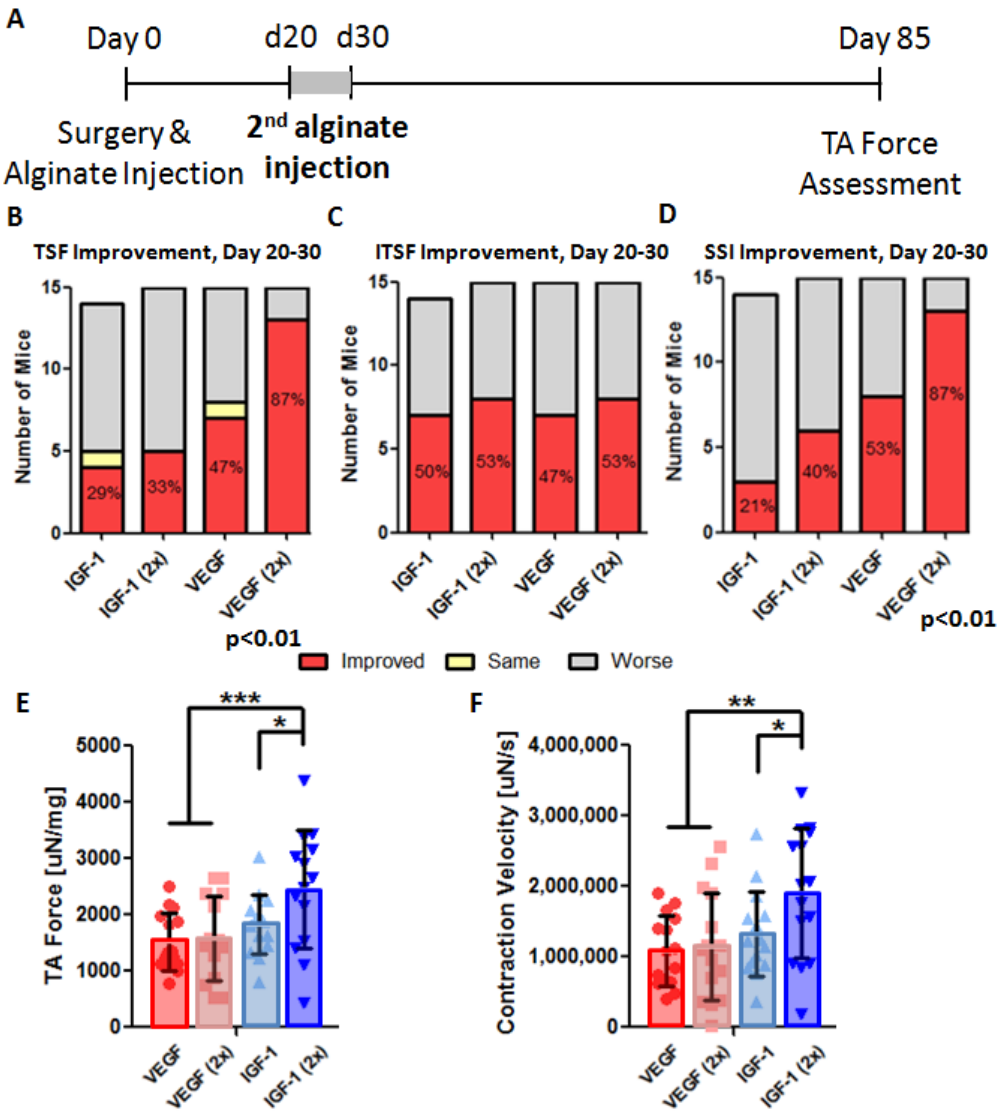


Figure 4.6. Toe spreading and muscle function are improved following administration of a booster injection of VEGF and IGF-1 alginate, respectively. (A) Alginate gels were injected IM adjacent to the distal end of the TA at the time of surgery, and again between days 20-30 in young mice. Mice were tracked and toe spreading was assessed before and after administration of the booster injection (i.e. on days 20 and 30); mice were sacrificed and muscle function assessed on day 85. (B-D) Functional improvement following administration of a booster injection was assessed by quantifying the percentage of mice that showed improvement (red), no change (yellow), or decline (gray) in TSF (B), ITSF (C), and SSI (D) between days 20-30. n=15 for IGF-1 single injection, n=16 for IGF-1 booster, and VEGF groups. $p<0.01$ for TSF and SSI, Chi-square test considering 2 outcomes improved (red) vs "same or worse" (yellow and gray). (E-F) TA function was assessed by maximum contraction force (E) and velocity (F) of explanted TAs stimulated at 25V, 250Hz on day 85 after surgery. Force was normalized to TA weight. Values are mean ±SD, n=15. *$p<0.05$, **$p<0.01$, ***$p<0.001$, 2-way ANOVA with Bonferroni post-test. Data from the contralateral TA has been excluded from the plots.

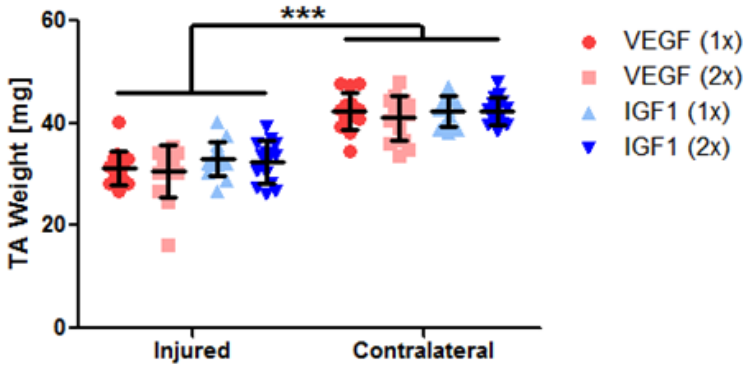


Figure 4.7. TA weight is reduced in the injured limb on day 85 after surgery in young mice following treatment with a single injection of VEGF or IGF-1 alginate at the time of surgery or booster injections of alginate administered at the time of surgery and between days 20-30. Values are mean ±SD, n=14-15. Matched 2-way ANOVA with Bonferroni post-test.

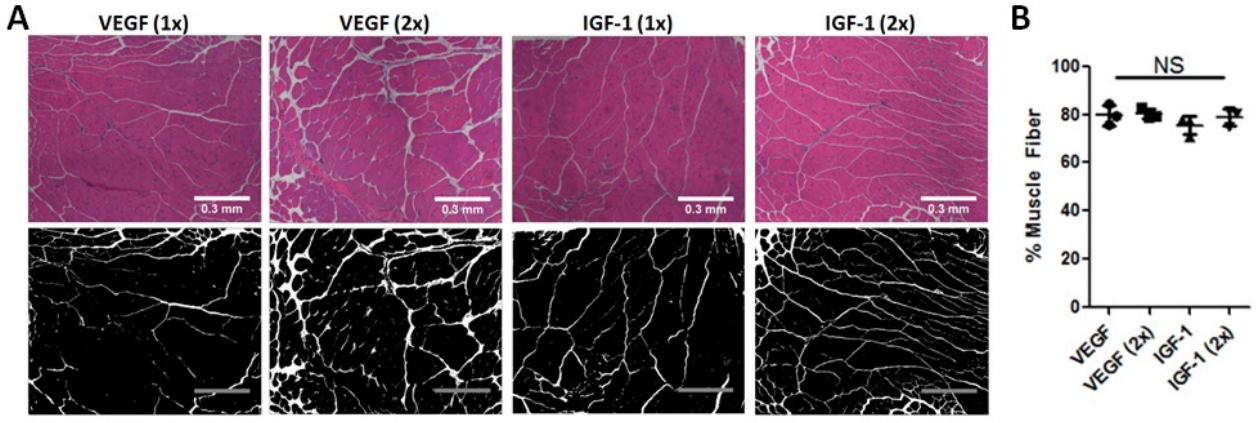


Figure 4.8. Delivery of VEGF or IGF-1 does not significantly improve muscle fiber area following sciatic nerve injury in young mice. (A) H&E histology from the middle of the TA, at the physiological cross-section, in young (6wk) mice on day 85 after surgery/initial treatment and booster alginate injection between days 20-30 (in groups noted with 2x). (bottom) Muscle fiber area was identified following color deconvolution in ImageJ and thresholding in the eosin channel. (B) Muscle fiber regeneration was assessed by measuring the muscle fiber area as a percentage of the TA cross-section. Values are mean ±SD, n=3. No statistically significant differences were identified with a 1-way ANOVA with Tukey post-test.

4.3.3 Combined delivery of VEGF + IGF-1 results in improved function in aged mice

Next, to study the effects of alginate delivery of VEGF and/or IGF-1 on therapeutic improvements in mice more representative of the older patient population that typically undergoes muscle transplant procedures, unilateral sciatic nerve ligation and microvascular neurorrhaphy was performed on 14wk old mice. Based on previous reports that older mice require a combination of VEGF and IGF-1 to show functional benefit in the context of angiogenesis [37], the combined delivery of both factors was included in this study with aged mice. Unlike young mice, only 20-40% of mice treated with blank alginate showed improvements in TSF and SSI between days 1-10 after surgery. However injection of IGF-1, VEGF, or VEGF + IGF-1 alginate at the time of surgery led to 70-80% of mice demonstrating improvements in TSF and SSI between days 1-10 (Fig. 4.9 A-C). Based on the benefit in young mice following booster injections, aged mice also received a booster injection of VEGF and/or IGF-1 alginate between days 20-30. Over time, while delivery of VEGF or IGF-1 alone maintained toe spreading function for a longer duration following surgery than blank alginate, only combined delivery of VEGF + IGF-1 resulted in improved TSF, ITSF, and SSI on day 40 (Fig. 4.9 D-F). While a benefit of growth factor delivery remained after approximately day 40, mice in all treatment groups showed a loss in toe spreading function at approximately the same rate after this timepoint (Fig. 4.10), suggesting that administration of booster injections every 20-30 days may be required until full functional recovery is achieved.

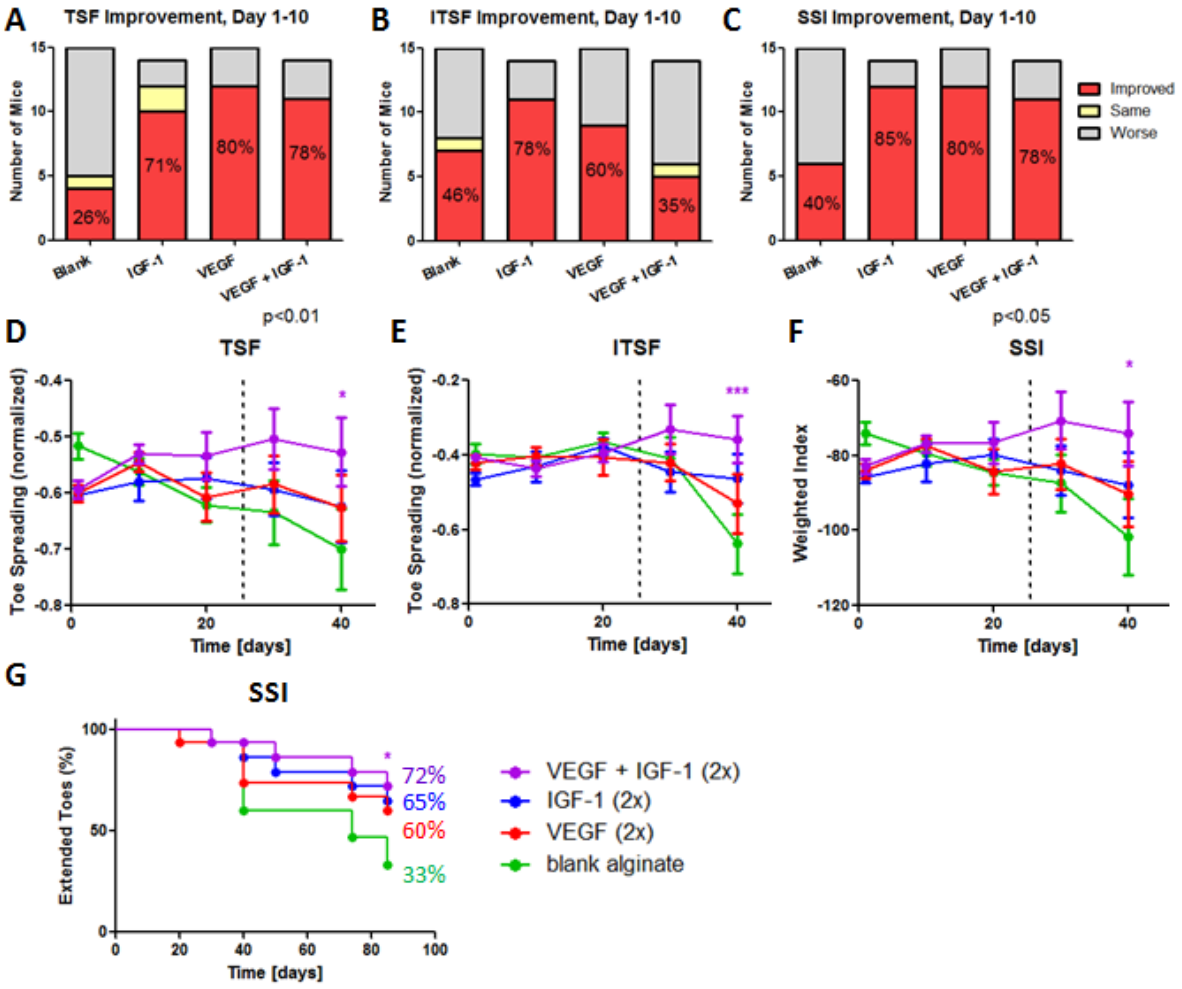


Figure 4.9. Combined presentation of VEGF and IGF-1 to aged mice results in improved toe spreading and sciatic nerve synapse function. (A-C) Initial functional improvement following surgery and injection of blank, VEGF, IGF-1, or VEGF + IGF-1 alginate in aged mice was assessed by quantifying the percentage that showed improvement (red), no change (yellow), or decline (gray) in TSF (A), ITSF (B), or SSI (C) between days 1-10. n=14-15. $p<0.01$ for TSF, $p<0.05$ for SSI, Chi-square test considering 2 outcomes improved (red) vs "same or worse" (yellow and gray) (D-E) Assessment of functional toe spreading using TSF (D) and ITSF (E) through day 40 following treatment with blank, VEGF, IGF-1 or VEGF + IGF-1 alginate at the time of surgery and again between days 20-30. I/TSF=0 implies no impairment, I/TSF=-1 indicates total loss of function with no toe spreading. (F) Assessment of sciatic nerve function using SSI. SSI $\geq$ -5.49 indicates no impairment, SSI $\leq$ -145, complete loss of function. For TSF, ITSF, and SSI plots (D-F), values are mean ±SEM, n=14-15. * $p<0.05$, *** $p<0.001$ vs blank alginate; matched 2-way ANOVA with Bonferroni post-test. (G) Permanent loss of nerve synapse and toe function was indicated by SSI < -125. The percentage of mice that maintained function was plotted with a Kaplan-Meier curve. n=14-15. *$p<0.05$ Mantel-Cox single comparison vs. blank

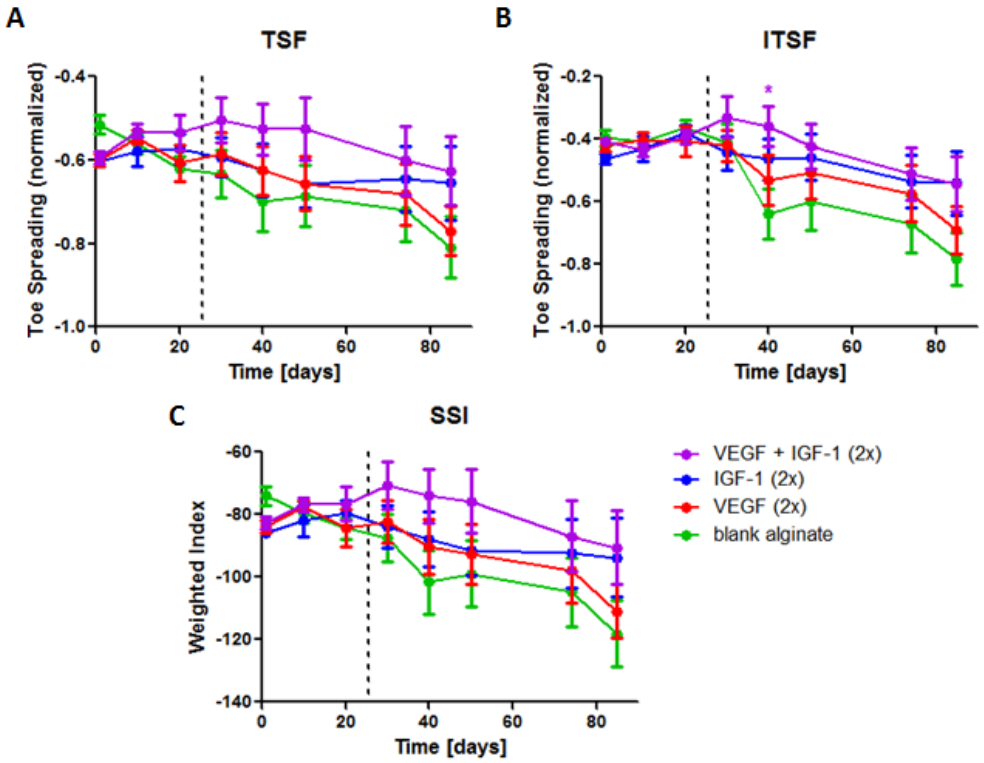


Figure 4.10. VEGF + IGF-1 Alginate improves functional toe spreading in aged mice, through 20-30 days following injection. (A) Assessment of functional toe spreading using TSF (A) and ITSF (B) through day 85 following treatment at the time of surgery and again between days 20-30 with blank, VEGF, IGF-1, or VEGF + IGF-1 alginate. I/TSF = 0 implies no impairment, I/TSF = -1 indicates total loss of function with no toe spreading. (C) Assessment of sciatic nerve function using SSI, calculated from the TSF and ITSF for each mouse. SSI $\geq$ -5.49 indicates no impairment, SSI $\leq$ -145, complete loss of function. Values are mean ±SEM, n=14-15. * $p<0.05$, matched 2-way ANOVA with Bonferroni post-test.

Mice losing the ability to spread or even extend their toes indicates a severe loss of innervation; the toes drag on the ground as mice walk in this situation, giving the appearance of being in a fist (Fig. 4.11). Tracking of individual mice, as versus average behavior of a cohort, revealed that once a specific level of loss in toe spreading function occurred in a mouse, that mouse never showed recovery. For the SSI this occurred below a score of -125 (Appendix C, Fig. C1), and for TSF and ITSF this occurred at -0.85 (Appendix C, Figs. C2, C3). Using these scores as a metric of severe and irreversible nerve damage, the percentage of mice in this state were tracked using Kaplan-Meier curves. VEGF + IGF-1 alginate significantly prolonged toe function following injury in aged mice as assessed by these cut-off values for

SSI, TSF, and ITSF (Fig. 4.9 G; Appendix C, Fig. C4). This benefit was observed over the course of 85 days post surgery, despite the fact that only 1 booster injection of alginate was administered between days 20-30.

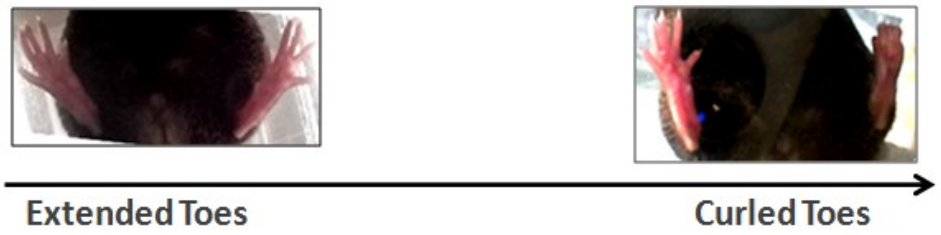


Figure 4.11. Representative images of the plantar aspect of the hind feet showing normal toe spread (left) and complete loss of toe function (curled toes, right). When toe function is lost the toes form a fist and drag on the ground as the mouse walks. The injured limb is shown on the right in the image.

At the completion of the studies (day 85), muscle mass and function were assessed. The TA mass was still diminished in the injured, as compared to the contralateral TA at this timepoint in all mice (Fig. 4.12). As a metric of muscle regeneration, the percentage of the TA cross sectional area composed of myofibers was quantified (Fig. 4.13 A-B). Alginate delivery of either VEGF or IGF-1 increased the percent myofiber area as compared to muscles treated with blank alginate. Combined delivery of VEGF + IGF-1, however, resulted in the most significant increase in myofiber area. Consistent with the data from young mice, IGF-1 alginate treatment significantly increased TA contraction force and velocity (Fig. 4.13 C-D). However, combined delivery of VEGF + IGF-1 resulted in the most significant improvements in contraction force and velocity, yielding 2.8 and 3.0-fold increases, respectively, as compared to mice treated with blank alginate.

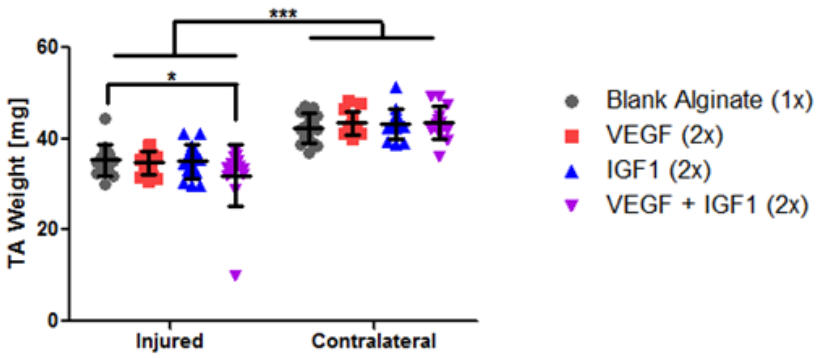


Figure 4.12. TA weight is reduced in the injured limb on day 85 after surgery in aged (14wk) mice. Mice were treated with blank, VEGF, IGF-1, or VEGF + IGF-1 alginate at the time of surgery, and growth factor containing alginate was injected again between days 20-30. Values are mean ±SD, n=14-15. *p<0.05, ***p<0.001 2-way ANOVA with Bonferroni post-test.

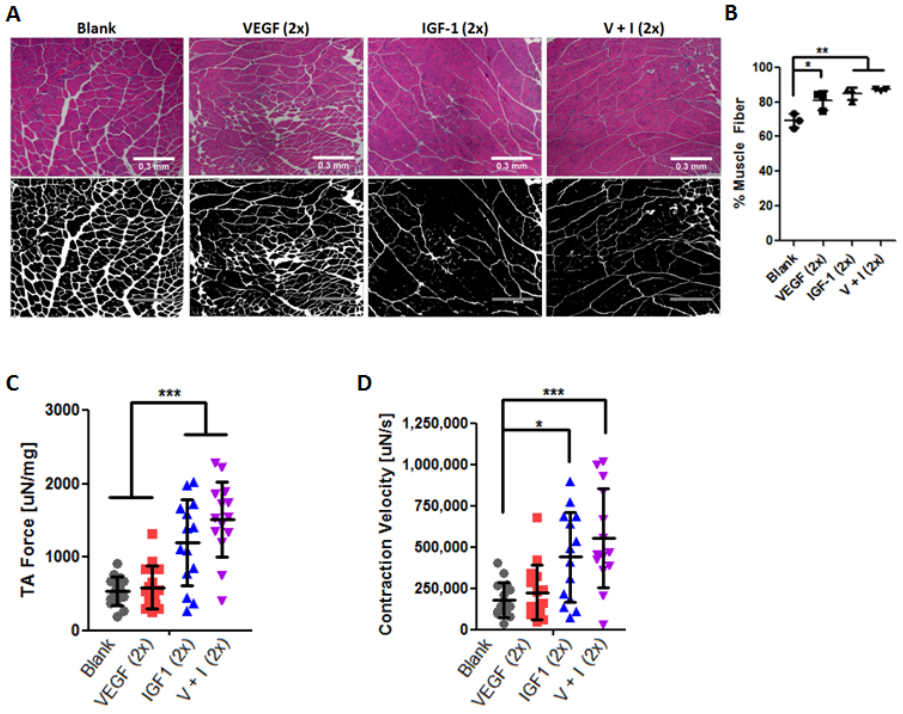


Figure 4.13. VEGF + IGF-1 alginate improves muscle fiber area, TA contraction force and velocity in aged mice. (A) (top) H&E histology from the middle of the TA, at the physiological cross-section, in aged (14wk) mice on day 85 after surgery/initial treatment and booster alginate injection between days 20-30. (bottom) Color deconvolution and thresholding of the eosin channel performed in ImageJ used to quantify muscle fiber area. (B) Muscle fiber regeneration was assessed by measuring the muscle fiber area as a percentage of the TA cross-section. Values are mean ±SD, n=3. *p<0.05, **p<0.01, 1-way ANOVA with Tukey post-test. (C-D) TA function was assessed by measuring maximum contraction force (C) and velocity (D) of explanted TAs stimulated at 27V, 270Hz on day 85 after surgery. Force was normalized to TA weight. Values are mean ±SD, n=14-15. *p<0.05, ***p<0.001, 2-way ANOVA with Bonferroni post-test. Data from the contralateral TA has been excluded from the plots.

4.3.4 Combined delivery of VEGF + IGF-1 improves functional muscle innervation following transplantation in rabbits

Finally, to determine if alginate delivery of VEGF + IGF-1 improves the recovery of nerve function in a transplanted muscle that models the size of a human graft, a rabbit model of microvascular craniofacial muscle transfer was used. An autologous gracilis muscle biopsy was transferred to a retroauricular location (Fig. 4.14 A), and alginate was injected into the transplanted gracilis prior to transplantation. To determine the appropriate number and spacing of gel injections as the muscle size increased from the mouse to rabbit, a COMSOL Multiphysics model was used to model VEGF diffusion and degradation in muscle tissue, as previously demonstrated [37, 25]. This modeling predicted that a single gel injection (50 μl) would maintain the VEGF concentration at a bioactive concentration in a tissue volume of ~1cm radius. Thus, 5 gel injections, equally-spaced (2cm apart) across the length of the ~2.4cm diameter x 10cm long gracilis transplant, were utilized in these rabbit studies (Fig. 4.14 B).

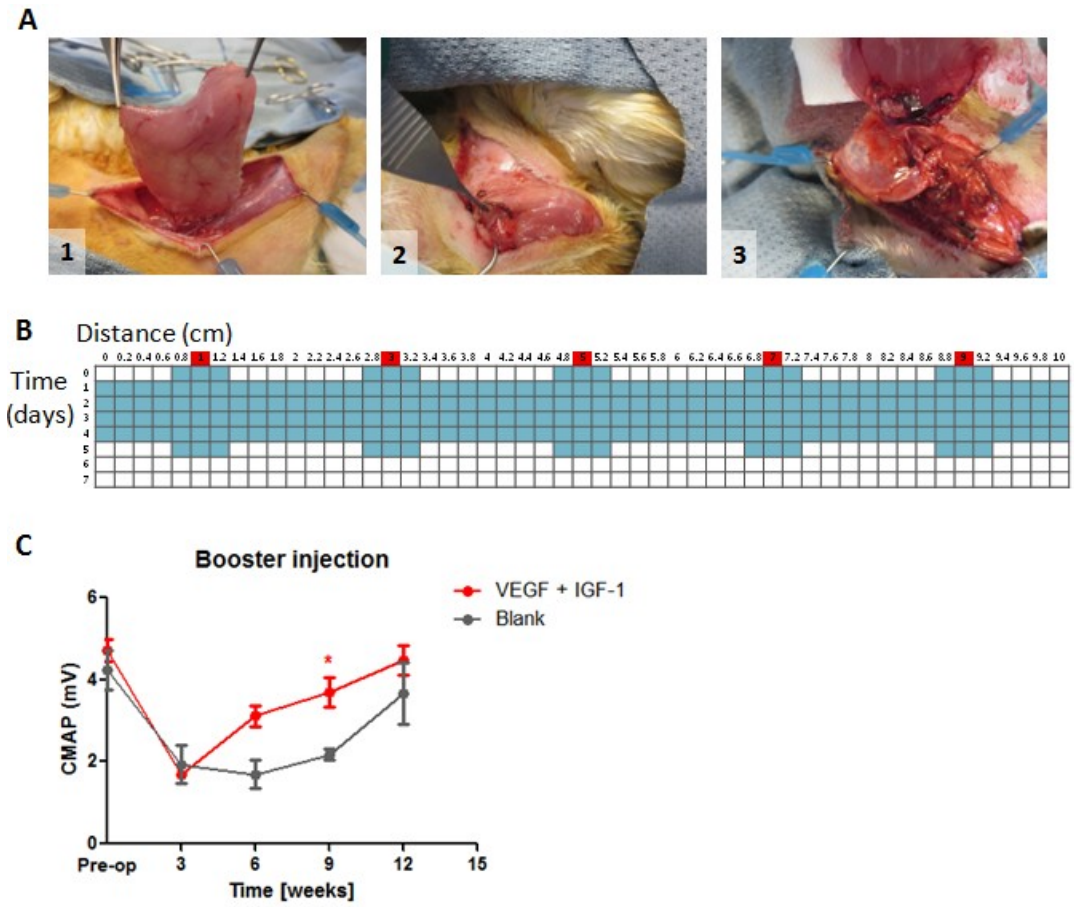


Figure 4.14. Combined delivery of VEGF and IGF-1 improves muscle nerve function following muscle transfer in a rabbit. (A) 1. The gracilis muscle flap is isolated with the pedicle, femoral artery, vein, and obturator nerve. 2. The facial nerve is isolated. 3. The gracilis muscle is attached to a branch of the facial nerve. The left jugular vein is later anatomized with the femoral vein. (B) Image from COMSOL indicating the alginate injection locations (red boxes), and region of biologically active VEGF concentration (i.e. > 5ng/mL, blue boxes) over time (y-axis) through the length of the muscle (x-axis). (C) Function of the transplanted gracilis was assessed by using electromyography to measure CMAP every 3wks following muscle transfer and treatment every 20-30 days with VEGF + IGF-1 alginate or blank alginate. Values are mean ±SEM, VEGF + IGF-1 n=6, blank n=3. *$p<0.05$, matched 2-way ANOVA with Bonferroni post-test.

Following transplantation, functional innervation throughout the transplanted muscle was assessed using electromyography to measure compound muscle action potential (CMAP). Following surgery, all rabbits demonstrated a 60% decrease in CMAP in the transplanted gracilis (Fig. 4.14 C). When only a single injection of VEGF, IGF-1, or VEGF + IGF-1 alginate was administered to the

transplant, CMAP readings showed minimal improvement only through ~4wks, then maintained a low CMAP through the end of the study (24wks) (Fig. 4.15). In subsequent studies, booster injections of growth factor containing alginate were administered every 20-30 days. Transplants treated with VEGF + IGF-1 alginate booster injections showed continual improvements in CMAP starting at 3wks (Fig. 4.14 C), resulting in 83% and 71% increases in CMAP at 6 and 9wks, respectively, compared to blank alginate treatment. Eventually, the untreated grafts demonstrated spontaneous recovery, as expected, and by 12wks the transplants in both treatment groups showed comparable CMAP readings.

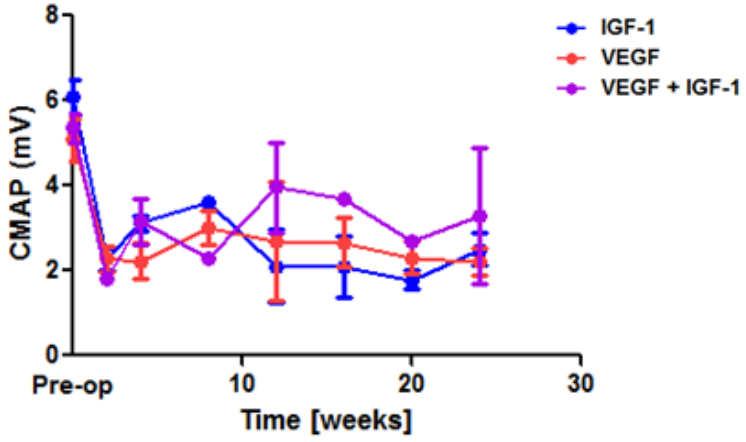


Figure 4.15. Single Injection of VEGF and/or IGF-1 alginate to a muscle transplant in rabbits provides only minimal functional improvement at early timepoints. A gracilis muscle transplant was treated with VEGF, IGF-1, or VEGF + IGF-1 alginate at the time of transplantation. At various timepoints following surgery electromyography was used to measure the CMAP of the transplanted muscle tissue. While minimal muscle functional improvement was observed in the first weeks following surgery, function essentially plateaued through the end of the study (24wks). Values are mean ±SEM, n=6 for IGF-1, n=5 for VEGF, n=2 for VEGF + IGF-1. No statistically significant differences were identified with a 2-way ANOVA with Bonferroni post-test.

4.4 Discussion

Microvascular muscle transfer is the gold standard for treating chronic facial paralysis [5, 6]. However, progressive obstacles to axon regrowth into muscle following chronic paralysis, and unpredictable reinnervation following surgical interventions [7, 8, 13, 12] leave many patients with a

poorly functional result. Here we show a beneficial interplay between VEGF and IGF-1, when an alginate gel is used to provide a sustained source in the transplanted muscle. Intramuscular injection of VEGF + IGF-1 alginate in this study, led to improved total myofiber area, increased muscle contraction velocity and strength, and improved functional innervation in aged mice. Alginate injection into donor muscle, in an adult rabbit model of craniofacial muscle transfer, led to improved transplant innervation and function.

Sustained IGF-1 delivery alone from alginate gels significantly improved myofiber regeneration and muscle function in a murine model of sciatic nerve ligation and microvascular neurorrhaphy. In aged mice, IGF-1 alginate increased the percent myofiber cross-sectional area by 22% as compared to blank alginate (Fig. 4.13 A,B) and resulted in 2.2 and 2.4-fold increases in TA contraction force and velocity, respectively, on day 85 after surgery (Fig. 4.13 C,D). Similar trends in muscle function were observed in young mice with IGF-1 alginate (Fig. 4.6 E,F). These data are consistent with previous studies that show that IGF-1 plays a central role in muscle regeneration by activating pathways that control both satellite cell activation, and myofiber survival and hypertrophy [27]. Virally delivered IGF-1 genes have also been shown to induce skeletal muscle hypertrophy, attenuate age-related atrophy, and improve strength both by modulating calcineurin-signaling in skeletal myocytes [44], down-regulating proinflammatory cytokines and limiting fibrosis [45]. IGF-1 may also play a role in promoting muscle regeneration following sciatic nerve injury by promoting axon regeneration. Previous reports have shown that IGF-1 increases the rate of axon regeneration following crush-injured rat sciatic nerves [46]. In the current study, however, the increase in muscle force following IGF-1 alginate treatment, with only modest improvements in toe spreading, suggests that IGF-1 delivery had a direct effect on muscle regeneration. Previous studies using young mouse models of ischemic muscle injury report a modest effect on myofiber regeneration and neoangiogenesis with IGF-1 alginate [28]. The present study suggests that similar improvements in muscle regeneration can be achieved following sciatic nerve injury in young mice, and that even more pronounced improvements in muscle regeneration and function can be achieved in aged mice with IGF-1. This is consistent with previous studies that show that local Igf-1 transgene expression helps maintain

hypertrophy and regeneration in aged skeletal muscle [47] and suggests that alginate delivery of IGF-1 in adult patients may significantly improve functional muscular outcomes.

Sustained VEGF delivery from alginate gels improved sciatic nerve function and toe spreading in mice. Following administration of a booster injection of VEGF alginate to young mice ~90% showed improved TSF and SSI (Fig. 4.6 B,D). This is in accord with previous reports that VEGF is implicated in muscle reinnervation via direct neuroprotective effects [48]. In previous studies, when alginate was used to deliver VEGF following ischemic injury in mice, the expression of nerve growth factor and glial-derived neurotrophic factor was induced, the loss of skeletal muscle innervations was ameliorated, and axon regrowth was promoted [26]. The expression of functional VEGF receptors on Schwann cells suggests that VEGF may also directly affect neural integrity [49]. Previous reports that have used toe spreading analysis as a measure of functional reinnervation have shown that VEGF gene therapy following sciatic nerve transection in mice resulted in increased numbers of myelinated fibers, higher gastrocnemius weight, and improved sciatic functional index scores [50]. In those studies, VEGF gene therapy, administered at the time of surgery, resulted in a 1.4-fold improvement in sciatic functional index 42 days after surgery [50]. In this study, a single injection of VEGF alginate at the time of surgery resulted in a comparable improvement in SSI (1.5-fold) 50 days after surgery (Fig. 2D). Alginate delivery of recombinant VEGF, however avoids the risks and barriers associated with gene therapy [51]. Furthermore, administration of booster injections allowed continued functional improvement in toe spreading and SSI to occur (Fig. 3A-D). The requirement for booster VEGF alginate injections every 20-30 days to prolong functional toe spreading corresponds with the release of VEGF over this timeframe [28], and suggests that VEGF release plays a critical role in promoting reinnervation and maintaining nerve function.

Combined delivery of VEGF + IGF-1 improved both muscle strength and nerve function throughout the hindlimb following sciatic nerve ligation and microvascular neurorrhaphy. VEGF + IGF-1 alginate prolonged the period of functional recovery following sciatic nerve injury in aged mice and

maintained long-term functional improvements in toe spreading and muscle strength. In particular, VEGF + IGF-1 alginate resulted in the most significant improvements in myofiber area (Fig. 4.13 A-B), toe spreading (Fig. 4.9 D-F), and sciatic nerve function (Fig. 4.9 G) as compared to single growth factor delivery and negative controls in aged mice. Previous studies of hindlimb ischemia have shown that VEGF + IGF-1 act synergistically to promote angiogenesis, reinnervation, and myogenesis [28, 52, 37, 53]. In those studies, the combined delivery of VEGF + IGF-1 from alginate gels [28, 52] resulted in ~1.7 – 6.0-fold increases in muscle contraction force at 6 weeks post injury, compared to negative controls in young mice. The present study suggests that similar functional improvements in muscle regeneration (2.8 and 3.0-fold increases in contraction force and velocity, respectively) can be achieved in aged mice with combined delivery of VEGF + IGF-1 following sciatic nerve injury. Synergy between VEGF and IGF-1 is likely critical to promote functional muscle and nerve regeneration in aged mice, and is significantly more effective than single growth factor delivery. This is consistent with previous reports that show that spontaneous perfusion recovery following injury of the femoral artery, vein, and nerve in mice diminishes with increasing age; only combined delivery of VEGF + IGF-1 rescued perfusion in mice $\geq$13 months old [37]. Clinically, patients under 16yrs of age are four times more likely to have a satisfactory motor recovery following microsurgical nerve repair than patients over 40 [10].

VEGF + IGF-1 work synergistically to improve nerve synaptic function. Although combined delivery did not appear to increase the number of structural NMJ connections compared to blank alginate (Fig. 4.2 C-D), growth factor delivery improved nerve synapse and ultimately toe spreading function in both young and aged mice (Figs. 4.3, 4.9). This former finding is consistent with previous studies that show that NMJ synaptic function is not well correlated with anatomic structure [13]. Although peripheral nerves can structurally reconnect with motor end plates, there is a consistent inability of these connections to be functional after prolonged denervation (>1month in mice and rats) [13]. Importantly, a meta-analysis based on individual patient data has also shown that longer delays between nerve injury and repair are associated with a lower chance of motor recovery [10]. The improved functional outcome

observed in the present study following treatment with VEGF + IGF-1 alginate may have been the result of more rapid reinnervation following injury, or improved neurotransmitter release or postsynaptic responses. Studies using VEGF + IGF-1 following ischemic injury have shown a more rapid recovery of NMJ connections compared to negative control groups, but in those studies, nerve synaptic function was not tested [28].

VEGF + IGF-1 alginate treatment of donor muscle tissue improved the functional outcome of a microvascular craniofacial muscle transplant in rabbits. Measurement of CMAPs has been shown to be a reliable postoperative monitoring technique for the vascularity and function of transplanted muscle; clinically, a persistent decrease by >40% in CMAP amplitude indicates vascular compromise [54]. VEGF + IGF-1 alginate promoted a more rapid recovery in CMAP in the transplanted muscle, ultimately resulting in a 71% increase compared to the blank alginate group at 9wks, and recovery of 97% of the pre-transplantation muscle CMAP at 12wks post surgery (Fig. 4.14 C). This finding may be particularly relevant in relation to multiple reported cases where gracilis muscles transferred to the craniofacial region were well perfused and showed no signs of tissue necrosis, yet salvage procedures were required because muscle reinnervation was insufficient to generate function and raised concerns for muscle atrophy [55]. Recent clinical work has been focused on identifying the most appropriate motor nerve to innervate the transplanted muscle [2, 56], while bioengineers have focused on the innervation of artificial skeletal muscle constructs [23, 24]. In a recent report, the murine femoral nerve was diverted into an engineered muscle construct [24], similar to the procedure used in microvascular muscle transfer. While the implanted construct was innervated sufficiently to generate a CMAP reading following stimulation, the CMAP waveform was irregular and the amplitude much lower than that of native muscle [24].

In sum, the current study presents a method that builds on both current clinical expertise regarding craniofacial microvascular transplantation, and established biomaterials for the controlled release of growth factors, to improve the functional muscular and neural outcome of muscle transplant procedures. Here we show that this technique can be easily scaled based on the volume of tissue to be

treated, and circumvents the current limitations of tissue engineered artificial muscle. Delivering growth factors directly into autologous donor muscle may provide a rapid route to clinical adaption, and significantly improve functional outcomes for patients with facial paralysis.

4.5 References

[1] R. Zuker, C. Goldberg and R. Manktelow, "Facial animation in children with mobius syndrome after segmental gracilis msucle transplant," *Plastic and reconstructive surgery,* vol. 106, no. 1, pp. 1-8, 2000.

[2] D. Chuang, J. Lu, T. Chang and V. Laurence, "Comparison of Functional Results After Cross-Face Nerve Graft-, Spinal Accessory Nerve-, and Masseter Nerve-Innervated Gracilis for Facial Paralysis Reconstruction," *Annals of Plastic Surgery,* doi. 10.1097/SAP.0000000000001327, 17 Apr 2018.

[3] D. Alam, "Rehabilitation of Long-standing Facial Nerve Paralysis With Percutaneous Suture–Based Slings," *Arch Facial Plast Surg,* vol. 9, no. 3, pp. 205-209, 2007.

[4] J. Thiele, H. Bannasch, G. Stark and S. Eisenhardt, "Single-stage Dynamic Reanimation of the Smile in Irreversible Facial Paralysis by Free Functional Muscle Transfer," *J. Vis. Exp,* vol. 97, p. e52386, 2015.

[5] R. Mehta, "Surgical Treatment of Facial Paralysis," *Clinical and Experimental Otorhinolaryngology,* vol. 2, no. 1, pp. 1-5, 2009.

[6] R. Lindsay, P. Bhama and T. Hadlock, "Quality-of-Life Improvement After Free Gracilis Muscle Transfer for Smile Restoration in Patients With Facial Paralysis," *JAMA Facial Plast Surg,* vol. 16, no. 6, pp. 419-24, 2014.

[7] F. Biglioli et al., "Recovery of Emotional Smiling Function in Free-Flap Facial Reanimation," *J Oral Maxillofac Surg,* vol. 70, pp. 2413-8, 2012.

[8] K. Barrie, S. Steinmann, A. Shin, R. Spinner and A. Bishop, "Gracilis free muscle transfer for restoration of function after complete brachial plexus avulsion," *Neurosurg Focus,* vol. 16, no. 5, pp. 1-9, 2004.

[9] V. Guaiquil et al., "VEGF-B selectively regenerates injured peripheral neurons and restores sensory and trophic functions," *Proc Natl Acad Sci USA,* vol. 111, no. 48, p. 17272–17277, 2014.

[10] A. Ruijs, J. Jaquet, S. Kalmijn, H. Giele and S. Hovius, "Median and Ulnar Nerve Injuries: A Meta-Analysis of Predictors of Motor and Sensory Recovery after Modern Microsurgical Nerve Repair," *Plast. Reconstr. Surg.,* vol. 116, no. 2, pp. 484-94, 2005.

[11] Y. Son and W. Thompson, "Schwann cell processes guide regeneration of peripheral axons," *Neuron,* vol. 14, pp. 125–132, 1995.

[12] H. Kang, L. Tian, M. Mikesh, J. Lichtman and W. Thompson, "Terminal Schwann cells participate in neuromuscular synapse remodeling during reinnervation following nerve injury," *The Journal of neuroscience: the official journal of the Society for Neuroscience,* vol. 34, pp. 6323–633, 2014.

[13] M. Sakuma et al., "Lack of motor recovery after prolonged denervation of the neuromuscular junction is not due to regenerative failure," *Eur J Neurosci,* vol. 43, no. 3, p. 451–462, 2016.

[14] B. Carlson and J. Faulkner, "Muscle transplantation between young and old rats: age of host determines recovery," *American Journal of Physiology-Cell Physiology,* vol. 256, no. 6, pp. C1262-C1266, 1989.

[15] I. Conboy et al., "Rejuvenation of aged progenitor cells by exposure to a young systemic environment," *Nature,* vol. 433, pp. 760-764, 2005.

[16] O. Delbono, "Neural control of aging skeletal muscle," *Aging Cell,* vol. 2, no. 1, pp. 21-29, 2003.

[17] A. Wagers and I. Conboy, "Cellular and molecular signatures of muscle regeneration: Current concepts and controversies in adult myogenesis," *Cell,* vol. 122, no. 5, pp. 659-667, 2005.

[18] I. Conboy, M. Conboy, G. Smythe and T. Rando, "Notch-mediated restoration of regenerative potential to aged muscle," *Science,* vol. 302, pp. 1575–1577, 2003.

[19] J. Chakkalakal, K. Jones, M. Basson and A. Brack, "The aged niche disrupts muscle stem cell quiescence," *Nature,* vol. 490, pp. 355-360, 2012.

[20] E. Barton-Davis, D. Shoturma, A. Musaro, N. Rosenthal and H. Sweeney, "Viral mediated expression of insulin-like growth factor I blocks the aging-related loss of skeletal muscle function," *Proc. Natl. Acad. Sci. USA,* vol. 95, pp. 15603–15607, 1998.

[21] M. Grounds, "Reasons for the degeneration of ageing skeletal muscle: a central role for IGF-1 signalling," *Biogerontology,* vol. 3, p. 19–24, 2002.

[22] B. Scicchitano, E. Rizzuto and A. Musarò, "Counteracting muscle wasting in aging and neuromuscular diseases: the critical role of IGF-1," *Aging,* vol. 1, no. 5, pp. 451-7, 2009.

[23] C. Fuoco et al., "In vivo generation of a mature and functional artificial skeletal muscle," *EMBO Molecular Medicine,* vol. 10, no. 5, p. e201404062, 2015.

[24] T. Kaufman et al., "Innervation of an engineered muscle graft for reconstruction of muscle defects," *Am J Transplantation,* doi: 10.1111/ajt.14957, 2018.

[25] E. Silva and D. Mooney, "Spatiotemporal control of vascular endothelial growth factor delivery from

injectable hydrogels enhances angiogenesis," *J Thromb Haemost,* vol. 5, pp. 590-8, 2007.

[26] D. Shvartsman et al., "Sustained Delivery of VEGF Maintains Innervation and Promotes Reperfusion in Ischemic Skeletal Muscles Via NGF/GDNF Signaling," *Molecular Therapy,* vol. 22, no. 7, pp. 1243–1253, 2014.

[27] M. Heszele and S. Price, "Insulin-like growth factor I: The yin and yang of muscle atrophy," *Endocrinology,* vol. 145, pp. 4803–4805, 2004.

[28] C. Borselli, H. Storriea, F. Benesch-Leec, D. Shvartsmana, C. Cezara, J. Lichtmane, H. Vandenburgh and D. Mooney, "Functional muscle regeneration with combined delivery of angiogenesis and myogenesis factors," *Proc Natl Acad Sci USA,* vol. 107, no. 8, p. 3287–3292, 2010.

[29] A. Hoke, T. Gordon, D. Zochodne and O. Sulaiman, "A decline in glial cell-line-derived neurotrophic factor expression is associated with impaired regeneration after long-term Schwann cell denervation," *Exp Neurol,* vol. 173, no. 1, pp. 77-85, 2002.

[30] D. Augst, H. Kong and D. Mooney, "Alginate Hydrogels as Biomaterials," *Macromol. Biosci,* vol. 6, pp. 623–633, 2006.

[31] T. Boontheekul, H. Kong and D. Mooney, "Controlling alginate gel degradation utilizing partial oxidation and bimodal molecular weight distribution," *Biomaterials,* vol. 26, pp. 2455–2465, 2005.

[32] T. Richardson et al., "Polymeric system for dual growth factor delivery," *Nat Biotechnol,* vol. 19, pp. 1029-34, 2001.

[33] R. Chen et al., "Integrated approach to designing growth factor delivery systems," *FASEB J,* vol. 21, no. 14, pp. 3896–3903, 2007.

[34] E. Silva and D. Mooney, "Effects of VEGF temporal and spatial presentation on angiogenesis," *Biomaterials,* vol. 31, pp. 1235–1241, 2010.

[35] S. Eppler et al., "A target-mediated model to describe the pharmacokinetics and hemodynamic effects of recombinant human vascular endothelial growth factor in humans," *Clin Pharmacol Ther,* vol. 72, no. 1, pp. 20-32, 2002.

[36] T. Henry et al., "The VIVA trial: vascular endothelial growth factor in ischemia for vascular angiogenesis," *Circulation,* vol. 107, pp. 1359-65, 2003.

[37] E. Anderson et al., "VEGF and IGF Delivered from Alginate Hydrogels Promote Stable Perfusion Recovery in Ischemic Hind Limbs of Aged Mice and Young Rabbits," *J Vasc Res,* vol. 54, pp. 288–298, 2017.

[38] N. Geifman and E. Rubin, "The Mouse Age Phenome Knowledgebase and Disease-Specific Inter-Species Age Mapping," *PLoS ONE,* vol. 8, no. 12, p. e81114. doi:10.1371/journal.pone.0081114,

2013.

[39] C. Borselli, H. Storrie, F. Benesch-Lee, D. Shvartsmana, C. Cezara, J. Lichtmane, H. Vandenburgh and D. Mooney, "Functional muscle regeneration with combined delivery of angiogenesis and myogenesis factors," *Proc Natl Acad Sci USA,* vol. 107, no. 8, pp. 3287–3292, 2010.

[40] M. Singh, H. Li, E. Caterson and S. Talbot, "Innervated Free Gracilis Muscle Transfer: An Experimental Model," *J Craniofac Surg,* vol. 27, no. 6, pp. 1515-6, 2016.

[41] M. Bervar, "Video analysis of standing — an alternative footprint analysis to assess functional loss following injury to the rat sciatic nerve," *J Neurosci Methods,* vol. 102, no. 2, pp. 109-116, 2000.

[42] F. Faul, E. Erdfelder, A. Lang and A. Buchner, "G*Power 3: A flexible statistical power analysis program for the social, behavioral, and biomedical sciences," *Behav Res Meth,* vol. 39, no. 2, pp. 175-191, 2007.

[43] A. Baptisa et al., "A new approach to assess function after sciatic nerve lesion in the mouse—Adaptation of the sciatic static index," *J Neurosci Methods,* vol. 161, no. 2, pp. 259-264, 2007.

[44] A. Musaro, K. McCullagh, F. Naya, E. Olson and N. Rosenthal, "IGF-1 induces skeletal myocyte hypertrophy through calcineurin in association withGATA-2 and NF-ATc1," *Nature,* vol. 400, pp. 581-5, 1999.

[45] L. Pelosi et al., "Local expression of IGF-1 accelerates muscle regeneration by rapidly modulating inflammatory cytokines and chemokines," *FASEB J,* vol. 21, pp. 1393–1402, 2007.

[46] E. Emel et al., "Effects of insulin-like growth factor–I and platelet-rich plasma on sciatic nerve crush injury in a rat model Laboratory investigation," *J Neurosurgery,* vol. 114, no. 2, pp. 522-8, 2011.

[47] A. Musaro et al., "Localized Igf-1 transgene expression sustains hypertrophy and regeneration in senescent skeletal muscle," *Nature Genetics,* vol. 27, pp. 195-200, 2001.

[48] K. Jin, X. Mao and D. Greenberg, "Vascular endothelial growth factor: Direct neuroprotective effect in in vitro ischemia," *Proc Natl Acad Sci USA,* vol. 97, no. 18, pp. 10242–10247, 2000.

[49] P. Schratzberger et al., "Favorable effect of VEGF gene transfer on ischemic peripheral neuropathy," *Nature Med,* vol. 6, no. 4, pp. 405-13, 2000.

[50] F. Lopes et al., "Enhancement of sciatic nerve regeneration after vascular endothelial growth factor (VEGF) gene therapy," *Neuropathology and Applied Neurobiology,* vol. 37, pp. 600-12, 2011.

[51] D. Ibraheem, A. Elaissari and H. Fessi, "Gene therapy and DNA delivery systems," *International Journal of Pharmaceutics,* vol. 459, pp. 70-83, 2014.

[52] C. Borselli, C. Cezar, D. Shvartsman, H. Vandenburgh and D. Mooney, "The role of multifunctional

delivery scaffold in the ability of cultured myoblasts to promote muscle regeneration," *Biomaterials,* vol. 32, pp. 8905-8914, 2011.

[53] L. Wang et al., "Minimally Invasive Approach to the Repair of Injured Skeletal Muscle With a Shape-memory Scaffold," *Molecular Therapy,* vol. 22, no. 8, pp. 1441–1449, 2014.

[54] A. Khater et al., "The use of compound muscle action potentials (CMAP) for postoperative monitoring of free functioning gracilis muscle transfer: A preliminary report," *Journal of Plastic, Reconstructive & Aesthetic Surgery,* vol. 68, pp. e137-e146, 2015.

[55] S. Eisenhardt, N. Eisenhardt, J. Thiele, G. Stark and H. Bannasch, "Salvage Procedures After Failed Facial Reanimation Surgery Using the Masseteric Nerve as the Motor Nerve for Free Functional Gracilis Muscle Transfer," *JAMA Facial Plast Surg,* vol. 16, no. 5, pp. 359–363, 2014.

[56] Y. Bae, R. Zuker, R. Manktelow and S. Wade, "A Comparison of Commissure Excursion following Gracilis Muscle Transplantation for Facial Paralysis Using a Cross-Face Nerve Graft versus the Motor Nerve to the Masseter Nerve," *Plast. Reconstr. Surg.,* vol. 117, no. 7, pp. 2407-13, 2006.

CHAPTER 5:

Conclusions, Implications, and Future Directions

5.1 Summary and Conclusions

Both modulation of the innate inflammatory response and promotion of tissue regeneration are important for the restoration of functional tissue following injury or chronic disease. In this thesis, two biomaterial systems were explored to address each of these critical aspects of tissue regeneration and were tested for therapeutic efficacy in the context of skeletal muscle regeneration. AuNPs with mixed monolayers of PEG and cytokine were designed to direct macrophage polarization towards the anti-inflammatory and pro-regenerative M2 phenotypes. The ability of these particles to deliver various cytokines and direct the polarization of a broad range of M2 states was demonstrated by their ability to conjugate IL-4, IL-13, and IL-10 and promote the polarization of human M2a and M2c macrophages in vitro. Further, PEG stabilized, IL-4 conjugated AuNPs were tested in a murine model of ischemic skeletal muscle injury to examine their ability to direct M2a macrophage polarization in vivo and ultimately improve the regeneration of functional muscle tissue. Separately, an established alginate scaffold used for the delivery of tissue regenerative cytokines, VEGF and IGF-1 [1], was explored in the new context of muscle transplantation.

Chapter 2 focused on the development of a nanoparticle system to direct M2 macrophage polarization. Partial PEGylation of the AuNP surface increased particle stability and monodispersity, and decreased serum protein adsorption. Further, partial PEGylation allowed for the conjugation of M2 polarizing cytokines, IL-4, IL-13, and IL-10, directly to the remaining Au surface. Importantly, PEGylation did not interfere with cytokine bioactivity, and all of the conjugated cytokines tested were able to direct human M2 macrophage polarization in vitro. Further, PEG-AuNP-IL4 and PEG-AuNP-IL10 were able to direct the polarization of both naïve and M1 polarized human macrophages towards M2 phenotypes in vitro.

In Chapter 3, PEGylated, IL-4 conjugated AuNPs were used in vivo for the treatment of skeletal muscle following surgically induced ischemic injury. On day 3 following injury, the particles were administered non-invasively via intramuscular injection, such that 2μg IL-4/muscle was delivered. This timing was coordinated with the initial inflammatory response, and corresponded with macrophage recruitment to the muscle. Macrophages played a critical role in promoting muscle regeneration following ischemic injury, and their depletion with clodronate-liposomes inhibited functional muscle regeneration. Further, PEG-AuNP-IL4 treatment enhanced muscle regeneration by shifting the balance of macrophages away from the inflammatory and towards the M2a state. Treatment with PEG-AuNP-IL4 resulted in a ~2-fold increase in the percentage of macrophages expressing the M2a phenotype and a ~2-fold decrease in M1 macrophages, as compared to mice treated with vehicle only. This shift in macrophage polarization was associated with improved muscle structure and a ~40% increase in muscle force generation. This improvement in muscle force in response to modulation of macrophage polarization by a single factor, IL-4, is comparable to that previously reported in response to scaffold delivery of VEGF, IGF-1, and/or myoblasts following ischemic muscle injury [1, 2, 3]. This suggests that modulation of the innate immune response by a single cytokine can be as potent as the combined delivery of multiple growth factors aimed at directly stimulating tissue regeneration. The shift in macrophage polarization played a central role in the improvement of muscle recovery, as the depletion of monocytes/macrophages eliminated the therapeutic effects of PEG-AuNP-IL4 treatment.

In Chapter 4, an alternative approach, the delivery of growth factors to directly stimulate tissue resident cells, to promote regeneration was explored. Here, a well-established injectable alginate scaffold capable of providing sustained local release of VEGF and IGF-1 [1] was used in the context of muscle transplantation. In a murine model of sciatic nerve ligation and neurorrhaphy, sustained IGF-1 delivery alone from alginate gels significantly improved myofiber regeneration and muscle function, while VEGF delivery alone improved sciatic nerve function and toe spreading. Combined delivery of VEGF + IGF-1 improved both muscle strength and nerve function. VEGF + IGF-1 delivery to aged mice resulted in

prolonged toe function, increased toe spreading, and improved the static sciatic index score, indicative of improved sciatic nerve and neuromuscular junction function. Further, a 26% increase in muscle fiber area, and 2.8 and 3.0-fold increases in muscle contraction force and velocity, respectively, were found compared to blank alginate injection. This strategy was subsequently tested in a rabbit model of craniofacial gracilis muscle transplantation. VEGF + IGF-1 alginate treatment of donor muscle tissue improved the functional outcome of a microvascular craniofacial transplant. Electromyography demonstrated a 71% increase in compound muscle action potential in the transplanted tissue 9 weeks after transplantation following treatment with VEGF + IGF-1 alginate, compared to blank alginate. Together this work suggests that sustained delivery of VEGF + IGF-1 from alginate improves the regeneration of muscle innervations and function following nerve injury and muscle transplantation.

5.2 Implications

This thesis has expanded the use of AuNPs as drug delivery vectors for the resolution of inflammation and the promotion of M2 macrophage polarization. While nanoparticles have been studied extensively for drug delivery, relatively few applications employ the conjugation of functional cytokines directly to the surface of AuNPs, and further, very few nanoparticle systems have been developed to direct M2 macrophage polarization [4]. The principles developed in this thesis, begin to establish a general method for the use of AuNPs for the delivery of anti-inflammatory cytokines that could likely be applied to any cytokine with disulfide or thiol groups available to participate in thiol-gold bonds, or an isoelectric point that would support electrostatic binding to AuNPs. The strategies developed here for the generation of particles with mixed monolayers of PEG and cytokine, such that particle stability and cytokine bioactivity are retained, are expected to find broad utility for cytokine therapies, especially in the context of inflammation.

Importantly, this thesis has shown that modulation of macrophage polarization by material delivery of polarizing cytokines is a potent therapeutic strategy to promote tissue regeneration. The ability

to shift inflammatory macrophage polarization towards pro-regenerative M2 states will likely be important for the treatment of many non-healing wounds and chronic inflammatory conditions. In fact, imbalanced macrophage activation contributes to the pathogenesis of atherosclerosis [5], inflammatory bowel disease [6], rheumatoid and osteoarthritis [7, 8], multiple sclerosis [9], and muscular dystrophy [10] among other conditions. However, the ability to control inflammation in vivo following injury, or in the context of chronic disease, has proven challenging. This thesis presents a method of cytokine delivery capable of shifting the balance of macrophage polarization in an inflammatory microenvironment in vivo, that of an ischemic muscle, away from the M1 and towards the M2a state. The ability to direct M2 macrophage polarization in vivo is expected to find broad clinical utility in the treatment of non-healing wounds, tissue regeneration, degenerative disease, and chronic inflammatory conditions.

Finally, the application of an established biomaterial for the dual delivery of VEGF + IGF-1 in the context of muscle transplantation has demonstrated the clinical utility of sustained growth factor delivery from biomaterials. The sustained release established an increasing concentration gradient into the transplant that mimicked natural paracrine signaling, and ultimately improved engraftment and function of the transplanted tissue. Importantly, this strategy side-steps the current limitations of artificially engineered muscle tissue and presents a clear path for the rapid clinical adaption of this biomaterial delivery technology. While recent advancements in the design of artificial muscle are promising, artificial constructs are still unable to recapitulate natural muscle function [11]. Further, unpredictable nerve regeneration following current surgical procedures leaves approximately 48% of patients with unsatisfactory motor recovery [12]. The technology described here provides a methodology to improve the engraftment, innervation, and ultimately function of transplanted tissue and does not necessitate artificial muscle constructs. As such, it builds on current microsurgical techniques and is expected to provide rapid clinical adaptation for muscle transplantation procedures. Further, this concept of using biomaterials to provide an increasing gradient of growth factors into donor tissue, may prove useful in the transplantation of other tissues.

5.3 Future Directions

This thesis has demonstrated that biomaterial systems can significantly improve the regeneration of tissue function both by modulating the inflammatory response and by directly promoting tissue regeneration. The ability of biomaterials to direct both of these facets of tissue regeneration were explored independently, in the context of skeletal muscle regeneration. The principles developed here, specifically, the ability of nanoparticles to promote cytokine driven macrophage polarization in vivo, the potency of macrophage modulation as a therapeutic strategy for tissue regeneration, and the ability of alginate gels to locally mimic paracrine signaling and improve functional tissue engraftment, open a wide range of research directions that will increase our understanding of tissue regenerative therapeutic strategies.

The cytokine conjugated nanoparticles developed here were shown to be stable, maintain cytokine bioactivity, and direct macrophage polarization in vivo. However further optimization of the nanoparticles may improve their therapeutic efficacy. In particular, modulation of nanoparticle size and shape would be expected to alter macrophage interactions with the particles [13, 14]. Decreasing macrophage internalization by increasing the aspect ratio may alter the binding of nanoparticle-conjugated cytokines with extracellular receptors on macrophages and thereby impact polarization. Furthermore, the varying methods of particle internalization dictated in part by particle size may also bias macrophage polarization and provides another design parameter. Nanoparticle size and shape have also been shown to significantly impact biodistribution following systemic administration [15], alter rates of particle clearance by the lymphatic system, and effect particle residence time in the tissue. Nanoparticle residence time in the tissue of interest will also likely be an important parameter in modulating macrophage polarization. Because macrophage polarization is plastic and constantly mutates in response to cytokines in the microenvironment, developing particles that have increased tissue residence time may be important in controlling macrophage polarization, especially in the context of chronic inflammation.

Interestingly, the PEGylated, IL-4 conjugated AuNPs developed in this thesis were shown to be potent stimulators of the M2a phenotype. However, the metabolism of the AuNPs was not explored here. Better understanding of cytokine-conjugated AuNP interactions with extracellular macrophage receptors, the rate of receptor binding, the possible role of receptor clustering by cytokine-conjugated AuNPs, and how the AuNPs are internalized and processed intracellularly will be important to better understand possible distinctions between AuNP-conjugated versus soluble cytokine driven macrophage polarization. Further, the heterogeneity of macrophage phenotypes following stimulation with soluble and AuNP-conjugated IL-4 limited the extent of M2a polarization, but is still poorly understood. Such improved mechanistic understanding, along with exploring how the cytokine-conjugated AuNPs are cleared from the body will be important in determining their potential long term toxicity. Although human IL-4 would not be expected to be recognized as foreign, the prolonged presence of AuNP-conjugated IL-4 may lead to the generation of a humoral immune response. IL-4 plays a central role in controlling adaptive immunity, and can promote the differentiation and division of B cells [16]. Determining if, and on what time-scale, an antibody response is generated will be important as it will have important implications for the repeated use of this technology in a single patient and for its application to chronic conditions.

While this thesis demonstrated the ability of PEGylated, cytokine-conjugated AuNPs to direct macrophage polarization in the context of acute ischemic muscle injury, it would be of significant clinical relevance to test the ability of these particles to direct macrophage polarization in the context of chronic inflammatory disease. Chronic inflammation plays a significant role in the pathogenesis of many conditions, including 7 of the 10 leading causes of death in the United States (CDC, 2016), and appropriate modulation of the inflammatory response holds promise for the improved treatment of many chronic diseases. Although the nanoparticle system presented here holds promise for the treatment of these conditions, the challenges associated with chronic disease have not been addressed here. Retention of the nanoparticles in tissues of interest, and the duration of therapeutic efficacy should be explored. Modulation of nanoparticle size, discussed above, and the use of repeated injections, as described in

Chapter 4 for the biomaterial delivery of VEGF + IGF-1 in muscle transplants, may be beneficial in the adaption of the AuNP therapy developed here to chronic disease. Given the clear effects of macrophage polarization on muscle regeneration, the treatment of duchenne muscular dystrophy, a disease characterized by chronic inflammation and progressive muscle wasting, with the nanoparticles developed here is particularly attractive. Another advantage of the nanoparticle system presented here is its ability to deliver multiple M2 polarization cytokines of interest, the ability to deliver multiple factors will also likely be important for the treatment of chronic disease. For example, inflamed synovial macrophages associated with rheumatoid arthritis are unable to respond to the anti-inflammatory effects of IL-10 alone, which would normally be beneficial for arthritis [17, 18]. Despite this challenge, it has been suggested that synergistic effects of IL-4 and IL-10 may be beneficial in the suppression of synovial inflammation [19, 20].

Another advantage of nanoparticles is their ability to be targeted to tissues of interest, either by the conjugation of targeting moieties, modulation of surface chemistry, or by physical properties that exploit extravagation through the leaky vasculature associated with tumors and inflamed tissue. While the treatment of many localized non-healing wounds could be addressed by the nanoparticles developed here, perhaps including diabetic foot ulcers, localized traumatic muscle injury, and transplantation tissue, among others, the ability to home to disperse tissues affected by systemic chronic inflammation would likely increase their therapeutic utility. An antibody (the F8 antibody) has been identified that recognizes the alternatively spliced extra domain A of fibronectin, a marker strongly over expressed at sites of arthritis, and can be used to target the delivery of therapeutics to these sites [21]. The potential to conjugate such targeting biomolecules to the surface of the AuNPs developed here holds great promise.

In this thesis a hydrogel for dual delivery of VEGF + IGF-1 has shown improved functional regeneration in clinically relevant animal models of skeletal muscle injury; sciatic nerve injury in aged mice, and large muscle transplantation in adult rabbits. Continued development of this system in large animal models (pigs) is ongoing. Given the interaction between the immune response and muscle

regeneration extensively studied by others [22], and exploited here in the context of ischemic muscle injury, it will be important to explore the effects of the VEGF + IGF-1 delivering hydrogel on the immune response. The immune response is expected to play a central role in orchestrating muscle regeneration and exploring the effects of VEGF + IGF-1 in this context would significantly enlighten the mechanism of this biomaterial treatment. Furthermore, the incorporation of polarizing cytokines or the AuNP-cytokines developed here into the alginate hydrogel, or the dual treatment of muscles with the hydrogel and the AuNPs developed here, may further improve functional tissue regeneration by controlling the immune response in concert with promoting muscle tissue regeneration.

In summary, this thesis explores the ability of biomaterials to both modulate the innate inflammatory response and directly promote tissue regeneration, independently, in the context of skeletal muscle regeneration. The ability to control the inflammatory response, and specifically, direct macrophage polarization is expected to find clinical utility in the treatment of non-healing wounds, tissue regeneration and chronic inflammatory disease. Further, the development of biomaterials that will coordinate the immune response with tissue regeneration represents an exciting avenue for the advancement of tissue regenerative therapies.

5.4 References

[1] C. Borselli et al., "Functional muscle regeneration with combined delivery of angiogenesis and myogenesis factors," *Proc Natl Acad Sci USA,*vol. 107, no. 8, pp. 3287–3292, 2010.

[2] C. Borselli, C. Cezar, D. Shvartsmana, H. Vandenburgh and D. Mooney, "The role of multifunctional delivery scaffold in the ability of cultured myoblasts to promote muscle regeneration," *Biomat,* vol. 32, pp. 8905-8914, 2011.

[3] L. Wang, L. Cao, J. Shansky, Z. Wang, D. Mooney and H. Vandenburgh, "Minimally Invasive Approach to the Repair of Injured Skeletal Muscle With a Shape-memory Scaffold," *Molecular Therapy,* vol. 22, no. 8, pp. 1441–1449, 2014.

[4] X. Miao, X. Leng and Q. Zhang, "The Current State of Nanoparticle-Induced Macrophage

Polarization and Reprogramming Research," *Int. J. Mol. Sci.,* vol. 18, no. 2, pp. 336-348, 2017.

[5] A. Mantovani, C. Garlanda, M. Locati, "Macrophage Diversity and Polarization in Atherosclerosis: A Question of Balance," *Arterioscler Thromb Vasc Biol,* vol. 29, no. 10, pp. 1419-1423, 2009.

[6] X. Zhang, D.M. Mosser, "Macrophage activation by endogenous danger signals," *J Pathol,* vol. 214, no. 2, pp. 161-178, 2008.

[7] R. W. Kinne, B. Stuhlmuller, G. Burmester, "Cells of the synovium in rheumatoid arthritis. Macrophages.," *Arthritis Res Ther,* vol. 9, no. 6, pp. 224-239, 2007.

[8] N. Fahy et al., "Human osteoarthritic synovium impacts chondrogenic differentiation of mesenchymal stem cells via macrophage polarisation state," *HumaOsteoarthritis and Cartilage,* vol. 22, no. 8, pp. 1167-1175, 2014.

[9] J. Mikita et al., "Altered M1/M2 activation patterns of monocytes in severe relapsing experimental rat model of multiple sclerosis. Amelioration of clinical status by M2 activated monocyte administration," *Multiple Sclerosis Journal,* vol. 17, no. 1, pp. 2-15, 2011.

[10] S. Villalta, B. Deng, C. Rinaldi, M. Wehling-Henricks and J. Tidball, "IFN-γ Promotes Muscle Damage in the mdx Mouse Model of Duchenne Muscular Dystrophy by Suppressing M2 Macrophage Activation and Inhibiting Muscle Cell Proliferation," *J Immunology,* vol. 187, no. 10, pp. 5419-5428, 2011.

[11] T. Kaufman et al., "Innervation of an engineered muscle graft for reconstruction of muscle defects," *Am J Transplantation,* doi: 10.1111/ajt.14957, 2018.

[12] A. Ruijs, J. Jaquet, S. Kalmijn, H. Giele and S. Hovius, "Median and Ulnar Nerve Injuries: A Meta-Analysis of Predictors of Motor and Sensory Recovery after Modern Microsurgical Nerve Repair," *Plast. Reconstr. Surg.,* vol. 116, no. 2, pp. 484-94, 2005.

[13] T. Smith, R. Nagalla, E. Chen and W. Liu, "Harnessing macrophage plasticity for tissue regeneration," *Advanced Drug Delivery Reviews,* vol. 114, pp. 193-205, 2017.

[14] J. Champion, Y. Katare and S. Mitragotri, "Particle shape: A new design parameter for micro- and nanoscale drug delivery carriers," *Journal of Controlled Release,* vol. 121, pp. 3-9, 2007.

[15] Arnida, M. Janat-Amsbury, A. Ray, C. Peterson and H. Ghandehari, "Geometry and surface characteristics of gold nanoparticles influence their biodistribution and uptake by macrophages," *European Journal of Pharmaceutics and Biopharmaceutics,* vol. 77, no. 3, pp. 417-423, 2011.

[16] M. Vazquez, J. Catalan-Dibene and A. Zlotnik, "B cells responses and cytokine production are regulated by their immune microenvironment," *Cytokine,* vol. 74, no. 2, pp. 318-326, 2015.

[17] T. Antoniv and L. Ivashkiv, "Dysregulation of interleukin-10-dependent gene expression in rheumatoid arthritis synovial macrophages," *Arthritis Rheum,* vol. 54, pp. 2711-2721, 2006.

[18] C. Greenhill et al., "Interleukin-10 regulates the inflammasome-driven augmentation of inflammatory arthritis and joint destruction," *Arthritis Res Ther,* vol. 16, pp. 419-428, 2014.

[19] T.H. Tran, R. Rastogi, J. Shelke and M. Amiji, "Modulation of Macrophage Functional Polarity towards Anti-Inflammatory Phenotype with Plasmid DNA Delivery in CD44 Targeting Hyaluronic Acid Nanoparticles," *Scientic Reports,* vol. 5, pp. 16632-46, 2015.

[20] P. Graney, E. Lurier and K. Spiller, "Biomaterials and Bioactive Factor Delivery Systems for the Control of Macrophage Activation in Regenerative Medicine," *ACS Biomater. Sci. Eng,* vol. 4, no. 4, pp. 1137-1148, 2018.

[21] T. Hemmerle, F. Doll and D. Neri, "Antibody-based delivery of IL4 to the neovasculature cures mice with arthritis," *Proc Natl Acad Sci USA,* vol. 111, no. 33, pp. 12008–12012, 2014.

[22] J. Tidball and S. Villalta, "Regulatory interactions between muscle and the immune system during muscle regeneration," *Am J Physiol Regul Integr Comp Physiol,* vol. 298, pp. R1173-R1187, 2010.

Appendix A:

Supplemental Figures for Chapter 2

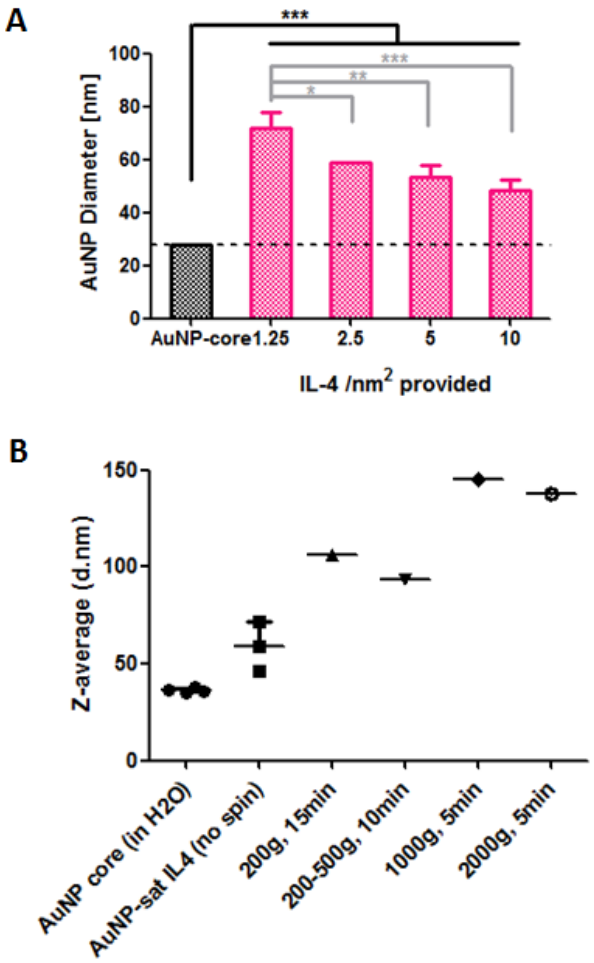


Figure A1. Increased IL-4 ligand density decreases AuNP-IL4 particle size. (A) Hydrodynamic diameter of AuNP-IL4 particles measured immediately following conjugation, and before washing, shows that particles with the highest IL-4 ligand densities have the smallest size. (B) AuNP-IL4 particles lacking PEG are susceptible to aggregation via centrifugation. Increasing the spin speed used in the wash steps increases particle aggregation.

Table A1. Characterization of AuNPs used in Bioactivity Assays

	Z-average [nm] Before wash	PDI Before wash	Z-average [nm] After wash	PDI After wash	Zeta Potential [mV] After wash
AuNP	NA	NA	33.44	0.147	-37.53
AuNP-PEG	Not measured		61.30	0.091	-16.9
AuNP-IL13 (0.25 /nm^2)	67.51	0.467	73.92	0.433	-12.13
AuNP	27.77	0.122	NA	NA	-33.13
AuNP-IL4 (5 /nm^2)	29.94	0.515	63.65	0.309	2.08

Appendix B:

Supplemental Methods for Chapter 3

Flow Cytometry

To assess cell recruitment and phenotype in the TAs, a single cell suspension was prepared using the skeletal muscle dissociation kit (MACS Miltenyl Biotec, # 130-098-305) with the gentleMACS^{TM} dissociator. Murine cells were blocked with CD16/CD32 monoclonal antibody (eBioscience # 14-0161-82) and then stained to assess immune cell presence, with the following antibodies CD45.2-FITC or CD45.2-PerCP/Cy5.5 (BioLegend #109828), CD3-PE/Cy5, CD4-PacBlue, CD11b-APC/Cy7 or CD11b-Pacific Blue (BioLegend #101224), Ly6C-PE/Cy7 or Ly6C-PE (BioLegend #128008), Gr-1-APC, F4/80-PE or F4/80-APC (BioLegend #123116), Ly6G-AlexaFluor 488 (BioLegend #127626), CD11c-APC/Cy7 (BioLegend #117324) at the concentrations recommended by the manufacturer to assess cell recruitment. A separate panel was used to assess macrophage polarization: CD86-FITC (eBioscience #11-0862-82 or BioLegend #105006), CD206-APC (BioLegend #141708), F4/80-PE (eBioscience #12-4801-82) or F4/80-PerCP/Cy5.5 (BioLegend #123128), CD11b-APC/Cy7 (BioLegend #101226), CD80-Pacific Blue (BioLegend #104724), and CD163-Cy3 (Bioss Antibodies #bs-2527R-Cy3) or CD163 (Santa Cruz #18796) + PerCP/Cy5.5 secondary (Santa Cruz #45102) at the concentrations recommended by the manufacturer. Unstained cells, fluorescent minus one controls, and the appropriate isotype controls recommended by the manufactures were used as controls in the gating. To identify recruited immune cells the following definitions were used: myeloid cells (CD11b+/CD11c-), macrophages (CD45+/CD11c-/CD11b+/Ly6G-/Ly6C-/ F4/80+) or (CD45+/CD11b+/CD3-/F4/80+) depending on the staining panel, monocytes (CD45+/CD11c-/CD11b+/Ly6G-/Ly6C+/ F4/80-) or (CD45+/CD11b+/CD3-/F4/80-/Gr1 lo or -) depending on the staining panel, monocyte/macrophages (CD45+/CD11c-/CD11b+/Ly6G-/Ly6C+/ F4/80+), neutrophils (CD45+/CD11b+/CD3-/F4/80-/Gr1^{hi}/Ly6C^{lo}), T cells (CD45+/CD11b-/CD3+), patrolling monocytes (CD45+/CD11b+/CD3-/F4/80-/Gr1-/Ly6C^{lo} or -). CD206 expression on macrophages was used as an indicator of M2a polarization, CD163 as an indicator of M2c polarization,

and CD80 and CD86 as indicators of M1 polarization. Cells were fixed and stored in 0.4% PFA at 4^{o}C until they were run on an LSR II flow cytometer, within 3 days following staining.

For in vitro polarization studies, human THP-1 derived macrophages were stained with near-IR fixable dead cell stain (Invitrogen #L10119). Then they were blocked with Fc receptor blocking solution (Human TruStain FcX^{TM}, BioLegend #422302) and stained with the following antibodies: CD206-PE (BioLegend #321106), CCR7-APC (BioLegend #353214), and CD163-FITC (BioLegend #333618) at the concentrations recommended by the manufacturer. CD206 expression was used as an indicator of M2a polarization, CD163 as an indicator of M2c polarization, and CCR7 as an indicator of M1 polarization on live cells. Unstained cells, and the isotype controls recommended by the manufacture were used as controls in the gating. Cells were fixed and stored in 0.4% PFA at 4^{o}C until they were run on an LSR II flow cytometer, within 3 days following staining.

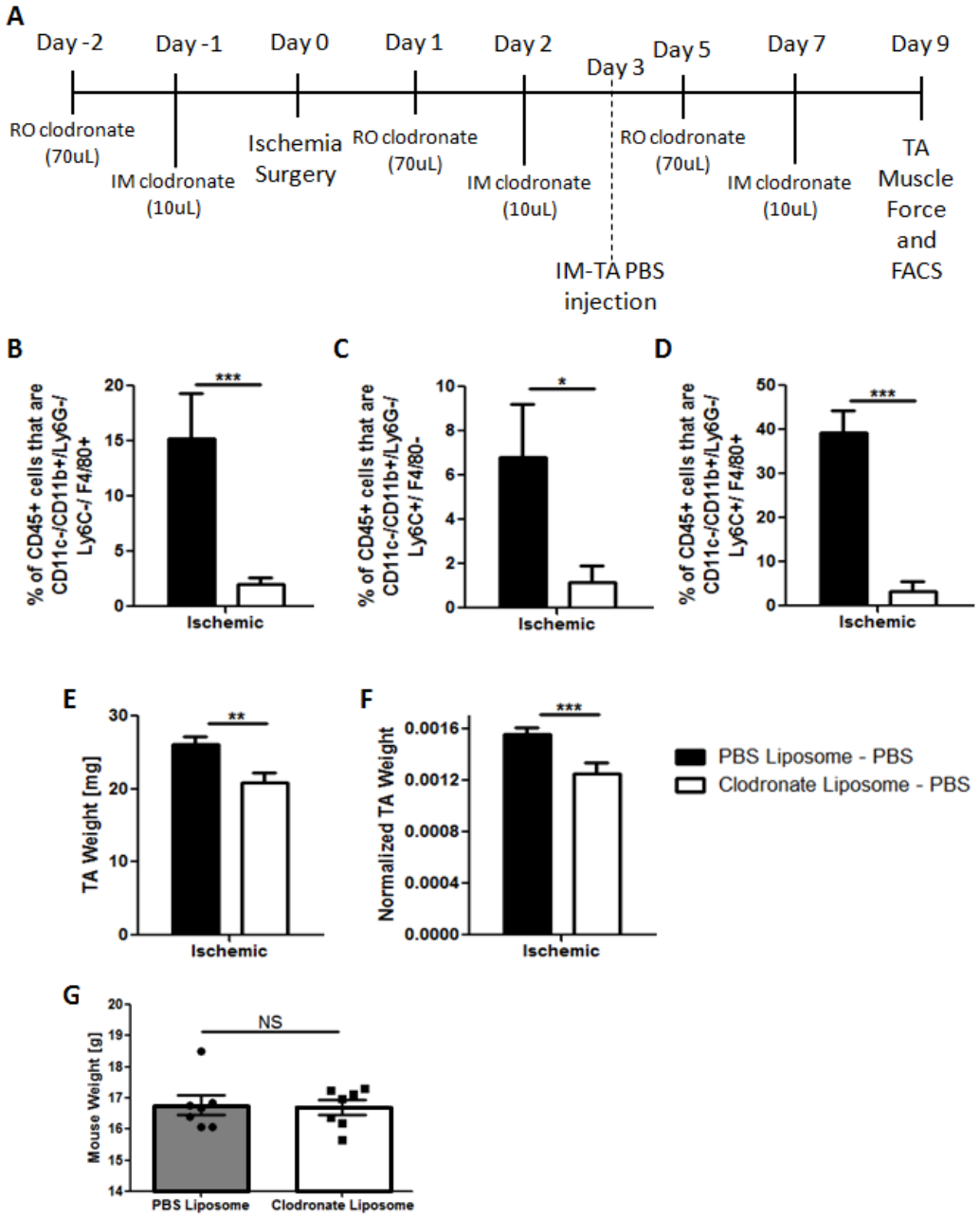
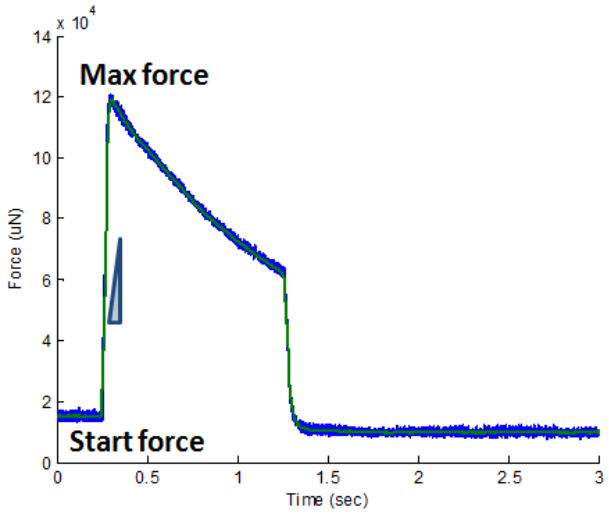


Figure B1. Clodronate depletes monocyte/macrophages and inhibits muscle regeneration. (A) Experimental design showing clodronate and PBS-treatment schedule in relation to the surgical induction of ischemia and muscle assessment. (B-D) The percentage of CD45+ immune cells in the TAs that were macrophages (CD11c-/CD11b+/Ly6G-/Ly6C-/ F4/80+) (B), monocytes (CD11c-/CD11b+/Ly6G-/Ly6C+/ F4/80-) (C), and monocyte/macrophages (CD11c-/CD11b+/Ly6G-/Ly6C+/F4/80+) (D), quantified by flow cytometry on day 9 after surgery. (E) The weight of the TA muscle isolated from the ischemic limb 9 days after surgery, following treatment with PBS-liposomes (control, black bar), or clodronate-liposomes (white bar). (F) The weight of the TA was normalized to the weight of the mouse. (G) Mouse weight on day 9 after surgical induction of ischemia. All data are means ±SEM of 7 mice per group. *P < 0.05, * P < 0.01, and ***P < 0.001

A



B

$$\text{Maximum Force [uN/mg]} = \frac{\text{Max force} - \text{Start force [uN]}}{\text{TA weight [mg]}}$$

C

Contraction Velocity = slope at 0.26s

Figure B2. Contraction force curve data from ex vivo tetanic stimulation of TA muscles. (A) Intact TA muscles were mounted between 2 parallel steel wire electrodes, and connected by microclips to a force transducer. A pulse wave was used to stimulate the muscle at 25V, 250Hz; 27V, 270Hz; and 30V, 300Hz for 1s. Each muscle was tested at all 3 stimulations with 5min rest between each test. The contraction force curves (blue) were smoothed in MATLAB (green line). (B) The maximum force was determined to be the difference between the maximum force recorded and the starting baseline, and was normalized by the TA mass. (C) The contraction velocity was calculated as the slope of the force curve at the time of stimulation, 0.26s.

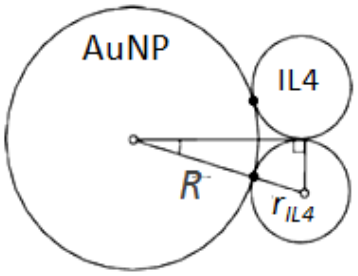


Figure B3. Schematic used to determine the theoretical maximum loading of IL-4 onto AuNPs based on sphere packing.

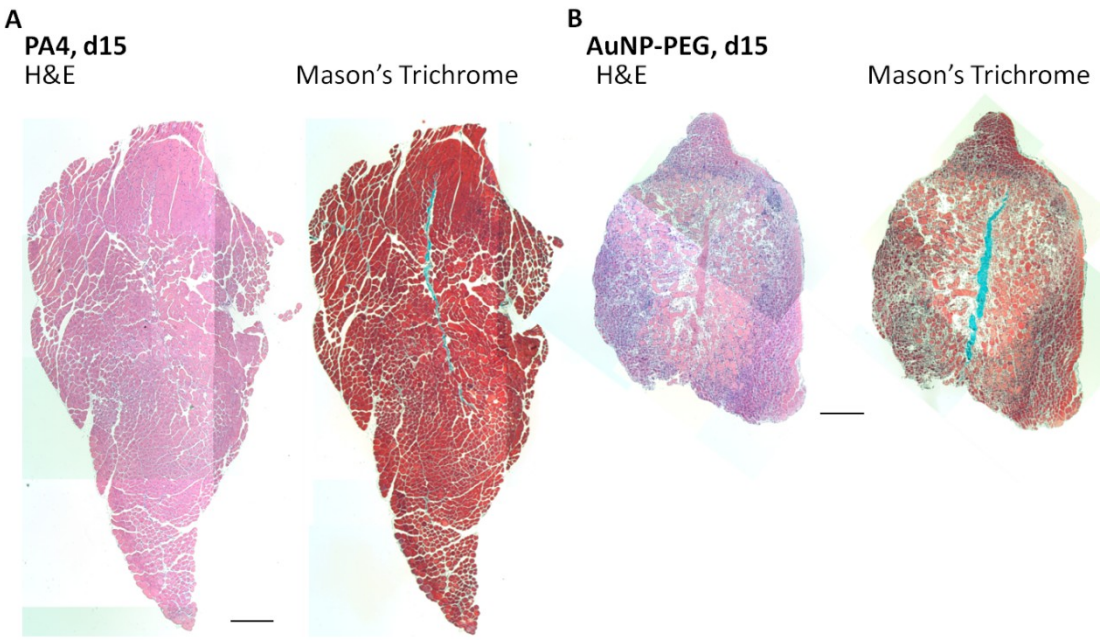


Figure B4. Improved muscle architecture and minimal to no fibrosis following PA4 treatment. Representative H&E (left) and Mason's trichrome staining (right) of TA muscles on day 15 following surgery from mice treated with PA4 (A) or AuNP-PEG particles lacking IL-4 (B). Scale bars = 1.5mm

Appendix C:

Supplemental Figures for Chapter 4

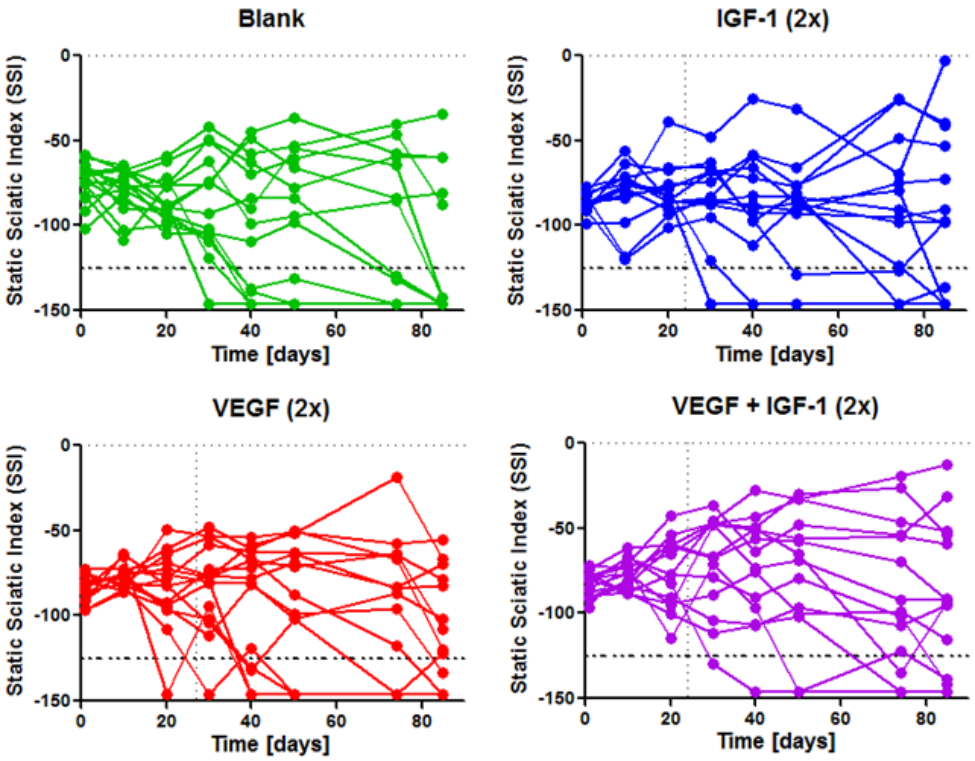


Figure C1. SSI Tracking of Individual Aged Mice. Sciatic nerve function in aged (14wk) mice was tracked following surgery and treatment with blank, IGF-1, VEGF, or VEGF + IGF-1 alginate by assessing the SSI every 10-20 days. Growth factor containing gels were administered at the time of surgery and again between days 20-30 (timing of the booster alginate injection is indicated by a dotted vertical line on the graphs). When SSI $\leq$ -125 (indicated on the plots) mice lost the ability to regain function (as measured by SSI). SSI $\geq$ -5.49 indicates no impairment, SSI $\leq$ -145, complete loss of function.

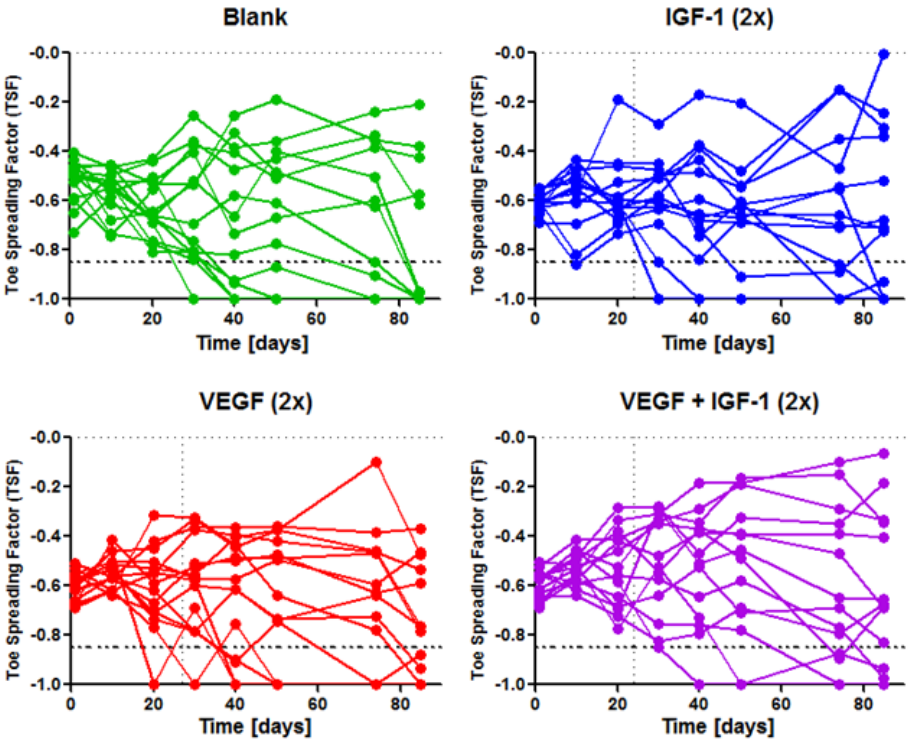


Figure C2. TSF Tracking of Individual Aged Mice. Toe spreading function in aged (14wk) mice was tracked following surgery and treatment with blank, IGF-1, VEGF, or VEGF + IGF-1 alginate by assessing the TSF every 10-20 days. Growth factor containing gels were administered at the time of surgery and again between days 20-30 (timing of the booster alginate injection is indicated by a dotted vertical line on the graphs). When TSF $\leq$ -0.85 (indicated on the plots) mice lost the ability to regain toe spreading function (as measured by TSF). TSF = 0 implies no impairment, TSF = -1 indicates total loss of function with no toe spreading.

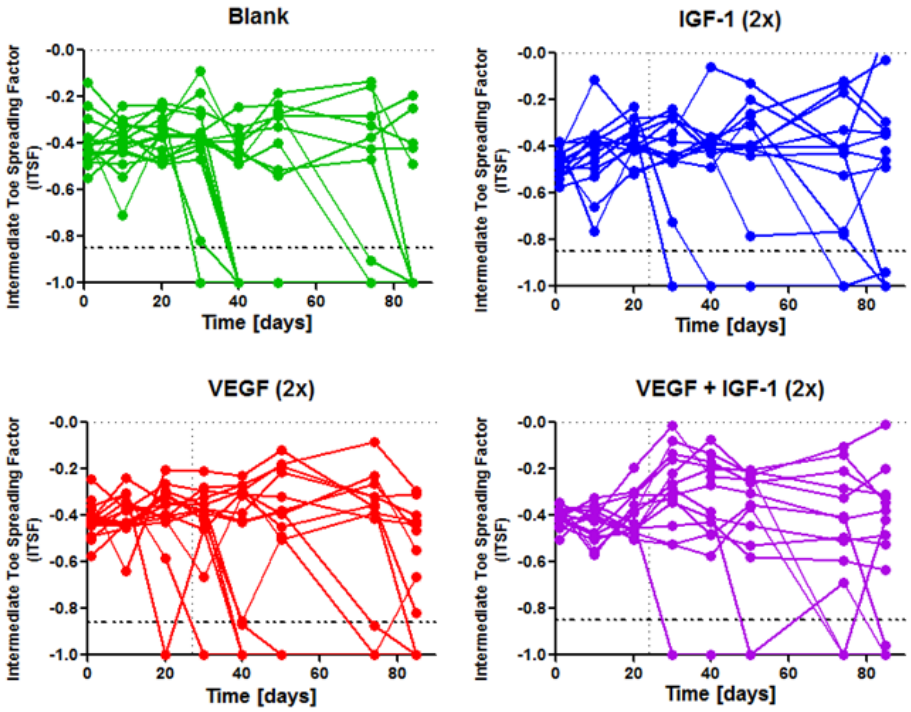


Figure C3. ITSF Tracking of Individual Aged Mice. Toe spreading function in aged (14wk) mice was tracked following surgery and treatment with blank, IGF-1, VEGF, or VEGF + IGF-1 alginate by assessing the ITSF every 10-20 days. Growth factor containing gels were administered at the time of surgery and again between days 20-30 (timing of the booster alginate injection is indicated by a dotted vertical line on the graphs). When ITSF $\leq$ -0.85 (indicated on the plots) mice lost the ability to regain toe spreading function (as measured by ITSF). ITSF = 0 implies no impairment, ITSF = -1 indicates total loss of function with no toe spreading.

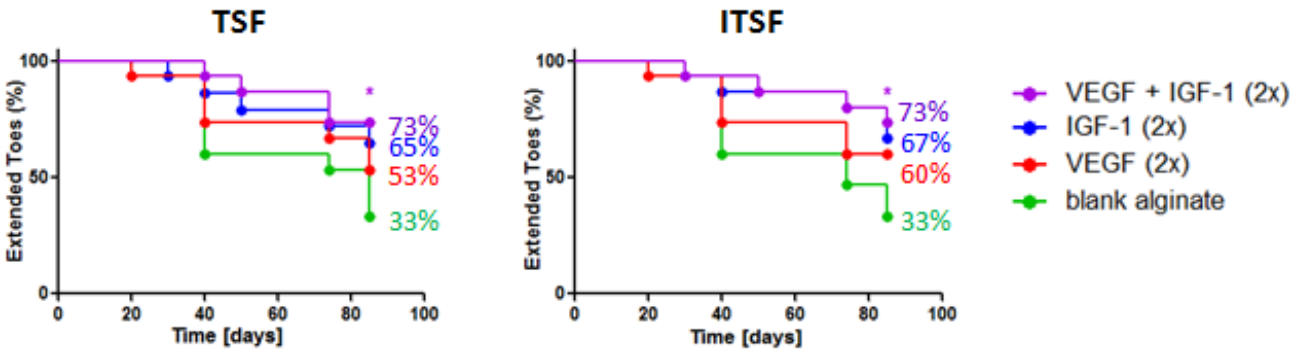


Figure C4. Prolonged Maintenance of Toe Spreading Function following alginate delivery of VEGF + IGF-1 in aged mice. Toe spreading function in aged (14wk) mice was tracked following surgery and treatment with blank, IGF-1, VEGF, or VEGF + IGF-1 alginate by assessing the TSF and ITSF. Once a specific level of severe toe spreading function was lost (indicated by I/TSF $\leq$ -0.85) mice were no longer able to recover any functional toe spreading or extend their toes. The percentage of mice that maintained the ability to extend their toes (i.e. maintained I/TSF > -0.85) were plotted on Kaplan-Meier curves. n=14-15. *p<0.05 Mantel-Cox single comparison vs. blank